Spring 5-25-2019

Two and Three-Dimensional Models for Material and Cells Interaction

Nam H. Nguyen
Louisiana Tech University

TWO AND THREE-DIMENSIONAL MODELS FOR MATERIAL AND CELLS INTERACTION

by

Nam H. Nguyen, M.S.

A Dissertation Presented in Partial Fulfillment
of the Requirements of the Degree
Doctor of Philosophy

COLLEGE OF ENGINEERING AND SCIENCE
LOUISIANA TECH UNIVERSITY

May 2019

LOUISIANA TECH UNIVERSITY

THE GRADUATE SCHOOL

April 2, 2019
Date of dissertation defense

We hereby recommend that the dissertation prepared under our supervision by **Nam H. Nguyen, M**.S.

entitled **Two and Three-dimensional Cell Models for Material and Cells Interaction**

be accepted in partial fulfillment of the requirements for the degree of

Doctor of Philosophy in Biomedical Engineering

Supervisor of Dissertation Research

Head of Biomedical Engineering

Recommendation concurred in:

Advisory Committee

Approved:

Director of Graduate Studies

Dean of the College

Approved:

Dean of the Graduate School

GS Form 13a
(10/18)

ABSTRACT

Three-dimensional (3D) cell spheroid model has been long considered a better model to mimic *in vivo* physiology compared to two-dimensional (2D) cell culture model. Traditional 2D cell models provide a simple, convenient and quick technique for drug screening but fail to simulate the complexity and heterogeneity of cells in the *in vivo* environment. The last few decades have remarked substantial progress toward the advancement of three-dimensional (3D) cell cultures as systems which better mimic cell-cell and cell-matrix interaction in the *in vivo* physiology. Nowadays, 3D cell models have been emerging, not only as an important approach in drug discovery and tissue engineering but also as potential therapeutics assessment for the development of new anticancer strategies. The employment of new 3D cell culture models in combination with traditional 2D models and co-culture models of two or more cell types would enable more accurate evaluation of drug efficiency and sensitivity, toxicity, resistance for *in vitro* testings before moving into *in vivo* studies and clinical trials.

A novel material, copper high aspect ratio structure (CuHARS) which is biocompatible, biodegradable and less toxic compared to copper nanoparticles with the same amount of copper has the potential to be used as a delivery system for drug treatment or tissue engineering. Moreover, a combination of CuHARS and disulfiram (DSF) to form DSF metal complex showed significant increase in growth inhibition of

gliomas in both 2D and 3D models suggested a promising approach in treating glioblastomas.

APPROVAL FOR SCHOLARLY DISSEMINATION

The author grants to the Prescott Memorial Library of Louisiana Tech University the right to reproduce, by appropriate methods, upon request, any or all portions of this Dissertation. It is understood that "proper request" consists of the agreement, on the part of the requesting party, that said reproduction is for his personal use and that subsequent reproduction will not occur without written approval of the author of this Dissertation. Further, any portions of the Dissertation used in books, papers, and other works must be appropriately referenced to this Dissertation.

Finally, the author of this Dissertation reserves the right to publish freely, in the literature, at any time, any or all portions of this Dissertation.

Author _____

Date _____

DEDICATION

This work is dedicated to my beloved family, Nguyễn Hồng Tuấn (my dad), Hoàng Thị Nguyệt (my mom) and Nguyễn Thu Hằng (my little sis) for their marvelous encouragement, understanding and patience all these long years; to my dear Nguyễn Chinh, for your inspiration and mental support. You guys are the best!

TABLE OF CONTENTS

LIST OF FIGURES

LIST OF TABLES

ACKNOWLEDGMENTS

My upmost gratitude goes towards all those who help make this amazing journey possible. First of all, I want to express my gratefulness to my advisor, Dr. Mark DeCoster for his tremendous guidance, insightful advice and constant encouragement throughout my doctoral research. I would like to thank Dr. Steve Jones, Dr. Teresa Murray, Dr. Gergana Nestorova and Dr. Thomas Bishop for their help and counsel as committee members. Many thanks to all my colleagues, especially members of my lab – my second family, who helped me in countless ways all these years. I am grateful to Zach Norcross, Urna Kansakar, Kahla St. Marthe and Kyle Rugg for their huge contributions and many useful suggestions. I am also grateful for Miles Delahoussaye and Mark Gragston for their training back then when I just joined the lab.

I would like to acknowledge Dr. Gergana Nestorova, Dr. Jessica L. Scoggin, Chao Tan, Dr. Prabhu Arumugam and Dr. Teresa Murray for all the helpful discussions during our collaborations.

I would also like to thank Dr. James Spaulding and Emily Born for their help and training in animal care, Dr. Raghuvara Yendluri and Dr. Lvov's lab for providing the materials used in this research. I would like to express my appreciation to all my friends at Louisiana Tech University as Tech has truly become my second home.

I am grateful to Neela Prajapati and Suman Sinkhwal for their support during the final months of my writing. And finally, special thanks to my family for their love and the continuous support they have given me.

CHAPTER 1

INTRODUCTION

1.1 Glioblastoma

Glioblastoma multiforme (GBM), the most common form of brain cancer, is a fatal and incurable disease [1]. About 65% of all primary brain tumors are caused by GBM and the survival rate is less than 5 years in 90% of patients [2]. Treatments often require surgery and chemotherapy, but in most cases, are ineffective [3]. The lack of adequate treatment and high recurrence rate is believed to be driven by glioma stem cells (GSC), which have the ability to self-renew, are resistant to drugs and are extremely invasive [4]. **Figure 1.1** shows an example of CRL-2303, a type of immortalized glioblastoma grown in traditional 48-wells culture plate. The aforementioned characteristics of GSC underscore the need for improved methods to study the progression of GBM and its recurrence mechanism and for novel breakthrough therapies to prevent GBM recurrence and extend the lives of patients suffering from this fatal disease. One of these approaches is to use anticancer drugs with convection-enhanced delivery of nanocarriers [5]. The purpose of this study is to examine the novel copper high aspect ratio structure biomaterial (CuHARS) as a potential carrier for delivering cancer drug in two and three-dimensional cell cultures.

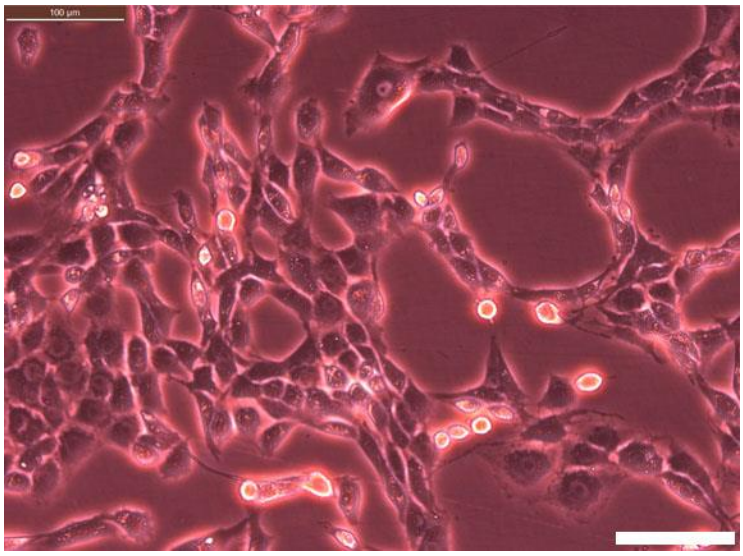

Figure 1.1: Glioblastoma (CRL-2303 – ATCC) in cell culture, imaged with phase microscopy at 200x magnification. Scale bar = 100 µm.

1.2 Three-Dimensional Cell Culture Model

The three-dimensional (3D) cell spheroid model has emerged in recent years as a new approach in cell sciences in contrast to traditional two-dimensional (2D) model with several advantages. Cell proliferation, morphology, and physiology in the 3D model better mimic the tissue micro-environment with potentially three layers of cells (proliferating, quiescent and necrotic), growing at different rates, instead of the more homogeneous rate in 2D model [6]. One of the most exciting facets of creating *in vitro* 3D cancer models is the ability to experimentally manipulate each component of the tumor microenvironment to try and understand the drivers of cancer as a disease state. Furthermore, diffusion considerations cause the *in vitro* 3D model to respond more accurately to drug treatment than 2D monolayers. Growing cells as 3D spheroids can increase resistance to chemotherapy when compared to the same cells grown in monolayers. The most straightforward explanation for enhanced resistance is that the cells on the inside of the spheroid are protected from drug penetration by the cells on the

outside of the spheroid. Another mechanism has been suggested related to the differential zones of proliferation [7], [8]. However, 3D cultures take longer time to form, and their longer diffusion times slow the effect of drugs. Also, 3D spheroid data needs to be normalized (area and volume) to interpret the results. **Figure 1.2** illustrates an example of 3D spheroid developed using a proprietary technique by our lab.

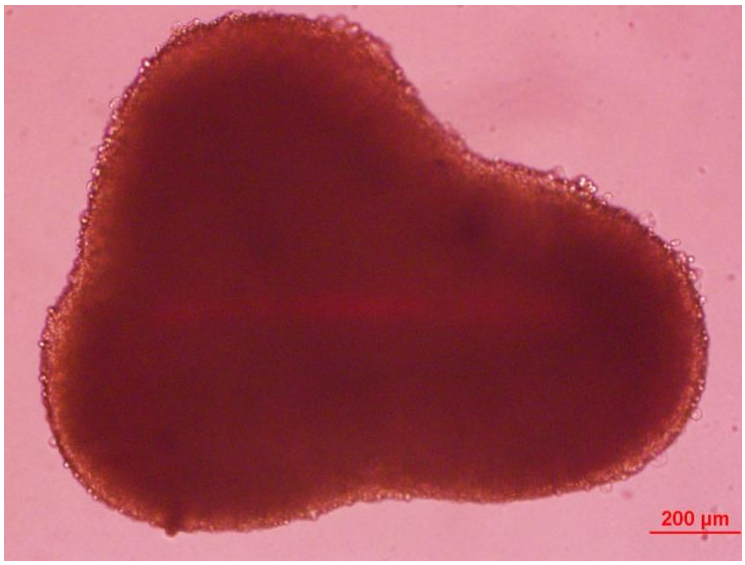

Figure 1.2: 3D spheroid of glioblastoma brain tumor cells grown in our lab. Scale bar = 200 µm.

1.3 A Novel Biomaterial for Drug Delivery System

CuHARS is a novel biocomposite made from copper and the amino acid cystine which has previously been discovered and published by Dr. DeCoster's lab at Louisiana Tech University [9]. The material has a rod-like shape and has both nano and micro-features [10], [11]. CuHARS has a vast potential for drug delivery systems because it is extremely stable in water but breaks down in cell culture media or when it interacts with cells. Biomaterials as a carrier for drug delivery system has been a hot topic in drug discovery research for the last three decades [12]. Much work has considered the

advantages of different types of biomaterials for targeting tumors and deliver drugs to the tumor site; but minimal research considers the fate of the biomaterial after drugs are delivered to the tumor and how our bodies dispose of those material [13]. For example, halloysite nanotubes (HNTs) which are made from clay, do not break down after entering our bodies. CuHARS is thus a great candidate for use in drug delivery research because it is confirmed to degrade over time after it is introduced in cell culture media or interacts with cells [14]. **Figure 1.3** and **1.4** are electron microscope images showing detailed structure of the CuHARS with both nano- and micro features.

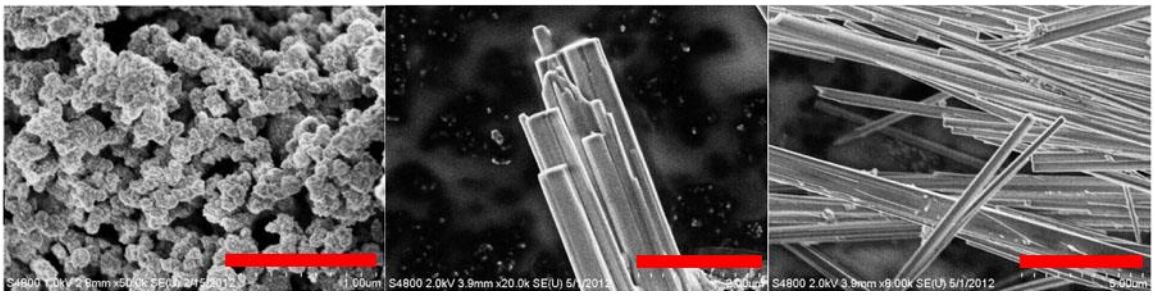

Figure 1.3: SEM images of starting material copper nanoparticles (left), and metallic biocomposite structures shown at the micro-scale (middle and right panels). Scale bars are 1 µm (left panel) and 5 µm (middle and right panels).

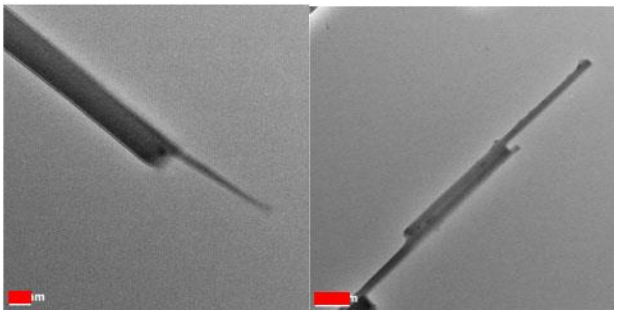

Figure 1.4: TEM images of the bio-metallic composites shown at the nanoscale. Scale bars are 50 nm (left panel) and 200 nm (right panel).

1.4 Disulfiram as a Potential Cancer Drug

Disulfiram (DSF) – an FDA approved drug to treat alcoholism, has recently been identified as a promising drug for cancer treatment, including GBM [15]. The mechanisms of action of DSF are not clearly understood, however research has indicated: 1) proteasome inhibition; 2) NF_kB inhibition; 3) epigenetic alteration; 4) re-sensitizing GBM to temozolomide (TMZ); 5) radio-sensitizing GBM cells, and 6) targeting in GSC. **Figure 1.5** shows the chemical structure of DSF, which can generate copper diethyldithiocarbamate ($Cu(DDC)_2$) complex, an active anticancer agent when DSF is applied in the presence of copper [16].

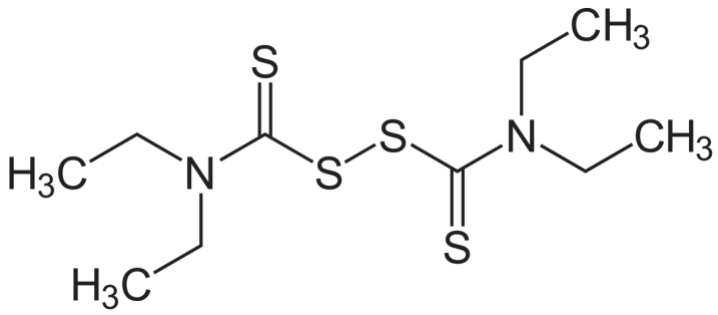

Figure 1.5: Disulfiram molecular structure.

DSF is of interest to this study because data suggest that DSF in the presence of copper shows better effects on cancer cells, including the aggressive GBM [17]. Since the CuHARS contains copper and degrades over time *in vitro*, a combination of DSF and CuHARS could be a novel therapeutic approach to treat GBM.

1.5 Objective of This Study

The overall goal of this research project is to study the use of a novel matrix free three-dimensional spheroid as a new approach to study the interaction of brain cells with different biomaterials and drugs. It will be divided into 3 major objectives:

Objective 1: To demonstrate similarity and difference in interaction with materials (CuHARS, CuNPs and HNTs) between three-dimensional spheroids compared to traditional two-dimensional cell culture.

Objective 2: To demonstrate the use of the novel material CuHARS as a potential carrier in a delivery system of drug treatment and/or cell growth promotion.

Objective 3: To demonstrate a method to modify the CuHARS to get a more uniform in size and shape CuHARS for better carrier and interaction with cells as well as the degradable ability of CuHARS in cell culture media under physiological conditions.

1.6 Dissertation Overview

Chapter 1 reviews the relevance and motivation and research goals of the study. Chapter 2 provides the background on the two cell types used in this study, primary astrocyte and glioma cells, the two cell culture techniques, traditional two-dimension and three-dimensional models together with their advantages and disadvantages. We will also discuss a novel technique developed by our group to create a 3D dimensional model. Chapter 3 compares two-dimension and three-dimensional models in term of cell morphology and interaction with different materials while Chapter 4 provides quantitative analysis for toxicity of these materials on both cell types in the two cell culture models and considers the potential of a novel biomaterial discovered by our group called CuHARS to be used as a delivery system. Chapter 5 describes a method to modify

the CuHARS without changing its characteristics for better integration into cell culture. Finally, Chapter 6 investigates the technique of cultivating a mixed co-culture model (both 2D and 3D) consisting of primary astrocytes and gliomas that can be utilized to study tumor invasiveness and cell-cell interactions between different cell populations.

CHAPTER 2

BACKGROUND

2.1 Cells of The Brain: Astrocytes

The human brain consists of approximately 10^{12} cells, with the number of neurons are considered to be approximately 10^{11}, and the rest being glia (around $9x10^{11}$); which means glial cells outnumber neurons by 2-9 times in the central nervous system (CNS). Astrocytes, one of the major classes of glial cells (along with microglia, oligodendrocytes and Schawann cells) outnumber neurons by approximately five fold [18] and derive their name from the roughly star-shaped cell bodies with many processes, as shown in **Figure 2.1**. Two major types of astrocytes are fibrous astrocytes (found in the white matter), with a high number of long processes that contain large bundles of intermediate filaments, and Protoplasmic astrocytes (found in the gray matter), with many processes that end in sheet-like appendages. Both types of astrocytes have end-feet which contact and surround capillaries, arterioles, and neurons throughout the brain. The protoplasmic astrocytes' processes cover nerve cell bodies and synapses, whereas the end-feet of fibrous astrocytes contact axons at the nodes of Ranvier [19].

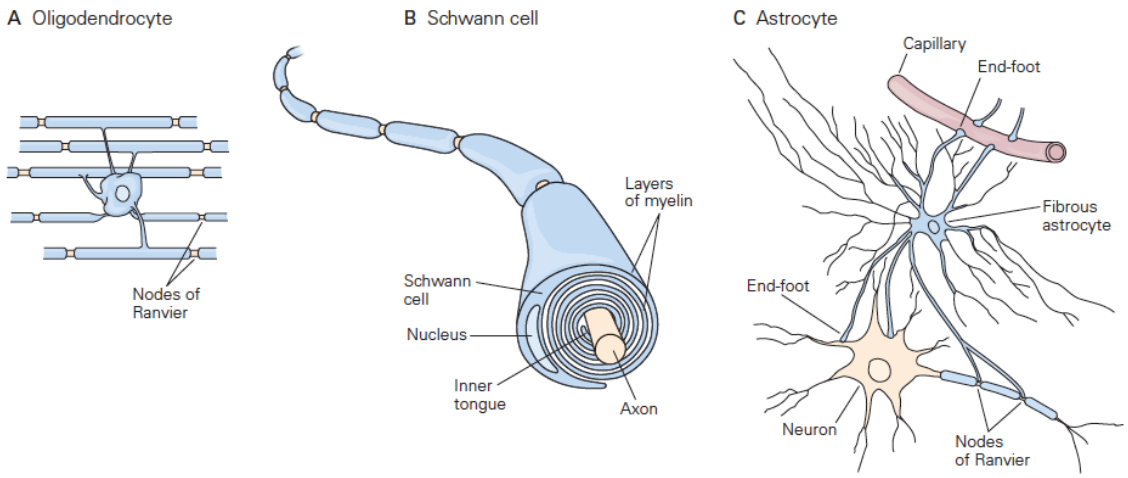

Figure 2.1: Major types of glial cells in the CNS (oligodendrocytes and astrocytes) and in the peripheral nervous system (Schwann cells) [19].

Although some of the functions of astrocytes are still not fully understood [18], it is generally thought that astrocytes are not essential for information processing but support, protect neurons, and provide nutrition to the neurons [19], [20]. Astrocytes are believed to support neurons in five major ways:

1. Astrocytes help separate cells, thus insulating neuron cells and their synapses from improper interconnections.

2. Astrocytes are highly permeable to some ions (specifically K^+) and thus, they help regulate these ion concentrations inside the brain. For example, during an action potential, neurons release K^+ when they fire. Without astrocytes to take up and regulate K^+ in the extracellular space, repetitive firing may create excess K^+ that could reduce the signaling efficiency between neurons. Astrocytes also regulate Ca^{2+} which is involved in neuronal calcium signaling [21], [22].

3. Astrocytes uptake neurotransmitters (mainly glutamate, GABA) and recycle them for future use by the neurons, and thus support neuronal signaling [23]–[25].

Although astrocytes (and other glial cell types) do not generate action potentials, they participate in neuron-glial signaling processes. This signaling is still poorly understood, but it is believed to actively help to regulate synapse development and function.

4. Astrocytes also help nourish surrounding neurons by providing various necessary growth factors. Astrocytes express enzymes which are not available in neurons and produce metabolic intermediates of several metabolic pathways [26], [27].

5. Astrocytes help to control cerebral blood flow and maintaining the blood–brain barrier. Astrocytes help regulate local CNS blood flow by having extensive contacts with blood vessels and producing and releasing various molecular mediators, such as prostaglandins (PGE), nitric oxide (NO), and arachidonic acid (AA), which can cause CNS blood vessel to dilate or constrict [18]. The blood–brain barrier (BBB) is composed of the blood vessels that vascularize the central nervous system (CNS) and possess unique properties to act as a diffusion barrier that tightly regulate the movement of ions, molecules, and other substances between the blood and the brain, in order to defend the brain from any potential harm circulating in the blood [28], [29]. However, astrocytes' exact role in the BBB, especially in patients with stroke or brain trauma is still poorly defined [30]. Recent studies suggested that several factors released by astrocytes might be important for the induction and maintenance of the BBB. In particular, transforming growth factor alpha (TGF-α) and glial-derived neurotrophic factor (GDNF) are believed to support the formation of tight junctions in cultured endothelial cells [28], [31], [32].

2.2 Malignant Glioblastoma

The most common category of brain tumor is brain metastases (or secondary brain tumors) which are the spread of a primary tumor to the brain and which account for 10-

30% of cancer cases [33], [34]. As the name suggested, the cancer cells (lung, breast, colon, kidney and melanoma) start from different parts of the body then break off from the original mass and move through the bloodstream or lymph system and spread to the brain [35].

In contrast, primary malignant brain and other CNS tumors are rare. The incidence of primary brain tumors worldwide is approximately 4 to 10 per 100,000 individuals per year, and varies up to three fold between countries and ethnic groups [36]–[38]. Although brain tumors account for only about 2% of all cancers in adults and 7% of the years of life lost from cancer before the age of 70, the survival rate of patients with brain cancer improves very little or remains unchanged. The length of survival can be as short as 9 months in patients with highly invasive tumor types [38], [39]. The common gliomas affecting the CNS of adults are often referred to as “diffuse gliomas” because they have diffuse infiltrative growth throughout the brain parenchyma [39], [40]. Gliomas are classified histologically, immunohistochemically, as astrocytomas, oligodendrogliomas and ependymomas as displayed in **Figure 2.2**, based on cell types they originated from (astrocytes, oligodendrocytes and ependymal cells, respectively) in which astrocytomas accounts for over 75% of gliomas cases [41].

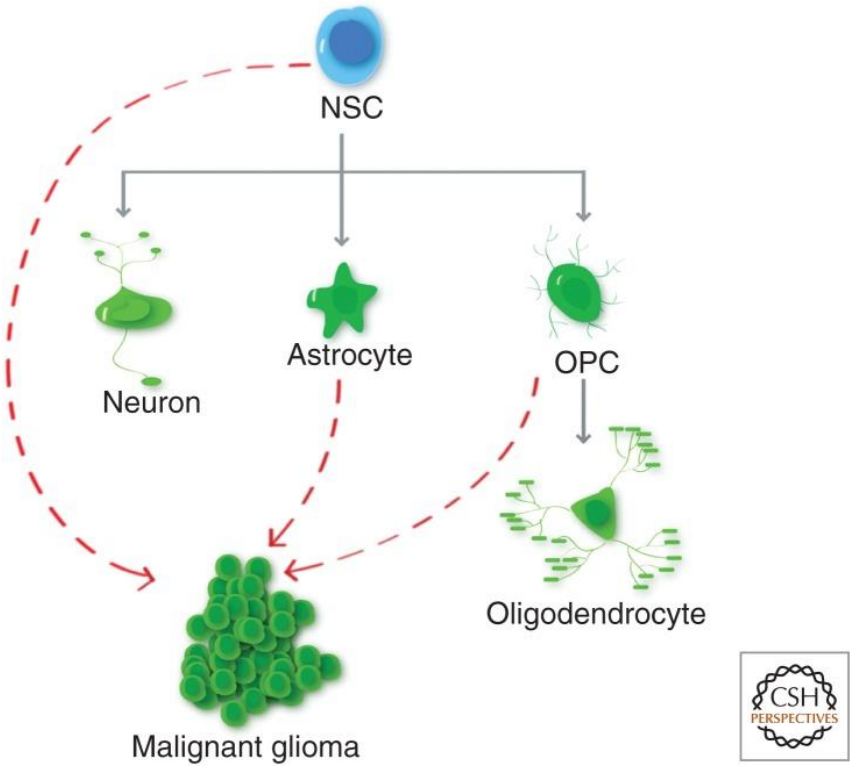

Figure 2.2: Cell of Origin for Malignant Gliomas. Neural stem cells (NSCs) differentiate into neurons, astrocytes, and oligodendrocyte precursor cells (OPCs). All these three cell types can mutate and give rise to malignant gliomas as indicated by dotted red lines [42].

Tumors are further categorized by various histopathological features together with genetic alterations, based on how differentiated the tumor cells are from the original cells, into grade from I to IV as presented in **Figure 2.3** [39], [43]. Grade I tumors are slow growing, unlikely to spread and mostly benign. They can be cured with surgery and the 5-year survival rate of patients with grade I tumors is over 90% [44]. Grade II tumors are low-grade malignancies which are moderately slow growing but are likely to recur after treatment, thus requiring long clinical treatment courses; life expectancy is 5-10 years after diagnosis and varies by ages. Grade III tumors demonstrate increased anaplasia (hence the alternative name, anaplastic astrocytoma) and proliferation over grade II tumors with rapidly dividing cells but little or no necrotic cells, and they are more rapidly

fatal than Grade II; life expectancy drops to 2-3 years with 5-year survival rate for patients over 55 years old of less than 10% [44], [45]. Grade IV tumors (or glioblastoma) exhibit more advanced features of malignancy, invasion including angiogenesis (vascular proliferation) and necrosis, as well as resistance to radio/chemotherapy and high recurrence rate; the survival rate in all age groups is normally less than 12 months [41], [44]–[47].

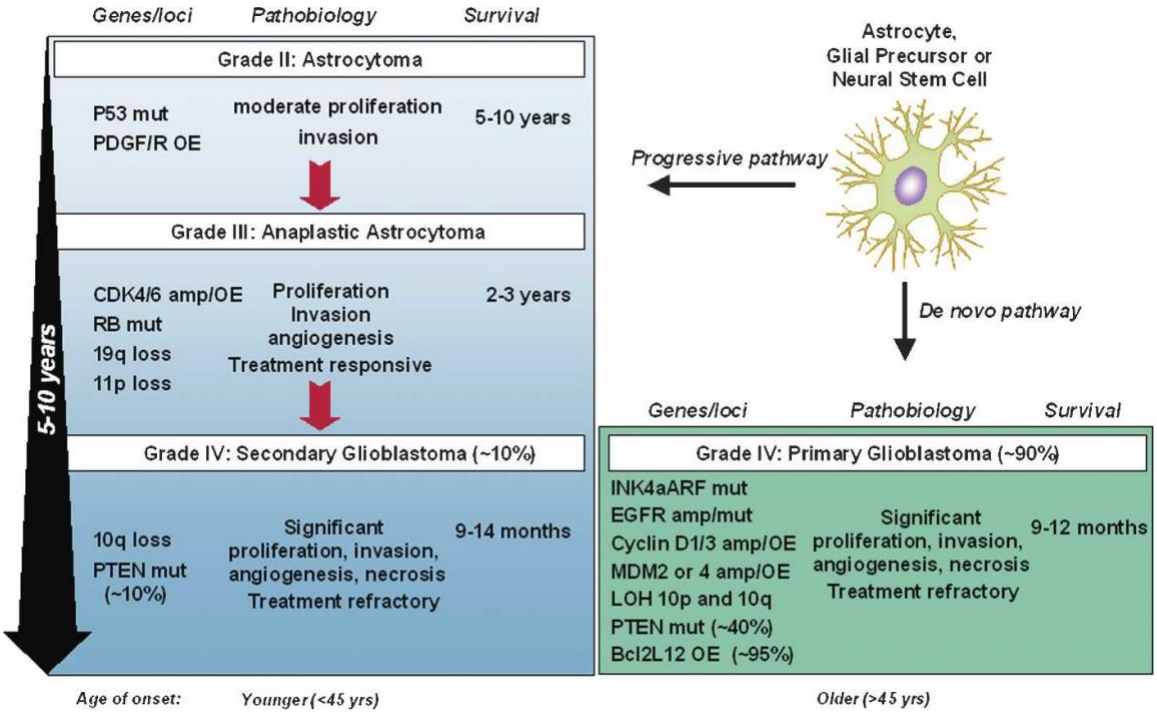

Figure 2.3: Characteristics, chromosomal and genetic aberrations related as well as survival expectancy for Grade II-IV of astrocytoma [39].

Type IV glioblastoma, often called glioblastoma multiforme (GBM), represents the most malignant, aggressive and fatal type of brain tumor. Primary treatment usually consists of surgery followed by radiation and chemotherapy. However, recurrence frequently occurs within 6-9 months after treatments [48]–[50]. On top of that, the cause for these types of brain tumors is generally unknown. Gene abnormalities are considered

to be one of the main factors deciding the progression of tumors, although the mechanism that leads to those abnormalities is still unclear.

Since GBM is derived from astrocytes – the major supportive cell type in brain, brain tumors can affect all kinds of brain functions in various areas. As a brain tumor grows, it may over time interfere with many of the normal functions of the brain (**Figure 2.4**). One of the first signs of GBM (headaches, seizures or changes in behavior) is increased pressure in the brain caused by the inability of the skull to expand to accommodate the aggressive growth of a tumor. Weakness or numbness in the arms or legs, language dysfunction, blurred vision, cognitive impairments as well as seizure are also common [51], [52]. Other symptoms may also occur, depending on the size and location of the tumor in addition to the age of patients.

Glioma brain tumor accounts for almost half of cancer and brain cancer mortality rates and in most cases are incurable [37], [39], [47], [50], [53]. Most cytotoxic drugs remain ineffective in treatment due to limited passage through the blood brain barrier (BBB). Several other limitations include resistance to chemotherapeutic agents and efficient DNA repair mechanism.

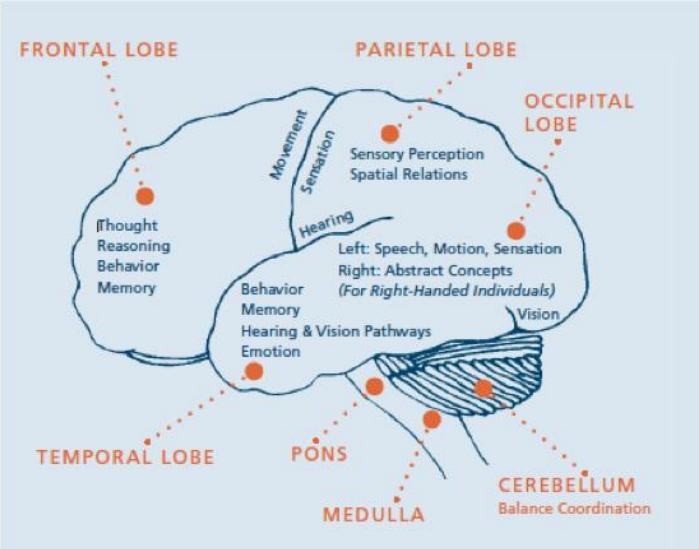

Figure 2.4: GBM can affect different functions of the brain depending on locations and size of the tumor [54].

2.3 Two Dimensional Versus Three-Dimensional Cell Culture

Cell-based assays, or *in vitro* two-dimensional cell cultures have played a vital role in the drug discovery process by offering a simple, fast, and cost-effective tool for preliminary testing before implementation of complicated and expensive animal testing. The term cell culture is used because results are based on the cellular responses (of cultured cells) to drugs, materials and other stimuli [6].

To date, traditional 2D cell culture is still the most frequently used method in cell assay and drug testing *in vitro.* The reason of its popularity is 2D cell culture presents a convenient, cheap and quick way to study drug responses. Cells can be placed on tissue culture Petri dishes, polystyrene plastic flasks or well-plates. It also does not require huge numbers of cells for experiment, so different combinations of drugs can be tested rapidly. In 2D model, cells form a monolayer on the bottom of the wells and all of the cells of such layer receive a homogenous amount of nutrients and growth factors from the medium during growth [55]. The monolayer also contains very few or no dead cells, but

is mainly composed of proliferating cells, because necrotic cells are usually detached from the surfaces and easily washed off. Cell morphology in 2D culture is usually flatter and more stretched than it is *in vivo* as shown in the schematic in **Figure 2.5**. Consequently, 2D modeled cells may not respond to drug or other materials the way they would inside the body.

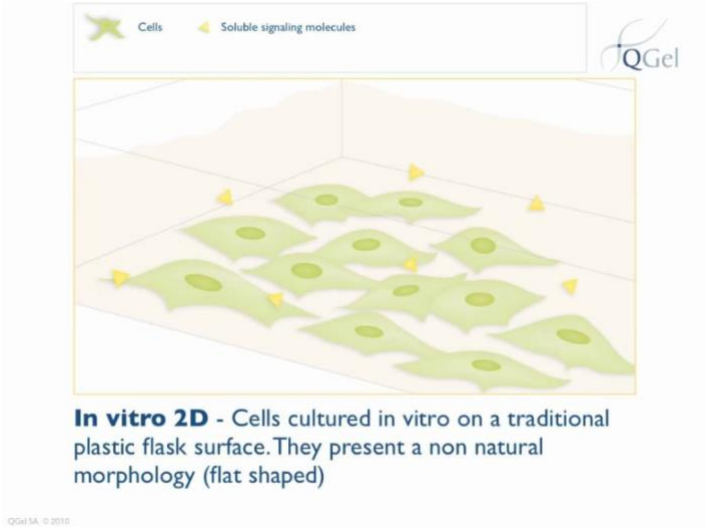

Figure 2.5: Schematic of cells grow in traditional 2D culture [56], [57].

In contrast, cells in 3D cell culture models grow into a spheroid within a matrix, scaffolds or suspension environment. Because of the tight contact in spheroids, cell-cell interactions and cell-extracellular matrix (ECM) interactions is believed to better mimic the microstructure and dynamic biochemistry of living tissues, which in turn can provide more accurate response in drug screening [55], [58]. Compared to 2D model, a typical 3D spheroid (as displayed in the diagram in **Figure 2.6**) is made of multiple layers growing at different rates, with a typical spheroid composed of proliferating, quiescent and necrotic layers [6], [59]. The outer layer, which has access to a maximum amount of nutrients and oxygen from the media, consists mostly of viable, proliferating cells (hence

the name proliferating layer). Cells in the middle layer still receive nutrients, growth factors and oxygen but at lower level than the proliferating layer; thus, cells at this layer tend to be less active (quiescent layer). The core layer, on other hand, has almost no access to oxygen and nutrients, and consists mainly of dead cells (necrotic layer) [58]–[60].

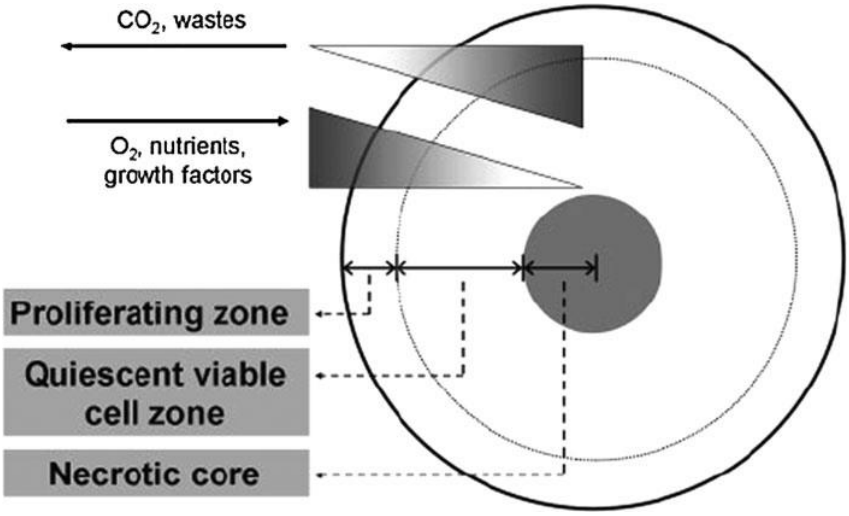

Figure 2.6: A typical 3D cell cultured spheroid includes different layers of cells [6].

Similar to 2D cell culture, 3D cell culture is also able to grow simultaneously two or more different cellular populations (co-cultured spheroid) but it mimics more accurately cellular functions normally observed within living tissues [6]. Last but not least, the three-dimensional model is considered as a bridge between *in vitro* and *in vivo* since using 3D cell culture makes it possible to control and monitor the cell spheroid micro-environment parameters (spheroid size, nutrients and growth factors, temperature, oxygen rate, pH) to a certain extent while remaining as accurate to whole living tissues as possible.

2.4 3D Cell Culture Techniques

A broad collection of tools and techniques are available to grow cells into 3D structures [6], [7], [61]. They are generally classified into two main categories; scaffold and non-scaffold based, and include these common technologies:

1. Scaffold Based Techniques
    - Polymeric Hard Scaffolds
    - Biologic Scaffolds
    - Micropatterned Surface Microplates
2. Non-Scaffold Based Techniques
    - Hanging Drop Microplates
    - Spheroid Microplates containing Ultra-Low Attachment (ULA) coating
    - Microfluidic 3D Cell Culture

2.4.1 Scaffold Based Techniques

Scaffold based techniques are the ones in which cells are grown with the help of a support. The scaffolds act as a physical support system for *in vitro* cell culture. Scaffold techniques also have encouraging application *in vivo* tissue regeneration because they can reconstruct the structural environment of living tissue [62].

2.4.1.1 *Polymeric Hard Material Scaffolds*

In polymeric hard material scaffold technique, 3D spheroid models are created by cultured cells on pre-fabricated scaffolds, or matrices, in order to mimic the tissue ECM. Cells attach, proliferate, and fill the spaces within the scaffold to form 3D structures [63].

Materials used in this technique includes polystyrene (PS) and polycaprolactone (PCL). Common designs include porous disc, electro-spun, and orthogonal layering [64].

Polymeric hard scaffolds are used in two major areas; regenerative medicine and preclinical *in vitro* study. In regenerative medicine, cells are grown on the scaffold and then transplanted to patients to replace degenerative tissue. Presently, scaffolds have been used successfully to engineer bone, cartilage, muscle, ligament, skin, vascular tissues and macula [65]–[67]. For preclinical *in vitro* study, cells are grown on the scaffold in Petri dishes or well plate for tumors modeling and drug studies. Typical thickness of the final scaffold is 150-200 μm; each containing a consistent pore size.

After scaffolds are incorporated (as shown in **Figure 2.7**), cells are placed and treated using procedures similar to that used with 2D cell culture. The arrangement of fibers and pores provides support for the cell to reorganize in three dimensions while it provides full access to nutrient, growth factors, and oxygen, allowing exchange of nutrients, waste material, and gases similar to that seen *in vivo*.

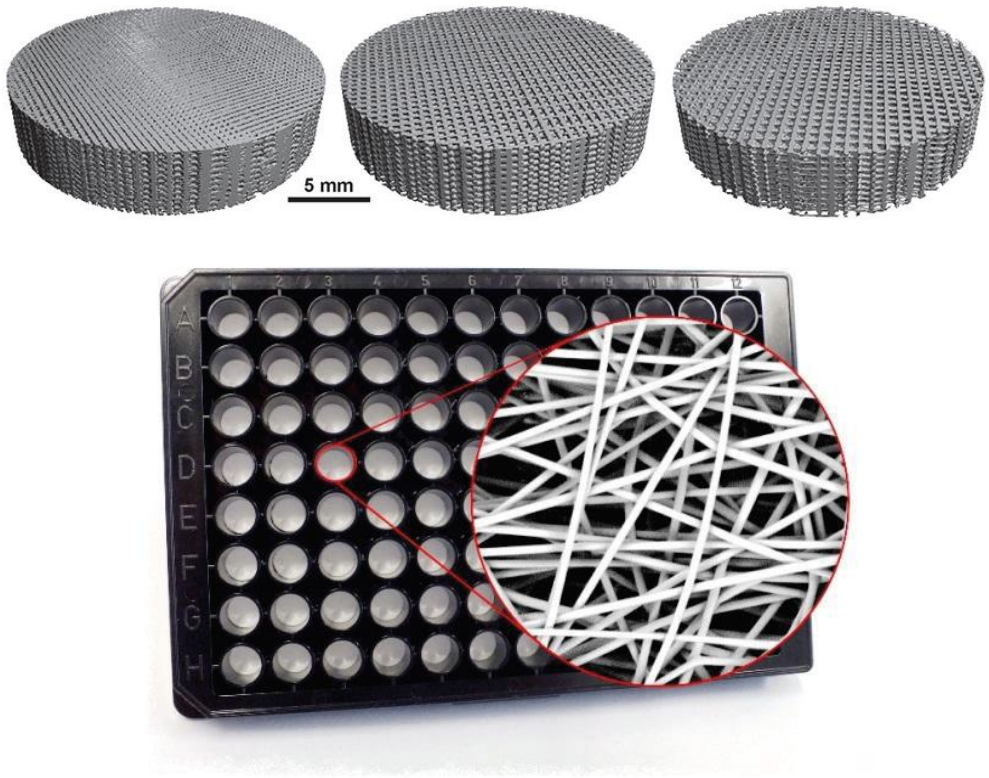

Figure 2.7: Orthogonal layering polymeric scaffolds for 3D cell spheroid forming (top panel) and final joint configuration of polymeric 3D scaffold in 96-wells plate format (bottom panel) [64].

2.4.1.2 *Biological Scaffolds*

A frequently used component of scaffolds is hydrogel, which can be created from natural or biological origin (such as proteoglycans, fibrous proteins, collagen, and gelatin generally found in the *in vivo* ECM). Biological scaffolds offer a matrix for cells to attach and grow into 3D structures as well as the microenvironment with soluble growth factors, hormones, and other nutrients which are often found in *in vivo* environment [68]. The polymer networks used in current hydrogel-based techniques are extensively swollen with water. The cells can be mixed with scaffold proteins in a liquid state (hydrogel) before they are plated in a microplate well, or they can be added, with nutrient mixture, to scaffolds already formed. Since these scaffolds originate from natural sources, they pose

low risk of toxicity and harm to cells while promoting many cellular functions, including increased viability, cell proliferation and cell formation [6], [7], [69]. In many cases, biological scaffolds can also be more advantageous over polymeric hard material scaffolds, as the hydrogel scaffolds can be engineered to associate and dissociate at biological conditions, unlike polymeric scaffolds (**Figure 2.8**). Hydrogels are also used in multi-layer scaffolds to form tissue-like structures, where each cell type is planted in a distinct hydrogel scaffold and the scaffolds are then put together on top of each other. Examples are human skin [70] and human corneal limbal crypts [59].

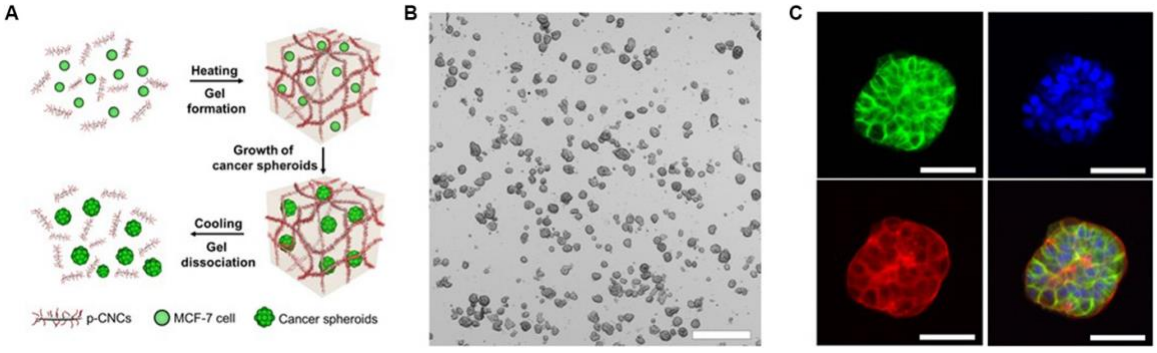

Figure 2.8: An example of hydrogel scaffolds used to encapsulate, grow and release multicellular cancer spheroids (MCSs) of MCF-7 cells using cellulose nanocrystals (CNCs) [71].

2.4.1.3 *Micropatterned Surface Microplates*

Use of micropatterned surface plates is a relatively new technique that takes full advantage of latest advancement made in micro-fabrication technology. Compartments are patterned at micrometer scale on the bottom of the wells in the microplates [64]. Wells can have various shapes – square, round, split pattern (**Figure 2.9**) with different configurations optimized for 3D spheroid forming or cell networking interaction.

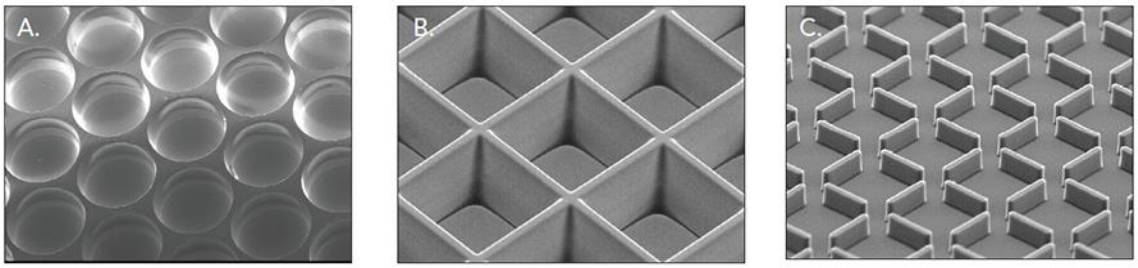

Figure 2.9: Some example of micropatterned surface microplate with different well shapes [64].

The micro-space compartments in each well are coated to create a low adhesion surface to prevent the cells from attaching. Consequently, cells self-assemble to form 3D spheroid structures in the compartment, or to form contiguous cell networks in case of the slit pattern, along the bottom of the well (**Figure 2.9**). The latest studies show that cell spheroids formed using micropatterned surface microplates demonstrate highly different enzyme expression levels and drug response compared to traditional 2D cell culture [72].

2.4.2 Non-Scaffold Based 3D Cell Culture

2.4.2.1 *Hanging Drop Microplates*

The hanging drop plate method is a simple technique that takes advantage of the tendency for cells with no nearby adhesion surface to aggregate into a 3D spheroid structure. In this method, instead of normal wells with a traditional bottom, the plate is equipped with open-bottomed wells. The top of the microplate is just like other conventional microplates, where cells and media can be dispensed (**Figure 2.10**), while a discrete droplet of media sufficient for cellular aggregation forms at the bottom opening of the well due to surface tension [64], [73].

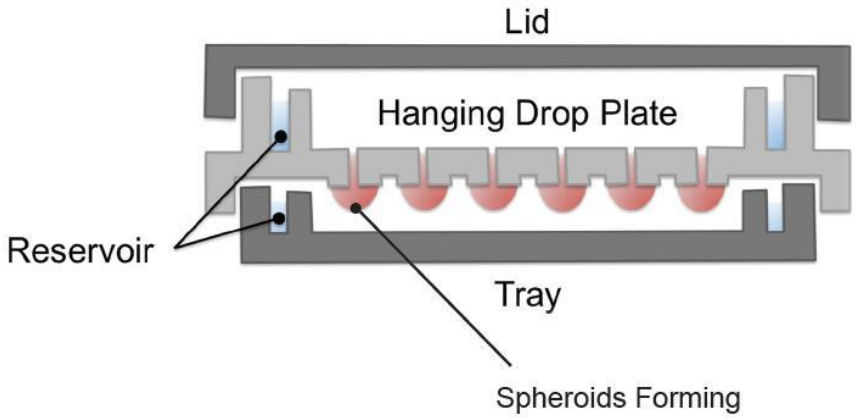

Figure 2.10: Diagram of hanging drop microplates [73].

This method allows the spheroid size to be controlled by adjusting the number of cells placed into each drop. Co-cultured spheroids with separate layers of multiple cell types can also be formed with no specialized equipment required except the hanging drop plate. The drawback of this technique is mobility, as the drops are susceptible to small mechanical shocks which cause spilling of the media and disruption of spheroids formation. Also, for long-term experiments (which is one of the benefits of 3D model over 2D model), spheroids need to be transferred to a second plate containing larger amount of media to prevent drying out as each drop contains limited amount of media.

2.4.2.2 *Spheroid Microplates Containing Ultra-Low Attachment Coating*

Ultra-low attachment (ULA) plates are an alternative to the hanging drop method. A 96- or 384-well microplate is commonly used in this method. The ultra-low attachment surface prevents cell adherence without the need for additional coating and allows a 3D spheroid structure to form. The bottom of each well is rounded instead of flat to conform better to the round multi-cell tissue or tumor spheroid structure. Well bottoms with v-shaped geometry design ensure formation of the spheroids in the middle of the well (**Figure 2.11**). Since the cells still have access to large amount of media and growth

factors, long-term experiment can be carried out in the same plate; without the need for transfer to a second one [64], [74]. Current research that employs ULA coating microplate include neural stem cell spheroid [75] and various immortalized cancer cell lines spheroids for drug screening [74], [76].

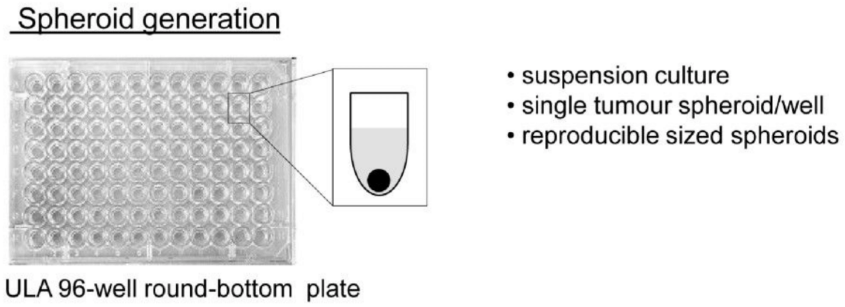

Figure 2.11: Ultra-low attachment (ULA) 96-well round-bottomed plates were used to generate suspension cultures of reproducibly sized, single spheroids in each well [74].

2.4.2.3 *Microfluidic 3D Cell Culture*

One of the ultimate goals of the 3D cell spheroid model as described above is to recreate the three-dimensional structure of living tissues and tumors and to allow cell-cell and cell-ECM interactions. In this method, microfluidic platforms are used to create a spheroid of one or more cell types (co-culture), while introducing a perfusive flow aspect to the cellular environment (**Figure 2.12**); permitting continuous addition of nutrition and oxygen as well as introduction of chemicals or drugs [73], [76], [77].

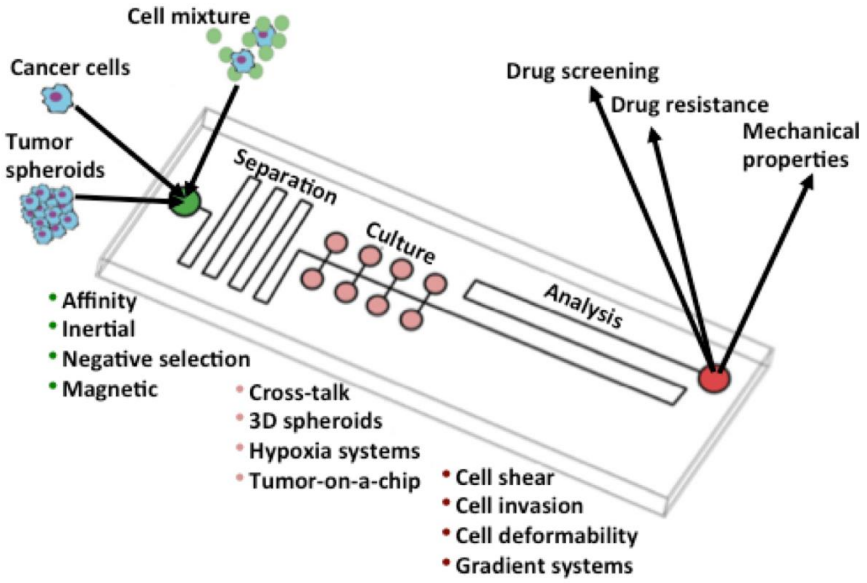

Figure 2.12: Diagram of a microfluid design of 3D spheroid model for drug screening [77].

Microfluidic devices use physical barriers composed of glass, silicon, and polymers, including polydimethylsiloxane (PDMS), polymethylmethacrylate (PMMA), polycarbonate (PC) and polystyrene (PS) [73]. Supporting matrix (such as collagen) can also be used to help 3D spheroid assembly and promote cell-cell and cell-ECM interactions. Current research directions that employs microfluidic systems include bone marrow mesenchymal stem cells (BMSCs) [78], murine embryonic stem cells [79], and carcinoma-associated fibroblasts invasion [80].

2.5 A Novel Matrix Free Spheroid Technique

2.5.1 Introduction

A matrix-free method is used in this study to create 3D spheroids of various cell types, including primary astrocyte cells, glioma brain tumor cells, and primary endothelial cells. This technique provides a simple but efficient, cost-effective method to

generate 3D spheroids that does not require matrix, scaffolds, or expensive plates but still retains the benefits of 3D cell models, including co-culturing of spheroids of different cell types, drug screening, and long-term interaction with biomaterial. Here we use a proprietary technique (Provisional patent number 61645328, filed with the U.S. Patent office) that uses a matrix-free system (Nanogaia #SSD-01, Ruston, LA - http://www.nanogaia.com/) with standard suspension cell culture plate. Also, this technique does not require special cell culture media and can be used for long periods of time after coating to enable much longer-term experiments than traditional 2D cell model. Since this method does not require any specialized equipment or techniques, it is suitable for both high-throughput studies (best for drug screening), and high-content studies (best for study cell interaction with drugs and biomaterials). The lack of a solid matrix provides the freedom to manipulate spheroids in our system in many ways.

2.5.2 Advantages of Our System

The system is advantageous in that it

- Provides matrix free generation of spheroids.
- Is simple and inexpensive.
- Can produce spheroids in large numbers.
- Can co-culture spheroids of two or more different cell types.
- Allows long term cell culture (up to one month compared to 3-7 days in 2D models).
- Has a wide variety of application, not limited to cell culture studies [81].

2.6 Comparison of CuHARS, CuNPs and HNTs

Copper nanoparticles (CuNPs) used in this research are copper based particles with size within range from 40-60 nm and have antifungal/antibacterial features due to their nano size and a high surface to volume ratio [82]. The stress/toxicity of CuNPs is produced when they interact with the membranes of cells/microbial and release metal ions into medium. Halloysite nanotubes (HNTs) are aluminosilicate clay mineral (chemical formula: $Al_2Si_2O_5(OH)_4$) and have hollow tubular structure with outer diameter 50 ± 5 nm; inner lumen 10 - 15 nm; and length 1200 ± 300 nm. The outer surface of HNTs is negative charged while the inner core is positive charged. Materials such as proteins, DNA, cancer drugs can be loaded to the hollow lumen of HNTs and then released in a controlled manner [83], [84]. CuHARS as previously described, is a self-assembled copper-containing biohybrid with the amino acid dimer cystine that forms high-aspect ratio structures [9]–[11], [14]. CuHARS has both bio-compatible and bio-degradable features which makes it a potential candidate to be used as a delivery system for drug treatments and/or cell growth promotions. Structure comparison of three materials using scanning electron microscopy (SEM) is shown in **Figure 2.13**.

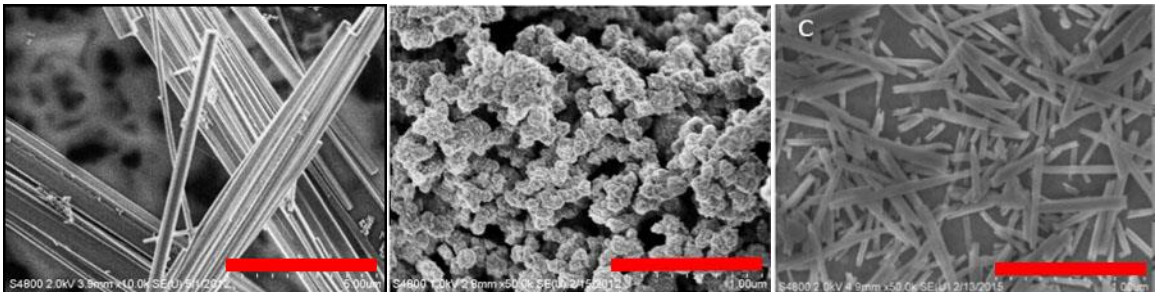

Figure 2.13: Side by side comparison of three materials, CuHARS (left panel), CuNPs (middle panel) and HNTs (right panel). Scale bars = 5 µm (left panel) and 1 µm (middle and right panels) [10], [85].

CHAPTER 3

COMPARISON OF TWO-DIMENSIONAL AND THREE-DIMENSIONAL CELL MODELS

3.1 Introduction

As previous described, three-dimensional (3D) cell models hold several advantages over traditional two-dimensional (2D) cell culture. In particularly, they more accurately mimic cell morphology, cell-cell interaction, and cell-ECM interaction in living tissues, which in turn provides a better response in drug screening, and allows performance of a much longer-term experiment than 2D model, which can give more insights into how the cells interact with biomaterials.

The goal of this chapter is to demonstrate the difference between two-dimensional and three-dimensional cell models in cell morphology, growth, and interaction with materials (Copper nanoparticles – CuNPs, Copper High Aspect Ratio Structure – CuHARS [9]–[11] and halloysite nanotubes – HNTs). The study results will allow us to better understand cell behavior in different environments before going to *in vivo.*

3.2 Materials and Methods

3.2.1 Cell Types

Rat brain glioma cells CRL-2303 (C6/lacZ7) were obtained from American Type Culture Collection (ATCC) and cultured in CRL-2303 media containing 10% FBS, 1%

non-essential amino acid solution, and 0.5% penicillin/streptomycin (**Appendix A, Section A.1)**.

Astrocytes derived from primary, newborn Sprague/Dawley rat brain cortices were cultured in astrocyte medium (Ham's F-12K) containing 10% Horse serum and other components (**Appendix A, Section A.2)**.

3.2.2 Methods

To test the difference between the way 2D and 3D cell models interact with biomaterials, normal brain astrocytes and brain tumor cells were plated in a cell culture 48 wells plate at the density of 20,000 cells/mL (astrocyte) and 10,000 cells/mL (brain tumor) in 2D model and grown in an incubator with 5% CO_2 and at 37°C for 5 days *in vitro* (DIV) in case of primary astrocytes and 3 DIV with glioma cells before adding the biomaterials.

Normal brain astrocytes and brain tumor cells were grown in suspension with a density of 200,000 cells/mL in 3D model. After cell spheroids were developed for 7 DIV, biomaterials were added to the fully formed spheroids at different concentrations.

3.2.3 Materials

Three different types of materials were used to study the difference in cell-materials interaction in both models, copper nanoparticles (CuNPs) (Sigma, 50-100 nm in diameter), copper high aspect ratio structure (CuHARS) and halloysite nanotubes (HNTs).

3.2.4 DAPI Staining

DAPI (4,6-Diamidino-2-phenylindole, dihydrochloride) was prepared according to **Appendix E** to stain nuclei as a way to confirm cell viability and compare nuclei of primary astrocytes and gliomas.

3.2.5 Microscopy

A Leica DMI 6000B inverted microscope was used to collect bright field and phase microscopic images of the cells. For fluorescent imaging, a Leica EL6000 light source was used. For GFAP imaging, excitation in the blue portion of the light spectrum (~475 nm) was required. To view DAPI-stained nuclei, excitation light in the ultraviolet range (~400 nm) was required.

3.3 Results

3.3.1 Interactions of Materials with Cells in 2D Model

3.3.1.1 *Interaction with CuHARS*

Figure 3.1 and **3.2** show the interaction of primary astrocytes with different concentrations of CuHARS over time. Phase microscopy was used to record the cells, while bright field microscopy was used to capture the CuHARS with better contrast, as needed because the material consists of both copper metal and the amino acid cystine).

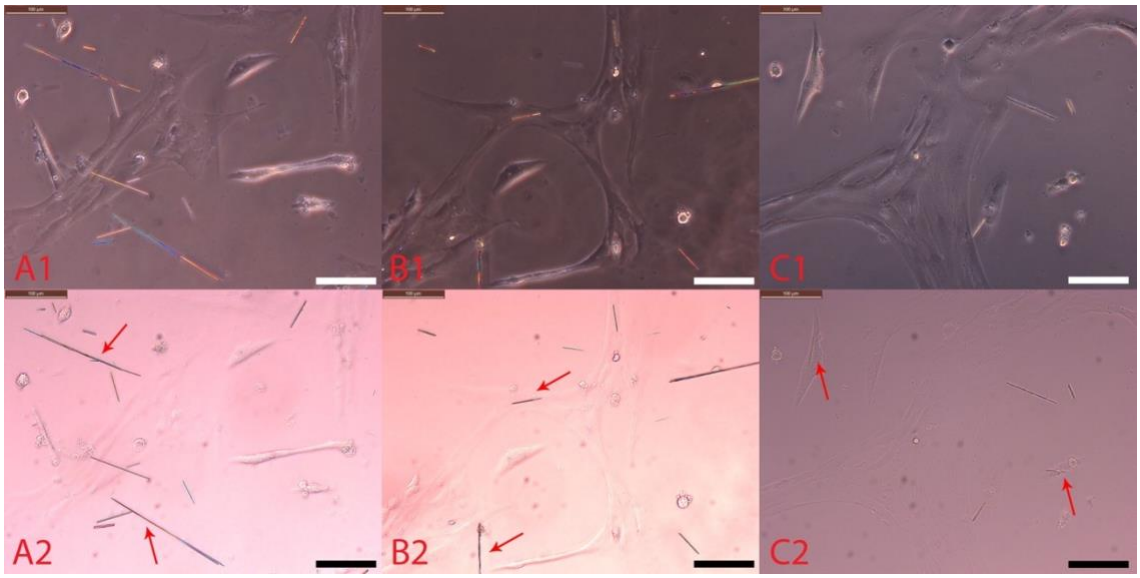

Figure 3.1: Interaction of CuHARS (1 µg/ml concentration) with primary astrocytes. Cells were plated at 20k cells/well and CuHARS were added 5 days after cells attached. Panels 1 and 2 were taken of the same areas with pictures A1, B1, C1 were taken using phase microscopy, pictures A2, B2, C2 were taken using bright field microscopy. Pictures were taken at 0h (left), 24 (center) and 96h (right) post addition at 200x magnification. Red arrows indicate CuHARS. Scale bar = 100 µm.

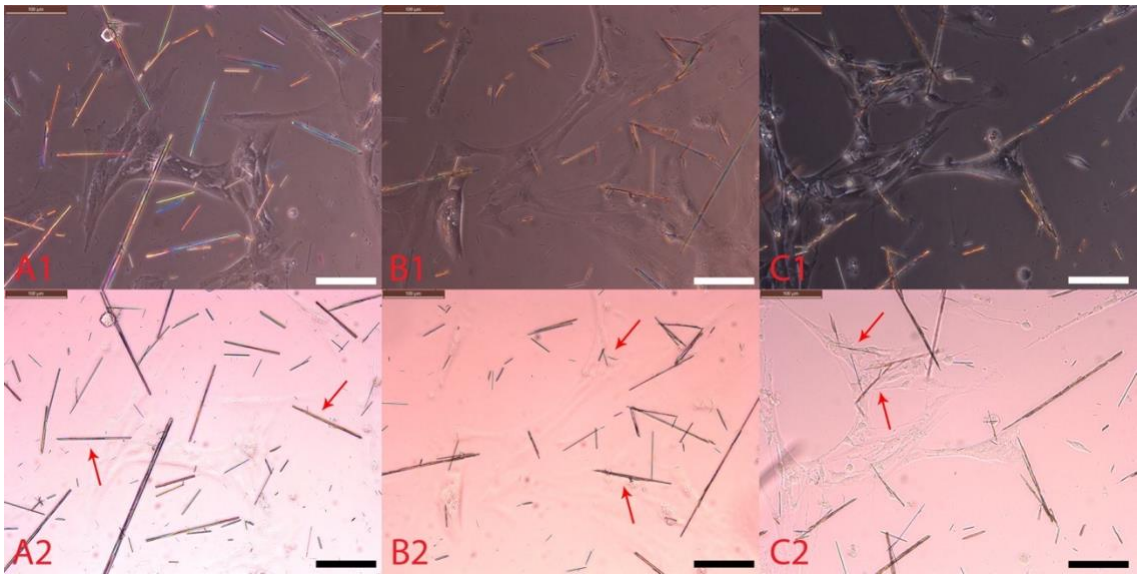

Figure 3.2: Interaction of CuHARS (10 µg/ml concentration) with primary astrocytes. Cells were plated at 20k cells/well and CuHARS were added 5 days after cells attached. Panels 1 and 2 were taken of the same areas with pictures A1, B1, C1 were taken using phase microscopy, pictures A2, B2, C2 were taken using bright field microscopy. Pictures were taken at 0h (left), 24 (center) and 96h (right) post addition at 200x magnification. Red arrows indicate CuHARS. Scale bar = 100 µm.

As shown in **Figure 3.1** and **3.2**, CuHARS started to bind to the astrocytes as soon as the 24h timepoint, and the small CuHARS started to break down at the 96h timepoint, as indicated by the smaller CuHARS disappearing in panel C2 (96h) compared to panel A2 (0h) in both **Figure 3.1** and **3.2**.

Figure 3.3 displays the astrocytes 4 DIV after interaction with the CuHARS at different concentrations. In the low and medium concentration 1 and 5 µg/ml (panel B and C), the astrocytes showed little to no sign of stress or toxicity (cell loss).

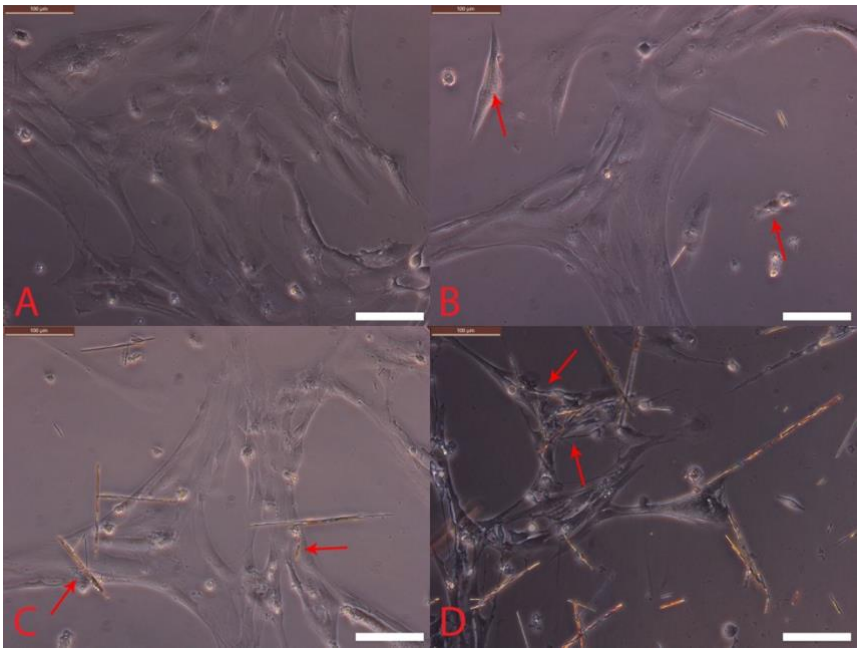

Figure 3.3: Interaction of CuHARS with primary astrocytes. Cells were plated at 20k cells/well and CuHARS were added 5 days after cells attached. Pictures were taken 96h post addition: control (panel A), 1 µg/ml CuHARS (panel B), 5 µg/ml CuHARS (panel C) and 10 µg/ml CuHARS (panel D) using phase microscopy at 200x magnification. Scale bar = 100 µm.

The same experiment was also carried out with glioma cells. **Figure 3.4** and **3.5** show the interaction of glioma cells with different concentrations of CuHARS over time. At low concentration (1 µg/ml), as in the case of primary astrocytes, CuHARS appeared

to be non-toxic to glioma cells, as indicated by the increase in cell number and the change in media color from red to yellow, an indicator of cell metabolism (**Figure 3.4** panel C1). At high concentration (10 µg/ml) as displayed in **Figure 3.5** panel C1, the media color was not as yellow as it was at low concentration. However, the cells had a similar morphology at both low and high CuHARS concentration, which suggested that even at high concentration, CuHARS did not cause drastic stress to the cells.

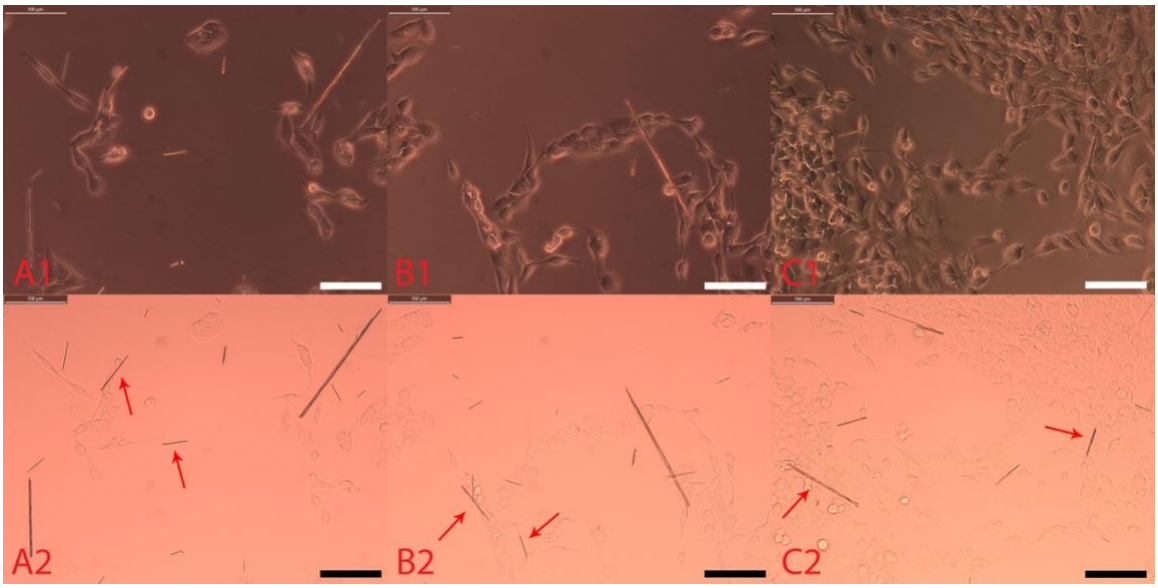

Figure 3.4: Interaction of CuHARS (1 µg/ml concentration) with brain tumor cells. Cells were plated at 10k cells/well and CuHARS were added 2 days after cells attached. Panels 1 and 2 were taken of the same areas with pictures A1, B1, C1 were taken using phase microscopy, pictures A2, B2, C2 were taken using bright field microscopy. Pictures were taken at 0h (left), 24 (center) and 96h (right) post addition at 200x magnification. Red arrows indicate CuHARS. Scale bar = 100 µm.

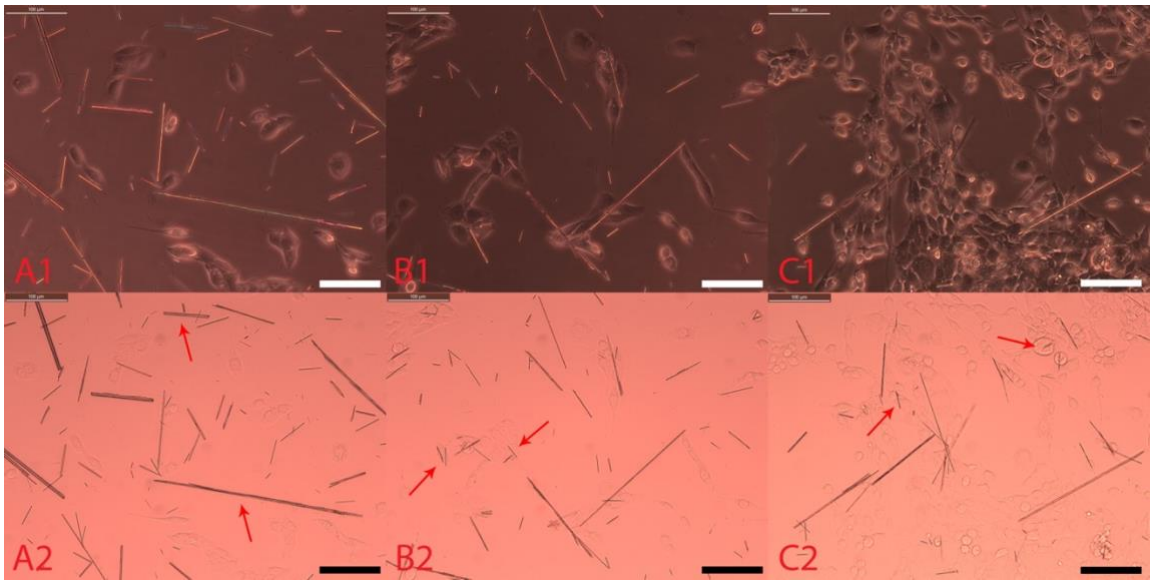

Figure 3.5: Interaction of CuHARS (10 µg/ml concentration) with brain tumor cells. Cells were plated at 10k cells/well and CuHARS were added 2 days after cells attached. Panels 1 and 2 were taken of the same areas with pictures A1, B1, C1 were taken using phase microscopy, pictures A2, B2, C2 were taken using bright field microscopy. Pictures were taken at 0h (left), 24 (center) and 96h (right) post addition at 200x magnification. Red arrows indicate CuHARS. Scale bar = 100 µm.

Figure 3.4 and **Figure 3.5** also show that with tumor cells, as with primary astrocytes, CuHARS started to bind to the cells as soon as 24h timepoint and the small CuHARS started to break down at 96h timepoint, as shown by the clearing of smaller CuHARS in panel C2 (96h) compared to panel A2 (0h) in both figures.

Side by side comparison of glioma 4 DIV after interaction with the CuHARS is displayed in **Figure 3.6** at low and medium concentrations of CuHARS (1 µg/ml and 5 µg/ml). The CuHARS showed little to no toxicity toward the brain tumor cells, indicated by the media color turning to yellow (acidic) as the result of high cell metabolism. In high concentrations of CuHARS (10 µg/ml), the cells appeared to be stressed and under toxicity as the media remained reddest as well as the biggest gap in cell growth. In

contrast, the control media had the yellowest color and the shortest gap in cell growth since the cells were the healthiest.

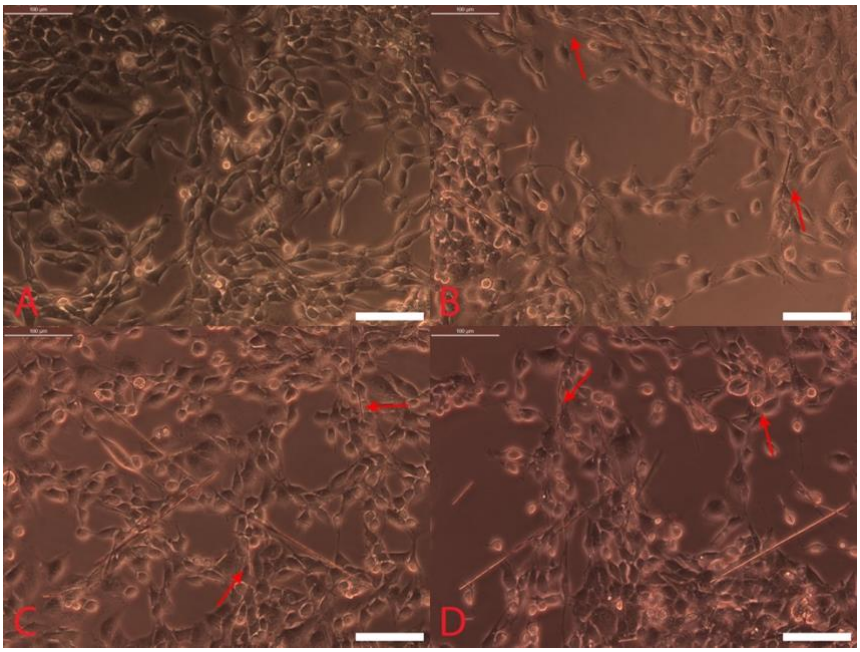

Figure 3.6: Interaction of CuHARS with brain tumor cells. Cells were plated at 10k cells/well and CuHARS were added 2 days after cells attached. Pictures were taken 96h post addition: control (panel A), 1 µg/ml CuHARS (panel B), 5 µg/ml CuHARS (panel C) and 10 µg/ml CuHARS (panel D) using phase microscopy at 200x magnification. Scale bar = 100 µm.

3.3.1.2 *Interaction with CuNPs*

Figure 3.7 and **3.8** show the interaction of primary astrocytes with different concentrations of CuNPs over time. Phase microscopy was used to record the cells, while bright field microscopy was used to capture the CuNPs with better contrast.

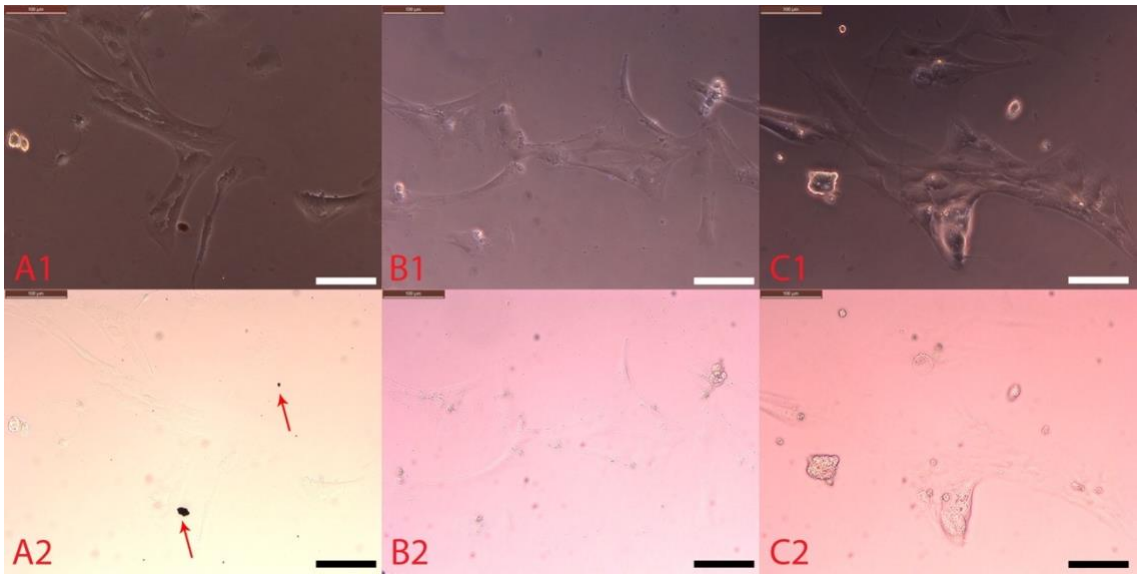

Figure 3.7: Interaction of CuNPs (0.5 µg/ml concentration) with primary astrocytes. Cells were plated at 20k cells/well and CuNPs were added 5 days after cells attached. Panels 1 and 2 were taken of the same areas with pictures A1, B1, C1 were taken using phase microscopy, pictures A2, B2, C2 were taken using bright field microscopy. Pictures were taken at 0h (left), 3h (center) and 24h (right) post addition at 200x magnification. Red arrows indicate CuNPs. Scale bar = 100 µm.

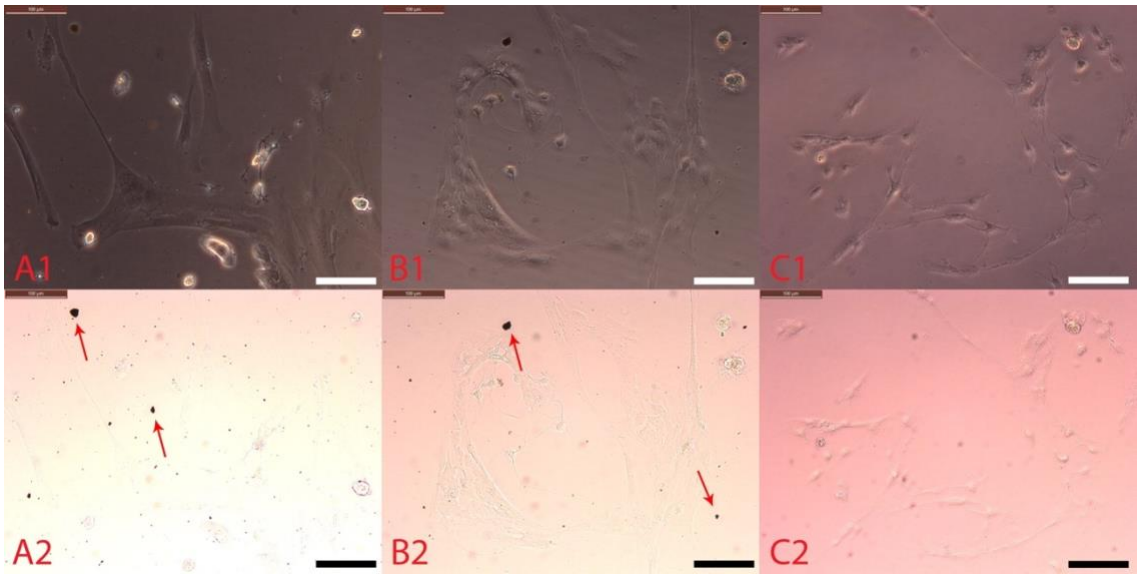

Figure 3.8: Interaction of CuNPs (5 µg/ml concentration) with primary astrocytes. Cells were plated at 20k cells/well and CuNPs were added 5 days after cells attached. Panels 1 and 2 were taken of the same areas with pictures A1, B1, C1 were taken using phase microscopy, pictures A2, B2, C2 were taken using bright field microscopy. Pictures were taken at 0h (left), 3h (center) and 24h (right) post addition at 200x magnification. Red arrows indicate CuNPs. Scale bar = 100 µm.

As shown in **Figure 3.7** and **Figure 3.8**, CuNPs break down begins rapidly, completing in 3 h for the low concentration (0.5 µg/ml) and after 24 h for all concentrations. Also, the CuNPs appeared to be very toxic to the astrocytes as the cells at both low and high concentrations (0.5 µg/ml and 5 µg/ml, respectively) of CuNPs already showed signs of stress at 24h timepoint.

Side by side comparison of primary astrocyte 4 DIV after interaction with the CuNPs is shown in **Figure 3.9**. All concentrations of CuNPs (0.5 µg/ml, 2.5 µg/ml, and 5 µg/ml) caused stress to the astrocytes, as indicated by the cells becoming round and shrunken. In contrast, the low and medium concentrations of CuHARS (1 µg/ml and 5 µg/ml) showed little to no toxicity toward the brain tumor cells (as shown in **Figure 3.3**).

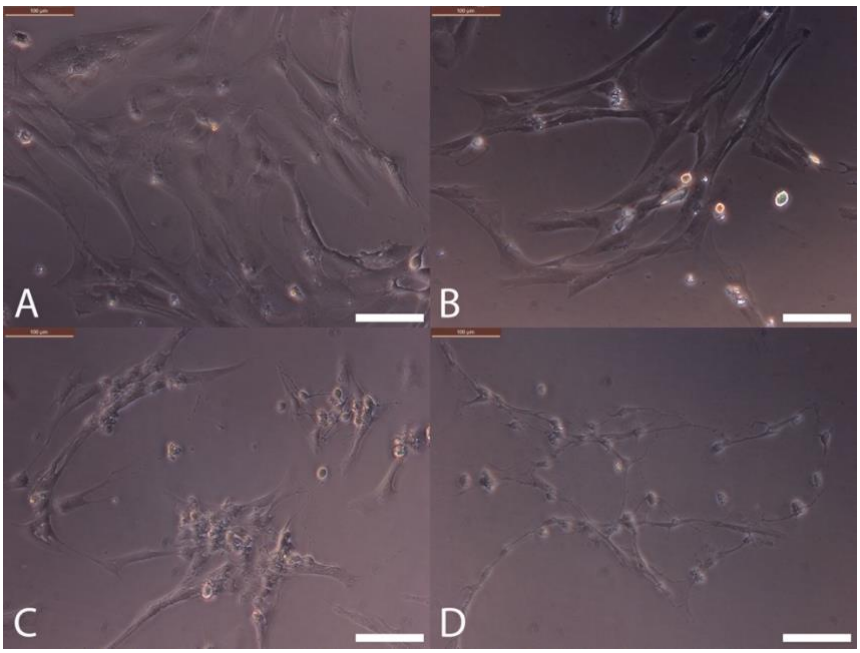

Figure 3.9: Interaction of CuNPs with primary astrocytes. Cells were plated at 20k cells/well and CuNPs were added 5 days after cells attached. Pictures were taken 96h post addition: control (panel A), 0.5 µg/ml CuNPs (panel B), 2.5 µg/ml CuNPs (panel C) and 5 µg/ml CuNPs (panel D) using phase microscopy at 200x magnification. Scale bar = 100 µm.

Figure 3.10 and **3.11** show the interaction of glioma cells with different concentrations of CuNPs over time. Both low and high concentrations (0.5 µg/ml and 5 µg/ml) of CuNPs broke down entirely within 3h for the low concentration (0.5 µg/ml) and within 24h for all concentrations similar to the case of primary astrocytes.

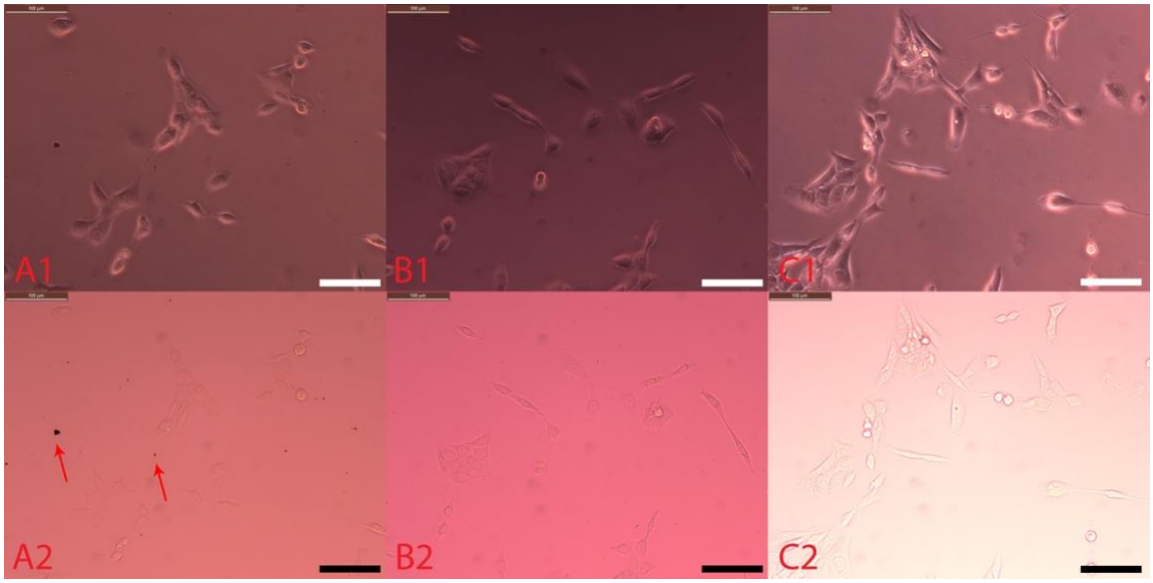

Figure 3.10: Interaction of CuNPs (0.5 µg/ml concentration) with brain tumor cells. Cells were plated at 20k cells/well and CuNPs were added 5 days after cells attached. Panels 1 and 2 were taken of the same areas with pictures A1, B1, C1 were taken using phase microscopy, pictures A2, B2, C2 were taken using bright field microscopy. Pictures were taken at 0h (left), 3h (center) and 24h (right) post addition at 200x magnification. Red arrows indicate CuNPs. Scale bar = 100 µm.

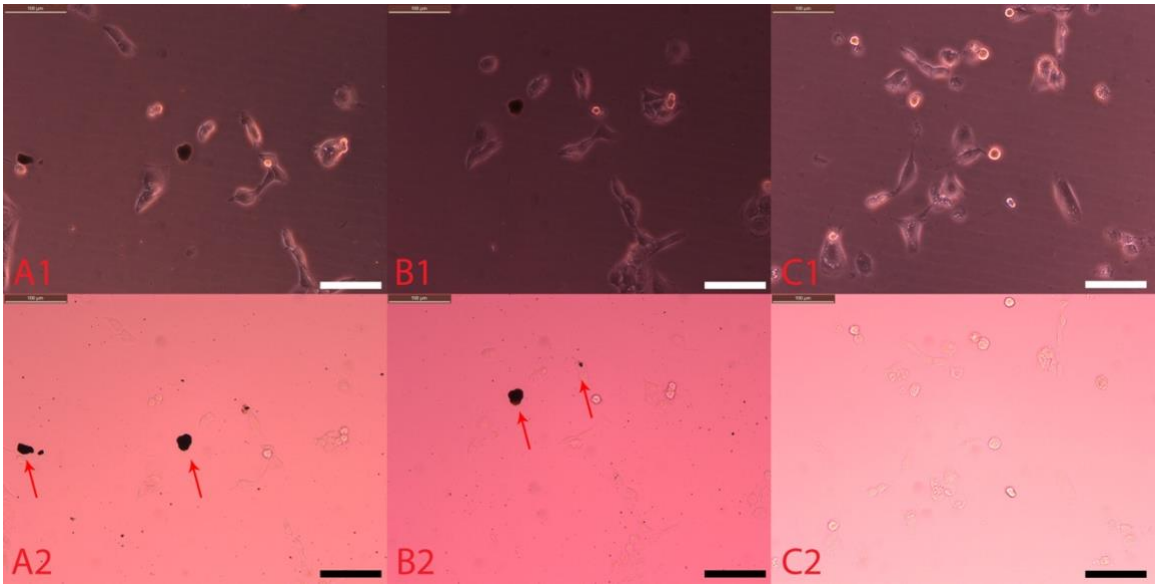

Figure 3.11: Interaction of CuNPs (5 µg/ml concentration) with brain tumor cells. Cells were plated at 20k cells/well and CuNPs were added 5 days after cells attached. Panels 1 and 2 were taken of the same areas with pictures A1, B1, C1 were taken using phase microscopy, pictures A2, B2, C2 were taken using bright field microscopy. Pictures were taken at 0h (left), 3h (center) and 24h (right) post addition at 200x magnification. Red arrows indicate CuNPs. Scale bar = 100 µm.

Figure 3.10 and **3.11** also indicate that the CuNPs cause some stress to the glioma cells at both concentrations (0.5 µg/ml and 5 µg/ml) as the cells became stressed (distinguished by the round shape and shrunk cell body) at the 24h timepoint (panel C1 of both figures).

Side by side comparison of glioma cells 4 DIV after interaction with the CuNPs is shown in **Figure 3.12**. Medium and high concentrations of CuNPs (2.5 µg/ml and 5 µg/ml) caused stress to the astrocytes, as indicated by the cells becoming round and shrinking, but at the low concentration of CuNPs (0.5 µg/ml), glioma cells recovered from initial stress, as indicated by the cell proliferation. However, compared to the CuHARS with the same amount of copper (as shown in **Figure 3.6**), CuNPs appeared to be more toxic toward the brain tumor cells as cell number goes down and the colors of

the media in all concentrations of CuNPs are redder than the colors of the media with respective concentrations of CuHARS. Thus, cell metabolism went decreased more by stress/toxicity caused by CuNPs than by CuHARS.

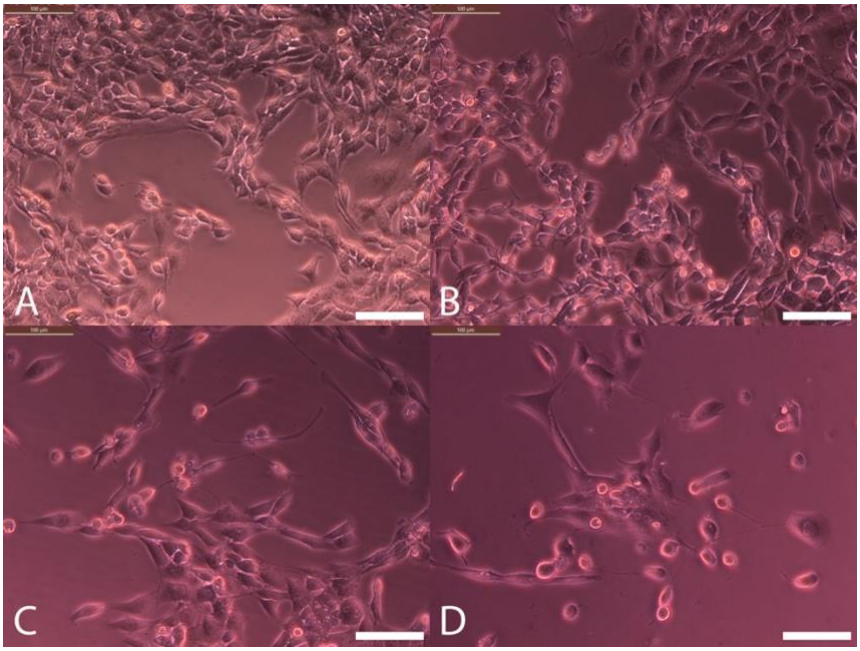

Figure 3.12: Interaction of CuNPs with brain tumor cells. Cells were plated at 10k cells/well and CuNPs were added 5 days after cells attached. Pictures were taken 96h post addition: control (panel A), 0.5 µg/ml CuNPs (panel B), 2.5 µg/ml CuNPs (panel C) and 5 µg/ml CuNPs (panel D) using phase microscopy at 200x magnification. Scale bar = 100 µm.

3.3.1.3 *Interaction with HNTs*

Figure 3.13 and **3.14** show the interaction of primary astrocytes with different concentrations of HNTs over time. Phase microscopy was used to record the cells, while fluorescent microscopy was used to capture the HNTs (green color on black background). The figures show that the fluorescent HNTs were taken up by or bound to the primary astrocytes over time, as indicated by the clearance in background and the amount of HNTs bound on or around the cells at 96h timepoint compared to 0h timepoint. Also,

HNTs at high concentration (10 µg/ml) appeared to be toxic to the astrocytes, as shown at 96h timepoint, as indicate by the rounder shape and shrunken size.

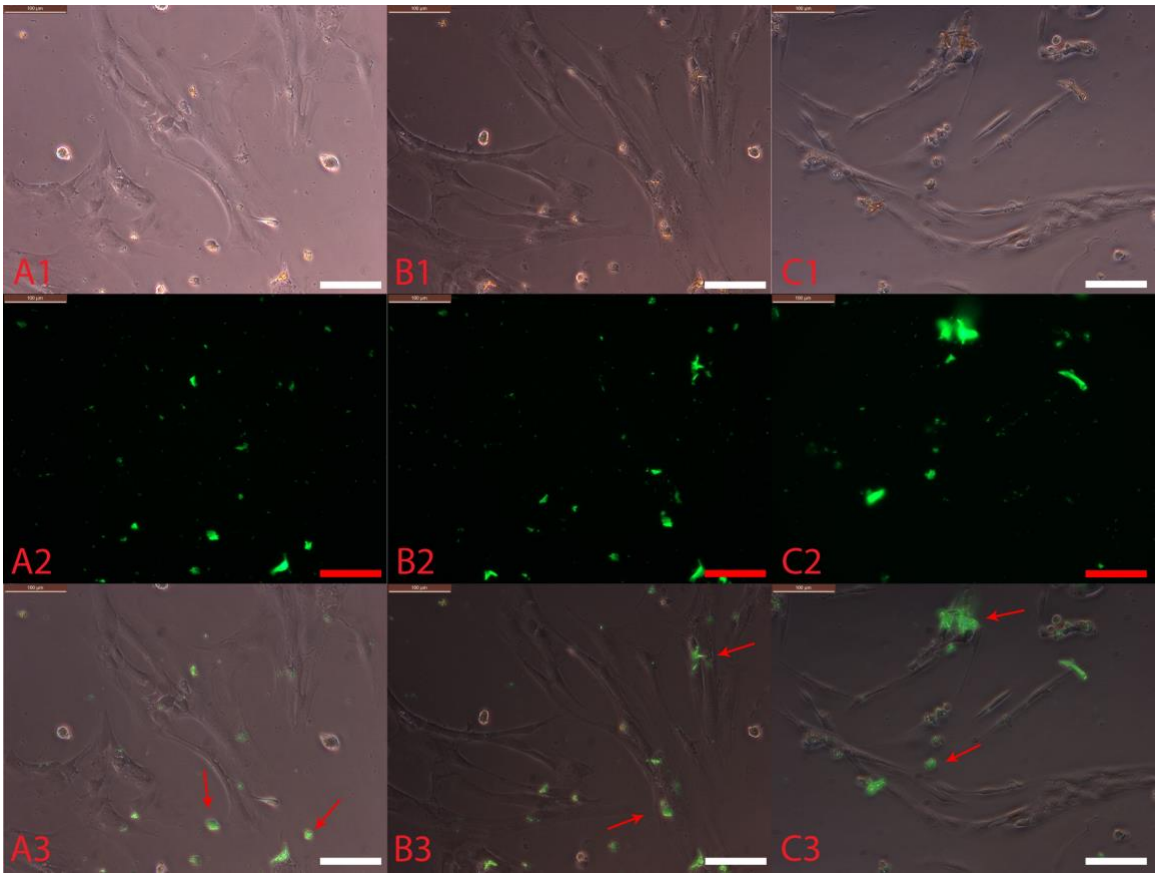

Figure 3.13: Interaction of fluorescent HNTs (1 µg/ml concentration) with primary astrocytes. Cells were plated at 20k cells/well and HNTs were added 5 days after cells attached. Panels 1 and 2 were taken of the same areas with pictures A1, B1, C1 were taken using phase microscopy, pictures A2, B2, C2 were taken using fluorescent microscopy. Panel 3 is the combination of panels 1 and 2. Pictures were taken at 0h (left), 24h (center) and 96h (right) post addition at 200x magnification. Red arrows indicate fluorescent HNTs. Scale bar = 100 µm.

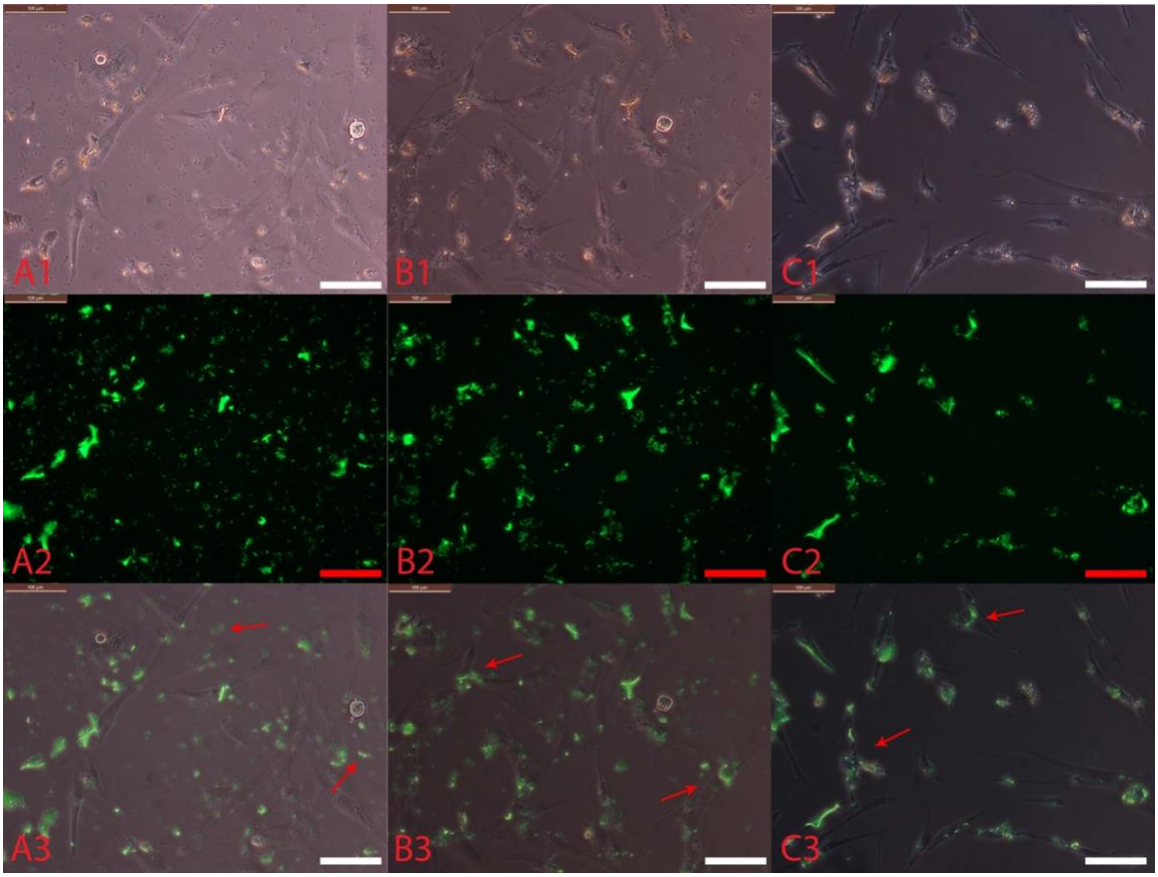

Figure 3.14: Interaction of fluorescent HNTs (10 µg/ml concentration) with primary astrocytes. Cells were plated at 20k cells/well and HNTs were added 5 days after cells attached. Panels 1 and 2 were taken of the same areas with pictures A1, B1, C1 were taken using phase microscopy, pictures A2, B2, C2 were taken using fluorescent microscopy. Panel 3 is the combination of panels 1 and 2. Pictures were taken at 0h (left), 24h (center) and 96h (right) post addition at 200x magnification. Red arrows indicate fluorescent HNTs. Scale bar = 100 µm.

Primary astrocytes 4 DIV after interaction are compared side-by-side for the different concentrations of fluorescent HNTs in **Figure 3.15** as most of the materials were taken up by the cells. A low concentration of HNTs (1 µg/ml) was not toxic to the astrocytes while medium and high HNTs concentrations (5, 10 µg/ml) caused some stress to the cells as indicated by the shrunken cell bodies (**Figure 3.15** panel C, D).

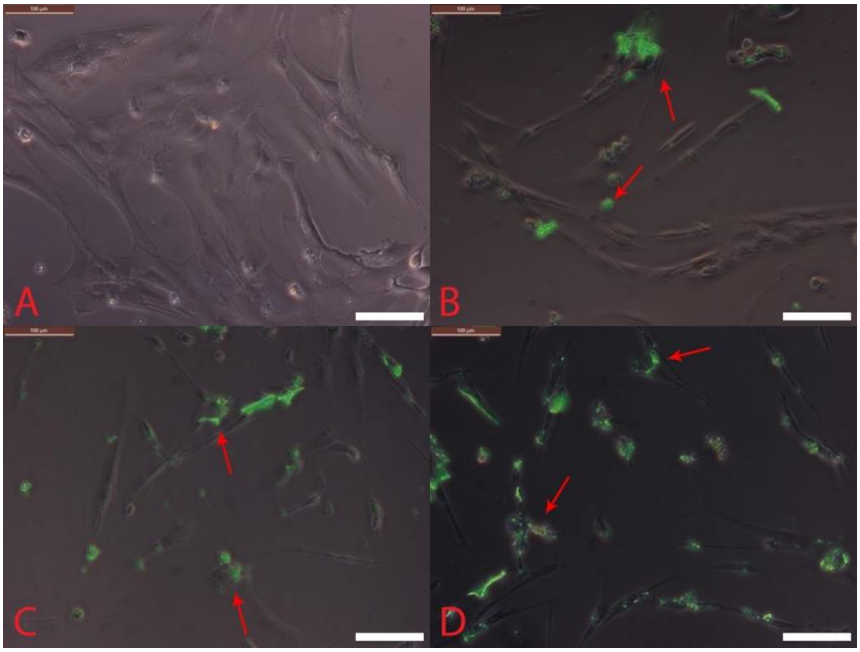

Figure 3.15: Interaction of fluorescent HNTs with primary astrocytes. Cells were plated at 20k cells/well and HNTs were added 5 days after cells attached. Pictures were taken 96h post addition: control (panel A), 1 µg/ml HNTs (panel B), 5 µg/ml HNTs (panel C) and 10 µg/ml HNTs (panel D) using phase and fluorescent microscopy at 200x magnification. Scale bar = 100 µm.

The same experiment was also carried out with glioma cells and fluorescent HNTs. **Figure 3.16** and **3.17** show the interaction of glioma cells with different concentrations of HNTs over time. As in the case with the astrocytes, phase microscopy was used to record the cells, while fluorescent microscopy was used to capture the HNTs (green color on black background).

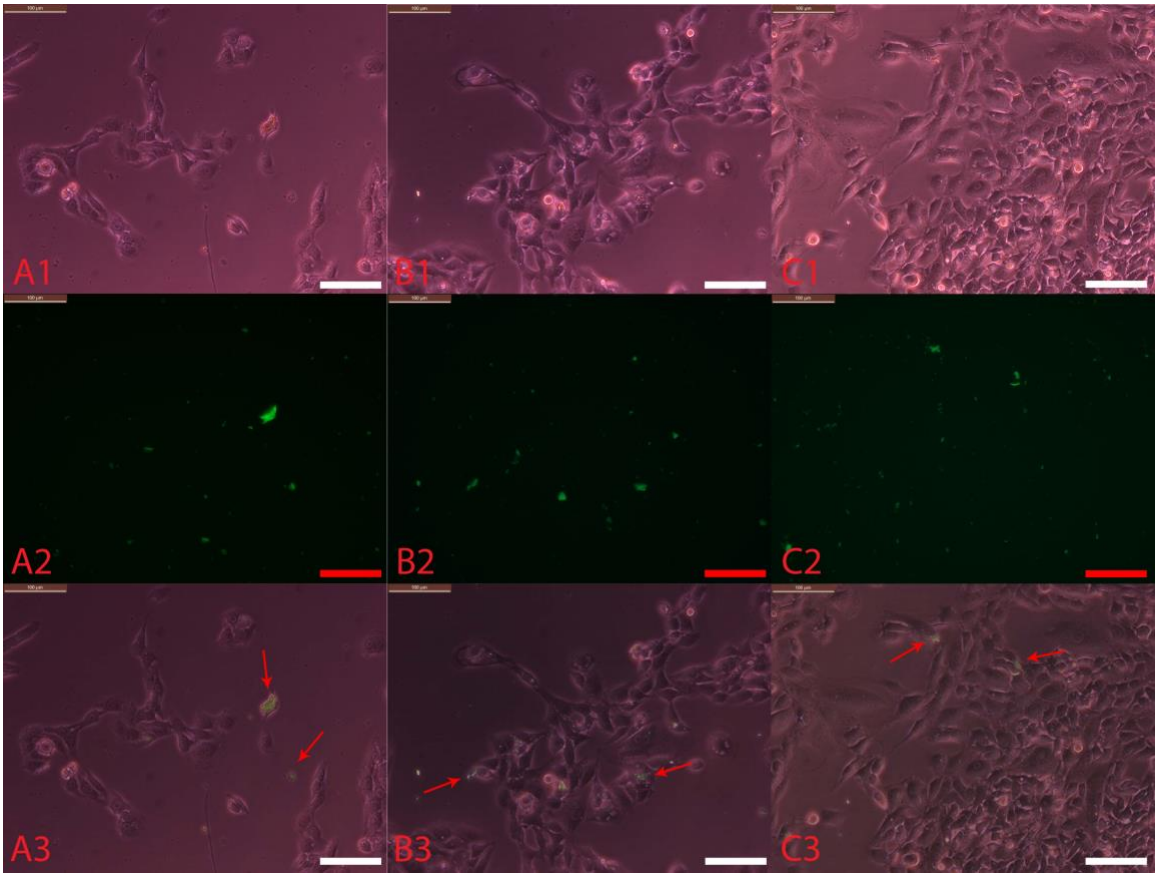

Figure 3.16: Interaction of fluorescent HNTs (1 µg/ml concentration) with brain tumor cells. Cells were plated at 10k cells/well and HNTs were added 2 days after cells attached. Panels 1 and 2 were taken of the same areas with pictures A1, B1, C1 were taken using phase microscopy, pictures A2, B2, C2 were taken using fluorescent microscopy. Panel 3 is the combination of panels 1 and 2. Pictures were taken at 0h (left), 24h (center) and 96h (right) post addition at 200x magnification. Red arrows indicate fluorescent HNTs. Scale bar = 100 µm.

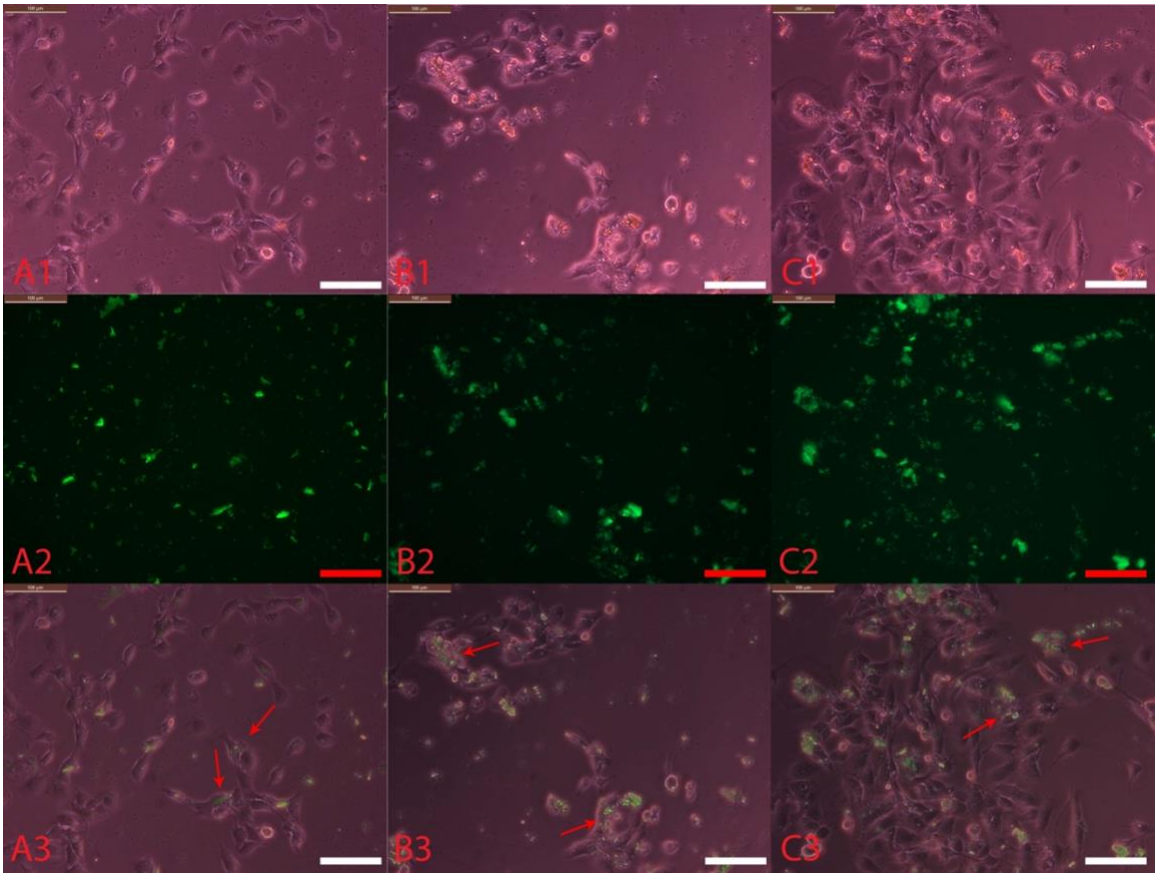

Figure 3.17: Interaction of fluorescent HNTs (10 µg/ml concentration) with brain tumor cells. Cells were plated at 10k cells/well and HNTs were added 2 days after cells attached. Panels 1 and 2 were taken of the same areas with pictures A1, B1, C1 were taken using phase microscopy, pictures A2, B2, C2 were taken using fluorescent microscopy. Panel 3 is the combination of panels 1 and 2. Pictures were taken at 0h (left), 24h (center) and 96h (right) post addition at 200x magnification. Red arrows indicate fluorescent HNTs. Scale bar = 100 µm.

Figure 3.16 and **Figure 3.17** show that the fluorescent HNTs were also taken up by or bound to the cancer cells over time, as indicated by the amount of HNTs bound on or around the cells at 96h timepoint compared to 0h timepoint. Unlike the astrocytes, fluorescent HNTs did not appear to cause any stress to the cancer cells at both low and high concentrations.

Side by side comparison of glioma cells 4 DIV after interaction with the different concentrations of fluorescent HNTs is shown in **Figure 3.18**. Most of the materials were

taken up by or bound to the cells. All concentrations of HNTs (1, 5 and 10 µg/ml) were not toxic to the cancer cells as indicated by cell proliferation and no round/shrunk cells (**Figure 3.18** panel B, C, D).

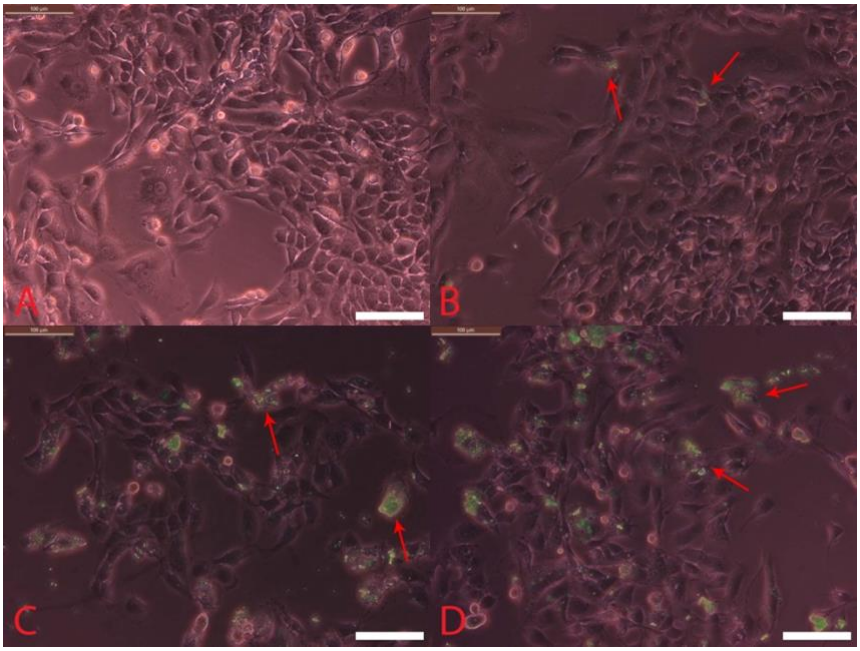

Figure 3.18: Interaction of fluorescent HNTs with brain tumor cells. Cells were plated at 10k cells/well and HNTs were added 2 days after cells attached. Pictures were taken 96h post addition: control (panel A), 1 µg/ml HNTs (panel B), 5 µg/ml HNTs (panel C) and 10 µg/ml HNTs (panel D) using phase microscopy at 200x magnification. Scale bar = 100 µm.

3.3.2 Interactions of Materials with Cells in 3D Model

3.3.2.1 *3D Spheroid Forming*

An example of a 3D spheroid assembled using the Nanogaia kit is shown in **Figure 3.19**. The kit allowed the spheroid (made from primary astrocyte in this case) to form in less than 24h.

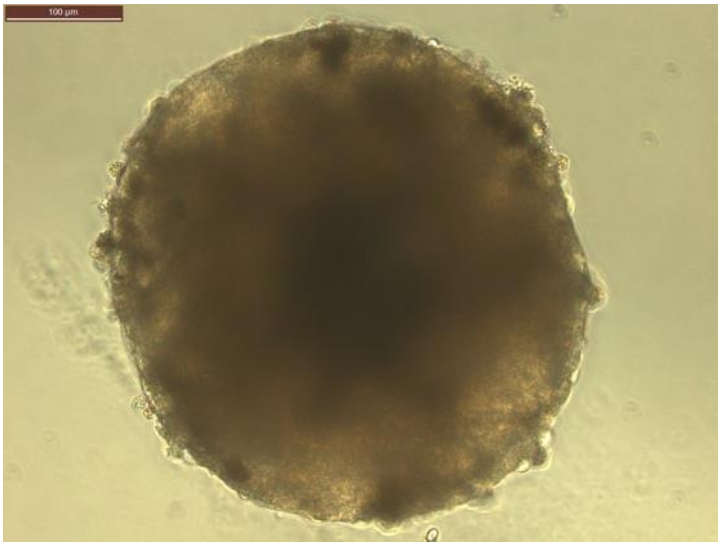

Figure 3.19: 3D spheroid of primary astrocyte cells made using matrix free method. (5 DIV spheroid treated with CuNPs 5 µg/ml 2 DIV post treatment). Scale bar = 100 µm.

A single 3D spheroid can consist of tens of thousands to hundreds of thousands of cells and can be up to a millimeter in diameter, which is big enough to see with naked eye, without help of microscopy. The traditional 2D model required much less material compared to the 3D model because the surface area is larger and the smaller cell population smaller. In contrast, 3D spheroids generally require more material (higher concentrations) due to larger number of cells and the need for materials to diffuse through multiple layers of cells (proliferating, quiescent, necrotic) [86], [87].

A time series that shows the formation of glioma cells into 3D spheroids in less than 24h is shown in **Figure 3.20.** **Figure 3.21** shows the gradual shape change of the 3D spheroid over a span of 15 days (2 days interval).

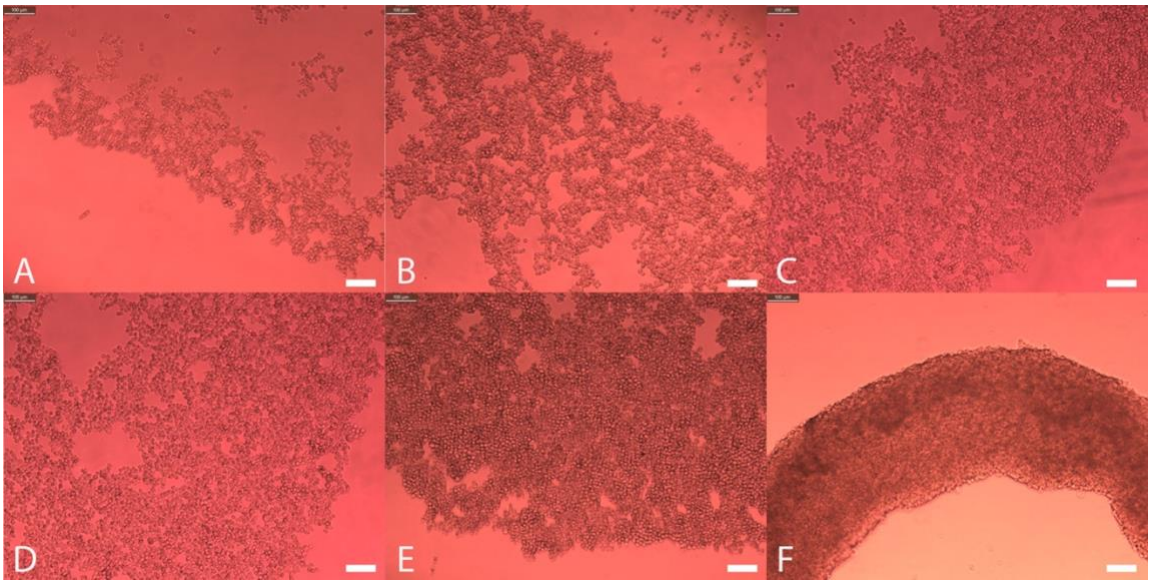

Figure 3.20: Time series of CRL-2303 spheroid (200,000 cells per ml) forming using Nanogaia #SSD-01 kit at 1h (panel A), 2h (panel B), 3h (panel C), 4h (panel D), 6h (panel E), 24h (panel F). Scale bar = 100 µm.

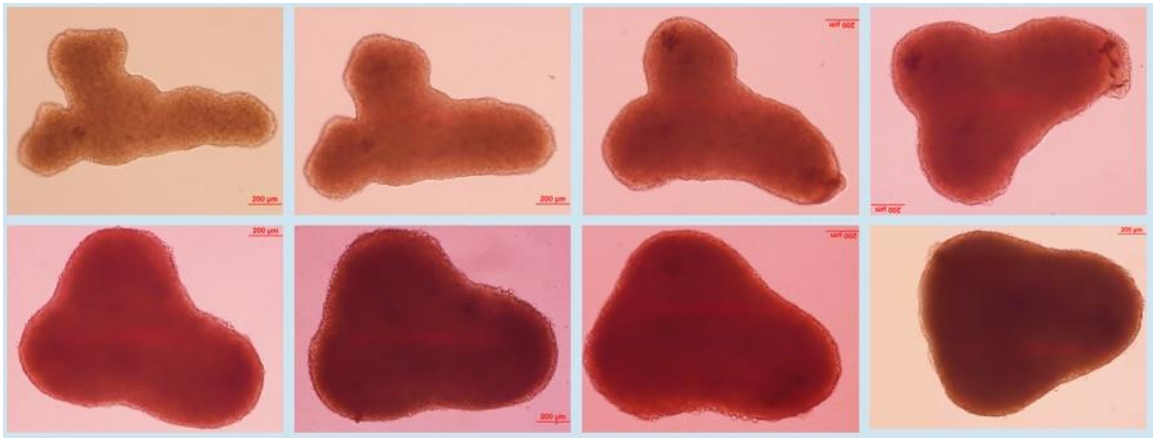

Figure 3.21: Time series of CRL-2303 spheroid growth (200,000 cells per ml) over 15 days (7 div – 21 div). Scale bar = 200 µm.

3.3.2.2 *Interaction with CuHARS*

Figures 3.22 and **3.23** show the interaction of a 3D spheroid of primary astrocytes with different concentrations of CuHARS over time. Phase microscopy was used to record the cells, while bright field microscopy was used to capture the CuHARS with better contrast. The CuHARS started to bind to the outer layer of the astrocyte spheroid

as early as 4h post addition. At low concentration (5 µg/ml), most of the CuHARS bound to the spheroid or were broken down (**Figure 3.22** panel D, E, F) as there was no free CuHARS in the media after 6 days.

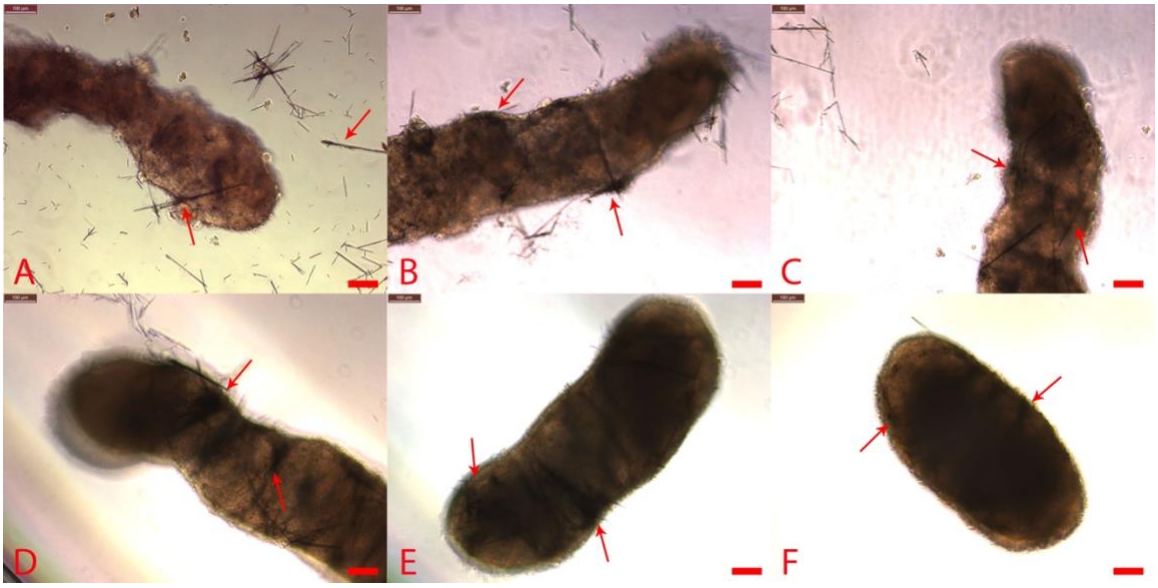

Figure 3.22: Interaction of CuHARS (5 µg/ml) with the astrocyte spheroids. CuHARS were added 5 days after the spheroids were formed. Pictures were taken at 4h (panel A), 1 DIV (panel B), 2 DIV (panel C), 4 DIV (panel D), 6 DIV (panel E) and 10 DIV (panel F) post addition of CuHARS using bright field microscopy at 100x magnification. Red arrows indicate association of CuHARS with cell spheroid. Note breakdown/clearance of CuHARS from the media over time. Scale bar = 100 µm.

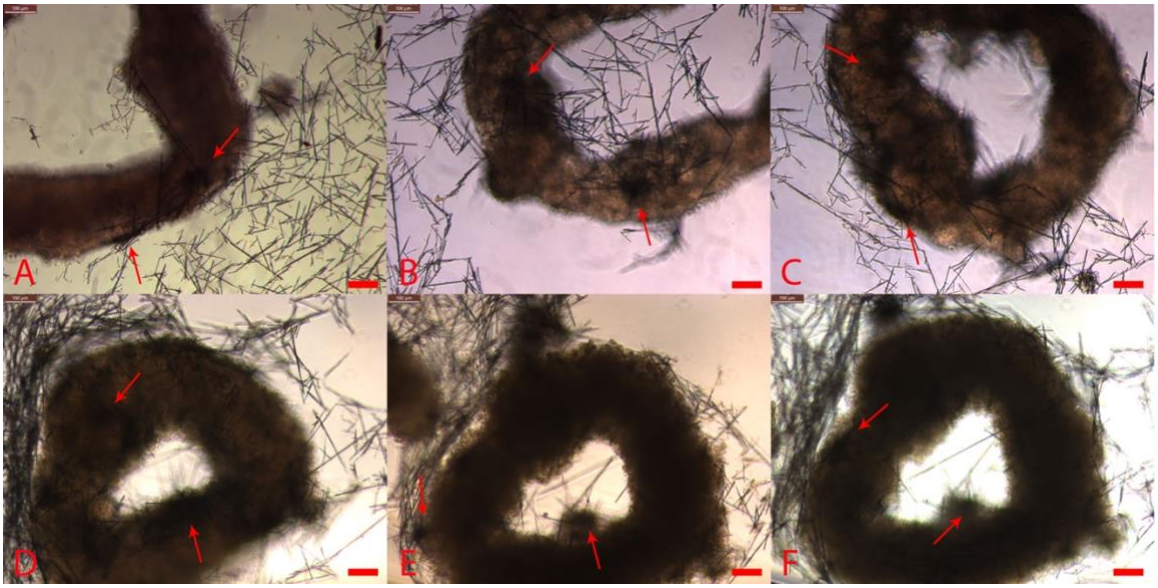

Figure 3.23: Interaction of CuHARS (25 µg/ml) with the astrocyte spheroids. CuHARS were added 5 days after the spheroids were formed. Pictures were taken at 4h (panel A), 1 DIV (panel B), 2 DIV (panel C), 4 DIV (panel D), 6 DIV (panel E) and 10 DIV (panel F) post addition of CuHARS using bright field microscopy at 100x magnification. Red arrows indicate association of CuHARS with cell spheroid. Scale bar = 100 µm.

The same experiment was also carried out with glioma cells. **Figures 3.24** and **3.25** show the interaction of glioma cells with different concentrations of CuHARS over time. Similar to the primary astrocytes, CuHARS clearance occurs at low concentration (5 µg/ml) as most of the CuHARS bound to or near the spheroid were broken down (**Figure 3.24** panel D, E, F) and no free CuHARS were present in the media after 6 days. A low concentration of CuHARS appeared to be initially less toxic to the 3D glioma spheroid, as indicated by the media color change from red to yellow at 4 and 6 DIV, a sign of normal cell metabolism, while high concentration (25 µg/ml) of CuHARS showed indication of toxicity as the color of the media did not change over the course of the experiment. Moreover, both low and high concentration of CuHARS appeared to be toxic to the spheroid at 10 DIV timepoint.

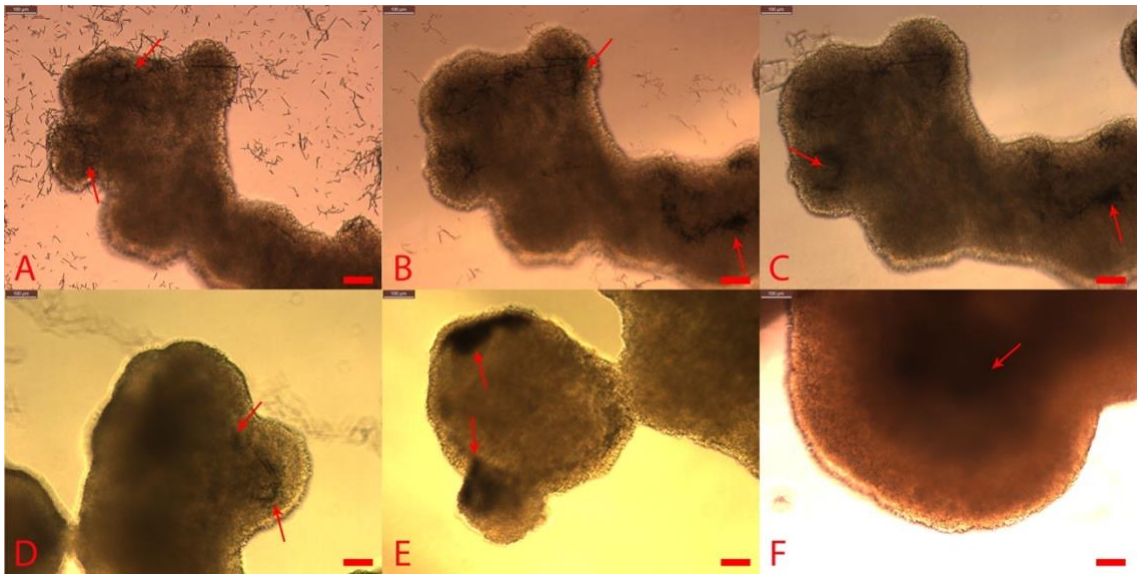

Figure 3.24: Interaction of CuHARS (5 µg/ml) with the brain tumor spheroids. CuHARS were added 5 days after the spheroids were formed. Pictures were taken at 4h (panel A), 1 DIV (panel B), 2 DIV (panel C), 4 DIV (panel D), 6 DIV (panel E) and 10 DIV (panel F) post addition of CuHARS using bright field microscopy at 100x magnification. Red arrows indicate association of CuHARS with cell spheroid. Note breakdown/clearance of CuHARS from the media over time. Scale bar = 100 µm.

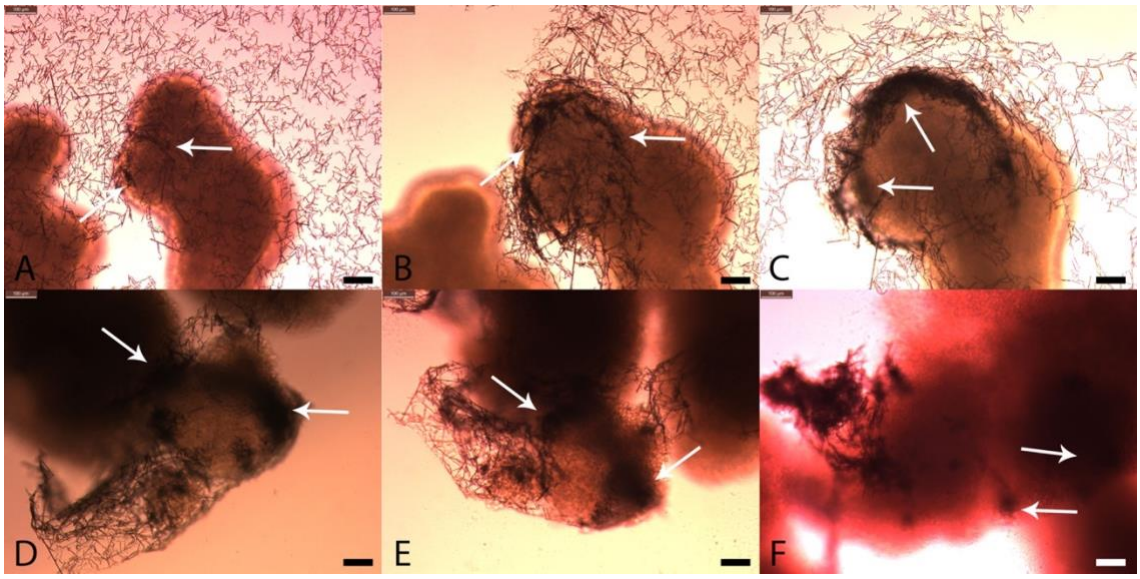

Figure 3.25: Interaction of CuHARS (25 µg/ml) with the brain tumor spheroids. CuHARS were added 5 days after the spheroids were formed. Pictures were taken at 4h (panel A), 1 DIV (panel B), 2 DIV (panel C), 4 DIV (panel D), 6 DIV (panel E) and 10 DIV (panel F) post addition of CuHARS using bright field microscopy at 100x magnification. White arrows indicate association of CuHARS with cell spheroid. Note breakdown/clearance of CuHARS over time. Scale bar = 100 µm.

3.3.2.3 *Interaction with CuNPs*

Figure 3.26 and **3.27** show the interaction of primary astrocytes spheroid with different concentrations of CuNPs over time. Phase microscopy was used to record the cells, while bright field microscopy was used to capture the CuNPs with better contrast. CuNPs at low concentration of 2.5 µg/ml degraded completely within 5h of treatment, while at a higher concentration of 12.5 µg/ml were still present after 5h of treatment but were broken down completely within 24h of treatment. A high concentration (12.5 µg/ml) of CuNPs appeared to be toxic to the spheroid at the 4, 6 and 10 DIV timepoints, as indicated by the large amount of cell debris presented around the spheroid and the rough edge of the spheroid itself (**Figure 3.27** panel D, E, F), compared to little cell debris and the smooth edge of the spheroid (**Figure 3.26** panel D, E, F). The cell debris and rough edge are present because most of the CuNPs came into contact with cells from the proliferating layer (the outer layer) of the spheroid, causing those cells to become stressed and undergo apoptosis/necrosis.

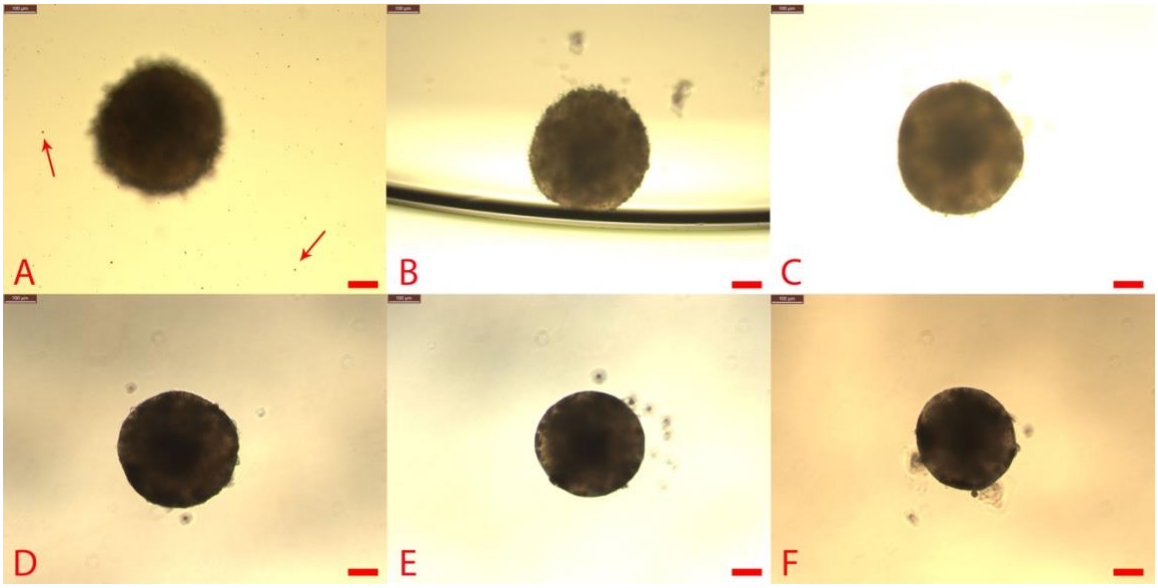

Figure 3.26: Interaction of CuNPs (2.5 µg/ml) with the astrocyte spheroids. CuNPs were added 5 days after the spheroids were formed. Pictures were taken at 0h (panel A), 5h (panel B), 1 DIV (panel C), 4 DIV (panel D), 6 DIV (panel E) and 10 DIV (panel F) post addition of CuNPs using bright field microscopy at 100x magnification. Red arrows indicate CuNPs in media. Scale bar = 100 µm.

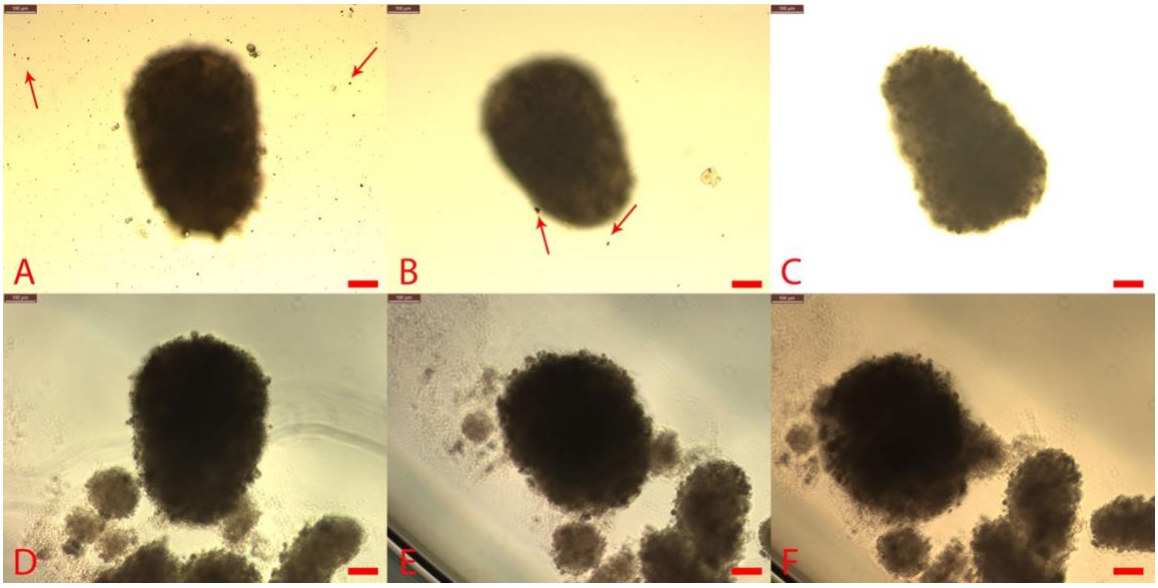

Figure 3.27: Interaction of CuNPs (12.5 µg/ml) with the astrocyte spheroids. CuNPs were added 5 days after the spheroids were formed. Pictures were taken at 0h (panel A), 5h (panel B), 1 DIV (panel C), 4 DIV (panel D), 6 DIV (panel E) and 10 DIV (panel F) post addition of CuNPs using bright field microscopy at 100x magnification. Red arrows indicate CuNPs in media. Scale bar = 100 µm.

The same experiment was also carried out with glioma cells. **Figure 3.28** and **3.29** show the interaction of glioma cells with different concentrations of CuNPs over time. Both low and high concentrations (2.5 µg/ml and 12.5 µg/ml) of CuNPs broke down rapidly, with complete break down in 5h for the low concentration (2.5 µg/ml) and 24h for all concentrations similar to the case with primary astrocytes. At both concentrations of CuNPs, media color changed to yellow toward the end of the experiment, indicating that brain tumor cells survived and recovered (cell metabolism went up) even at high concentration of CuNPs.

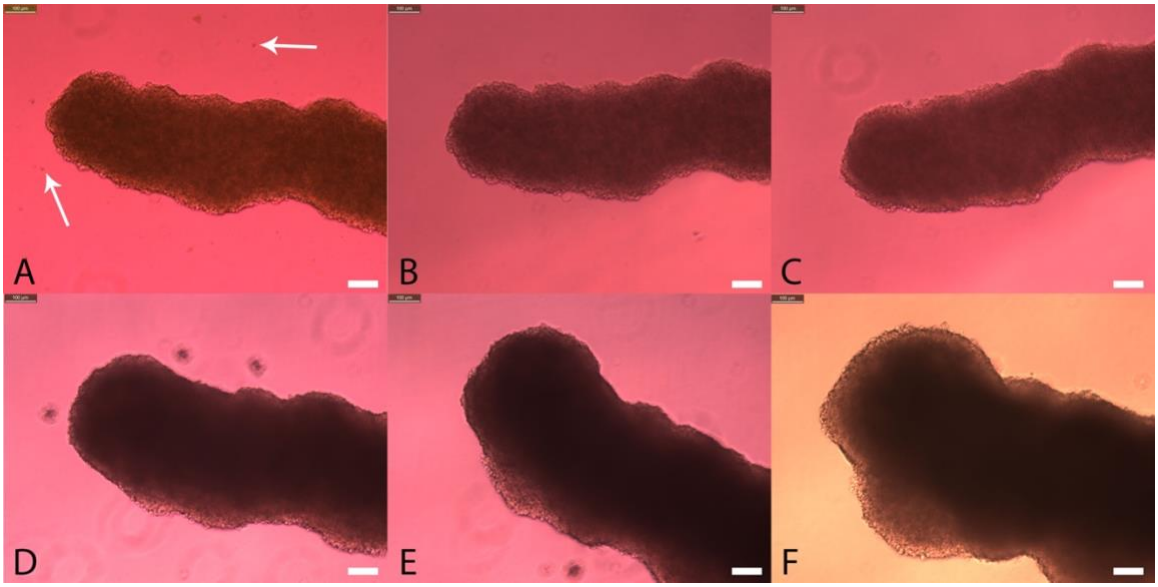

Figure 3.28: Interaction of CuNPs (2.5 µg/ml) with the brain tumor spheroids. CuNPs were added 5 days after the spheroids were formed. Pictures were taken at 0h (panel A), 5h (panel B), 1 DIV (panel C), 4 DIV (panel D), 6 DIV (panel E) and 10 DIV (panel F) post addition of CuNPs using bright field microscopy at 100x magnification. White arrows indicate CuNPs in media. Scale bar = 100 µm.

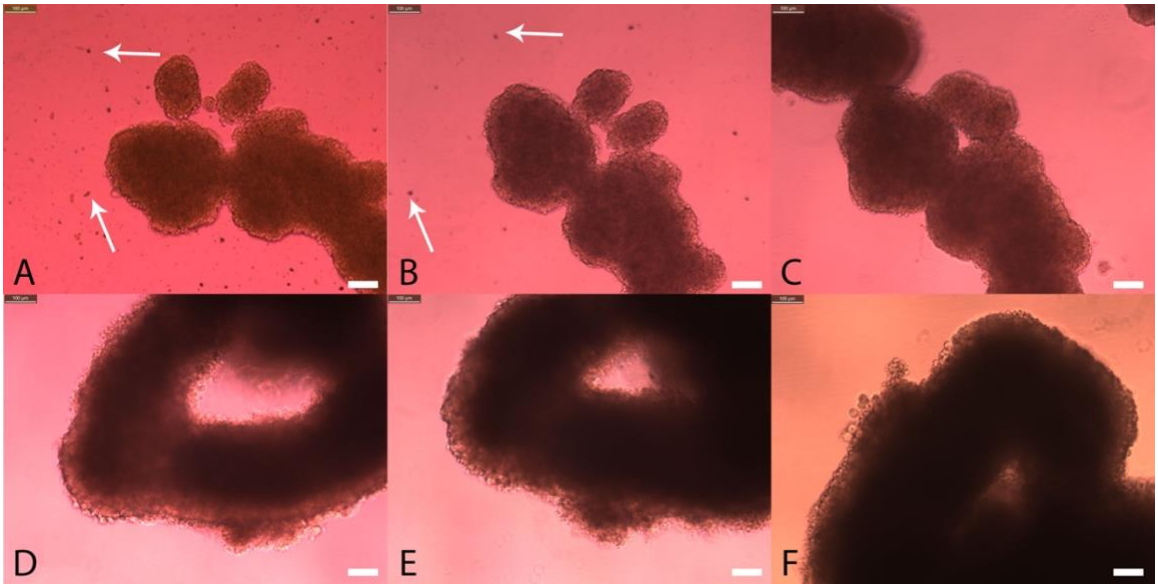

Figure 3.29: Interaction of CuNPs (12.5 µg/ml) with the brain tumor spheroids. CuNPs were added 5 days after the spheroids were formed. Pictures were taken at 0h (panel A), 5h (panel B), 1 DIV (panel C), 4 DIV (panel D), 6 DIV (panel E) and 10 DIV (panel F) post addition of CuNPs using bright field microscopy at 100x magnification. White arrows indicate CuNPs in media. Scale bar = 100 µm.

3.3.2.4 *Interaction with HNTs*

Figure 3. 30 and **3.31** show the interaction of primary astrocytes spheroid with different concentrations of HNTs over time. Phase microscopy was used to record the cells, while fluorescent microscopy was used to capture the HNTs then both pictures of the same area were combined into one panel. As with the 2D cell culture model, the fluorescent HNTs quickly started to attach to the astrocyte spheroid and the amount of HNTs bound to the spheroid kept increasing over time as indicated by the area of the spheroid cover by the fluorescent HNTs grew while the amount of HNTs in the media decreased.

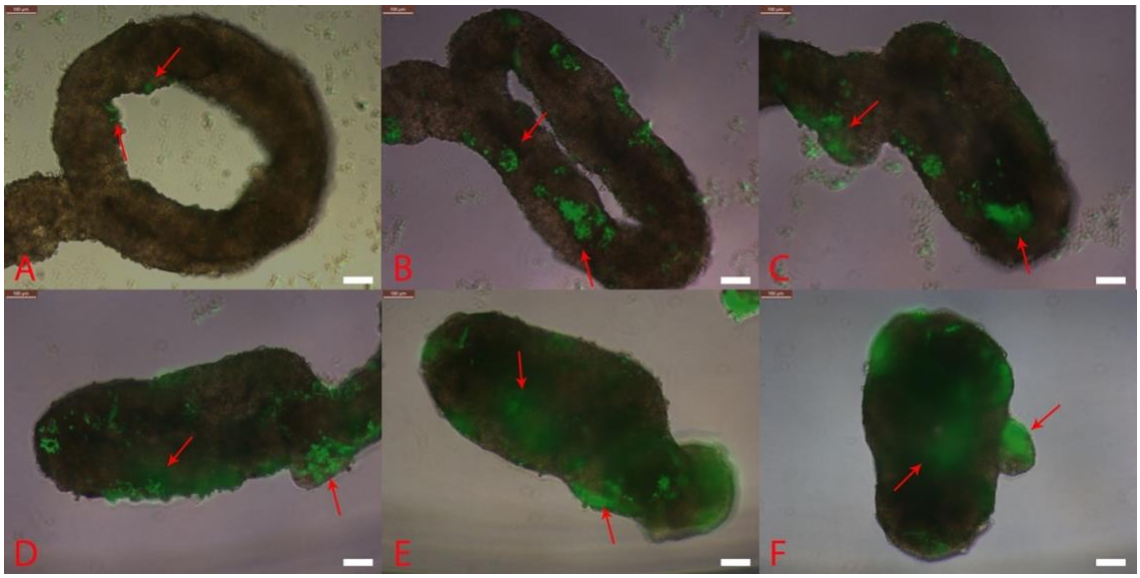

Figure 3.30: Interaction of fluorescent HNTs (5 µg/ml) with the astrocyte spheroids. HNTs were added 5 days after the spheroids were formed. Pictures were taken at 4h (panel A), 1 DIV (panel B), 2 DIV (panel C), 4 DIV (panel D), 6 DIV (panel E) and 10 DIV (panel F) post addition of HNTs using bright field microscopy at 100x magnification. Red arrows indicate association of HNTs with cell spheroid. Scale bar = 100 µm.

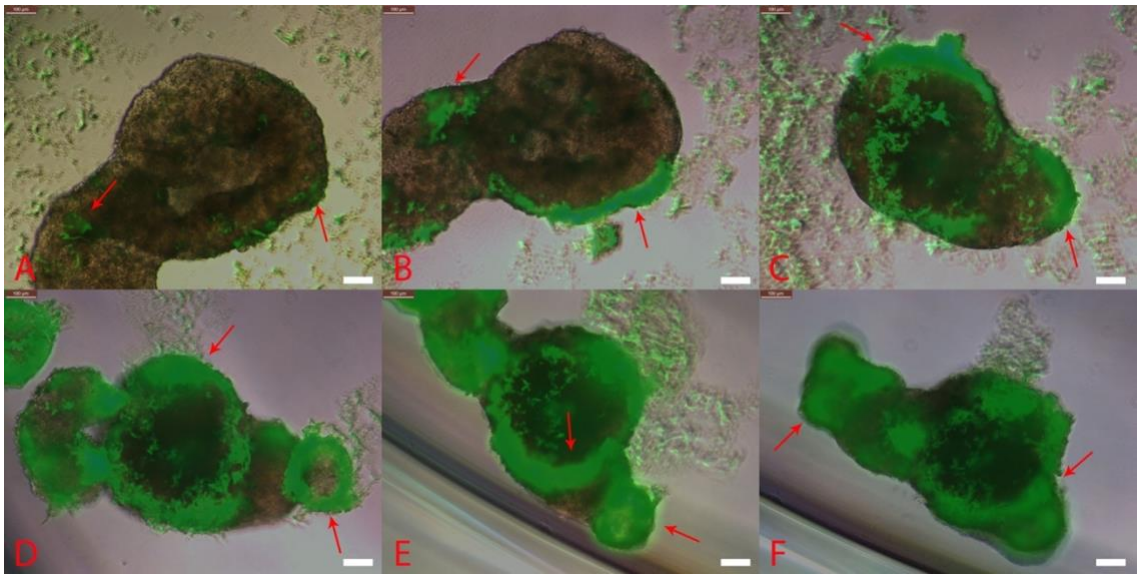

Figure 3.31: Interaction of fluorescent HNTs (25 µg/ml) with the astrocyte spheroids. HNTs were added 5 days after the spheroids were formed. Pictures were taken at 4h (panel A), 1 DIV (panel B), 2 DIV (panel C), 4 DIV (panel D), 6 DIV (panel E) and 10 DIV (panel F) post addition of HNTs using bright field microscopy at 100x magnification. Red arrows indicate association of HNTs with cell spheroid. Scale bar = 100 µm.

The same experiment was also carried out with glioma cells and fluorescent HNTs. **Figure 3.32** and **3.33** shows the interaction of glioma cells with different concentrations of HNTs over time. As with the case of astrocytes, phase microscopy was used to record the cells, while fluorescent microscopy was used to capture the HNTs. Both pictures of the same area were then combined into one panel. As in the primary astrocyte model (**Figure 3.30** and **Figure 3.31**) the fluorescent HNTs quickly started to attach to the glioma spheroid, and the amount of HNTs bound to the spheroid kept increasing over time (**Figure 3.32** and **Figure 3.33** panel E, F). Note the different z-plane focus due to the three-dimensional feature of the spheroid compared to the relatively flat two-dimensional cell culture.

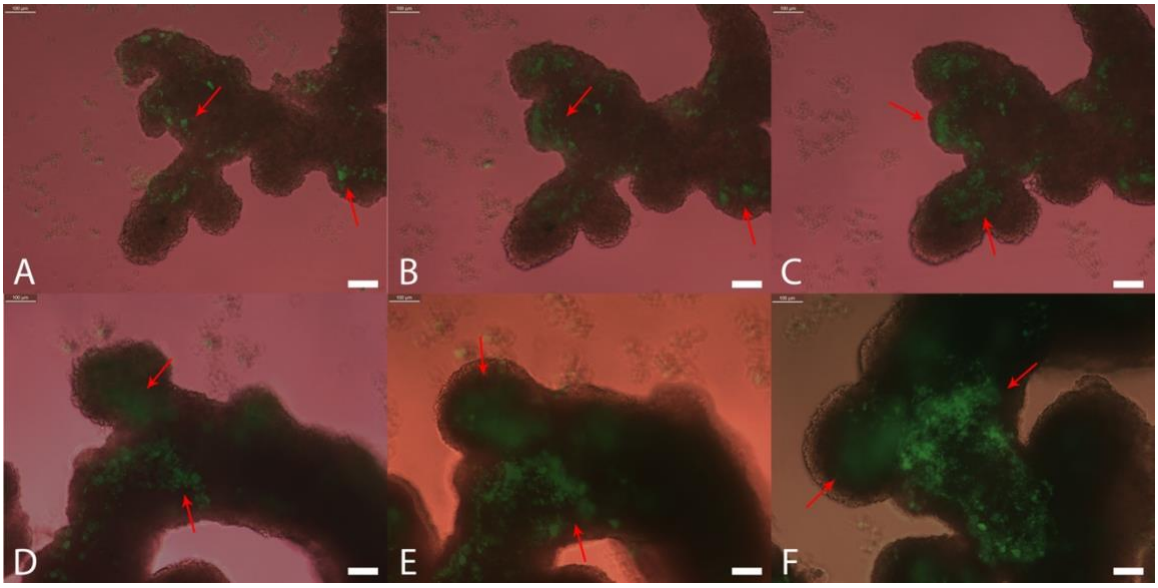

Figure 3.32: Interaction of fluorescent HNTs (5 µg/ml) with the brain tumor spheroids. HNTs were added 5 days after the spheroids were formed. Pictures were taken at 4h (panel A), 1 DIV (panel B), 2 DIV (panel C), 4 DIV (panel D), 6 DIV (panel E) and 10 DIV (panel F) post addition of HNTs using bright field microscopy at 100x magnification. Red arrows indicate association of HNTs with cell spheroid. Scale bar = 100 µm.

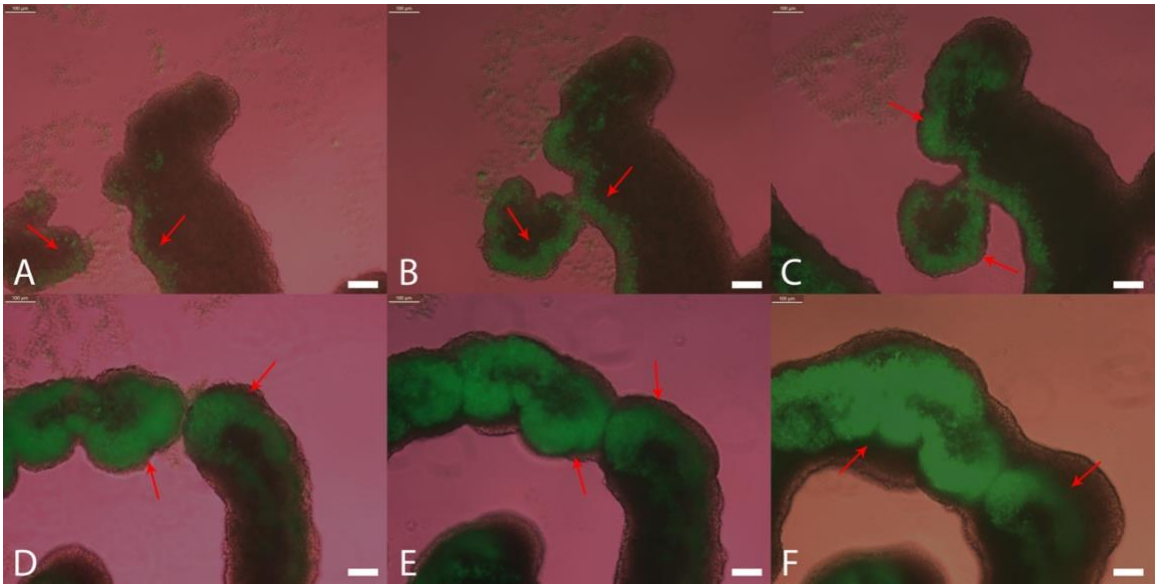

Figure 3.33: Interaction of fluorescent HNTs (25 µg/ml) with the brain tumor spheroids. HNTs were added 5 days after the spheroids were formed. Pictures were taken at 4h (panel A), 1 DIV (panel B), 2 DIV (panel C), 4 DIV (panel D), 6 DIV (panel E) and 10 DIV (panel F) post addition of HNTs using bright field microscopy at 100x magnification. Red arrows indicate association of HNTs with cell spheroid. Scale bar = 100 µm.

A summary of the effects each material had on each cell type are shown in **Table 3.1**-**3.6**.

Table 3.1: Effects of CuHARS on primary astrocytes with ~ for no effect, - for small effect, and -/- for larger effect. The first three time points applied for both 2D and 3D models while the last two time points only applied for 3D model.

Time point / **Concentration**	0 div	1 div	4 div	6div (3D)	10 div (3D)
Low	~	~	~	~	~
Medium	~	~	-	-	-/-
High	~	~	-	-	-/-

Table 3.2: Effects of CuHARS on brain tumor cells with ~ for no effect, - for small effect, and -/- for larger effect. The first three time points applied for both 2D and 3D models while the last two time points only applied for 3D model.

Time point / Concentration	0 div	1 div	4 div	6div (3D)	10 div (3D)
Low	~	~	~	~	~
Medium	~	~	~	~	-
High	~	~	-	-	-/-

Table 3.3: Effects of CuNPs on primary astrocytes with ~ for no effect, - for small effect, -/- for larger effect, and -/-/- for cell death. The first three time points applied for both 2D and 3D models while the last two time points only applied for 3D model.

Time point / Concentration	0 div	1 div	4 div	6div (3D)	10 div (3D)
Low	~	-	-	-/-	-/-
Medium	~	-	-/-	-/-	-/-
High	~	-/-	-/-/-	-/-/-	-/-/-

Table 3.4: Effects of CuNPs on brain tumor cells with ~ for no effect, - for small effect, -/- for larger effect, and -/-/- for cell death. The first three time points applied for both 2D and 3D models while the last two time points only applied for 3D model.

Time point / Concentration	0 div	1 div	4 div	6div (3D)	10 div (3D)
Low	~	-	-	-/-	-/-
Medium	~	-	-/-	-/-	-/-
High	~	-/-	-/-/-	-/-/-	-/-

Table 3.5: Effects of HNTs on primary astrocytes with ~ for no effect, - for small effect, and -/- for larger effect. The first three time points applied for both 2D and 3D models while the last two time points only applied for 3D model.

Time point / Concentration	0 div	1 div	4 div	6div (3D)	10 div (3D)
Low	~	~	-	-	-
Medium	~	-	-	-	-
High	~	-	-/-	-/-	-/-

Table 3.6: Effects of HNTs on brain tumor cells with ~ for no effect, - for small effect, and -/- for larger effect. The first three time points applied for both 2D and 3D models while the last two time points only applied for 3D model.

Time point / Concentration	0 div	1 div	4 div	6div (3D)	10 div (3D)
Low	~	~	~	~	~
Medium	~	~	~	~	~
High	~	~	~	~	~

3.4 Discussion

Since cells in 2D model grow into a monolayer, changes in cell morphology (shape, viability) after interaction with materials happen quicker and can be easily measured and quantified. The number of cells and amount of materials required in 2D model are also lower compared to 3D model. However, cells in 2D model less accurately mimic cell characteristics exhibited in *in vivo* model, which could lead to incorrect response in drug/materials interactions. Moreover, overaggressive cell types (e.g. glioma) limit the duration of observation in the 2D model (cell culture becomes confluent over a short period of time – **Figure 3.6**). In contrast, the 3D cell model requires more cells, more materials, and more time to grow, but the cells are a more accurate model of cell-

cell and cell-matrix interaction than the 2D *in vivo* model. Response to drug/material treatment will be closer to *in vivo* model due to the presence of diffusion barriers (multiple cell layers – proliferating, quiescent, necrotic). Cells grow in suspension in 3D model also enable longer term experiment (more than 10 DIV).

Of all three materials tested, CuNPs appeared to be the most toxic to the cells, especially to primary astrocytes (**Figure 3.9** and **Figure 3.27**) while CuHARS with the same amount of copper showed little to no sign of stress on both primary astrocytes and gliomas (**Figure 3.3, 3.6, 3,22** and **3.24**). Further detailed and quantitative analysis of toxicity of these materials on both 2D and 3D models will be presented in **Chapter 4**.

CHAPTER 4

THE USE OF CUHARS AS DELIVERY SYSTEM IN TWO- AND THREE-DIMENSIONAL CELL MODELS

4.1 Overview

CuHARS can be coated with a cancer drug, as a drug delivery system, and it can be coated with growth factors to promote cell growth. In this study, CuHARS were delivered to both 2D and 3D spheroid models in different concentrations to study the effects of the biomaterial to cells (normal and cancer brain cell) over short and long-term periods. The results of different bio-physical features will be compared with two other materials CuNPs and HNTs as shown in **Figure 4.1**.

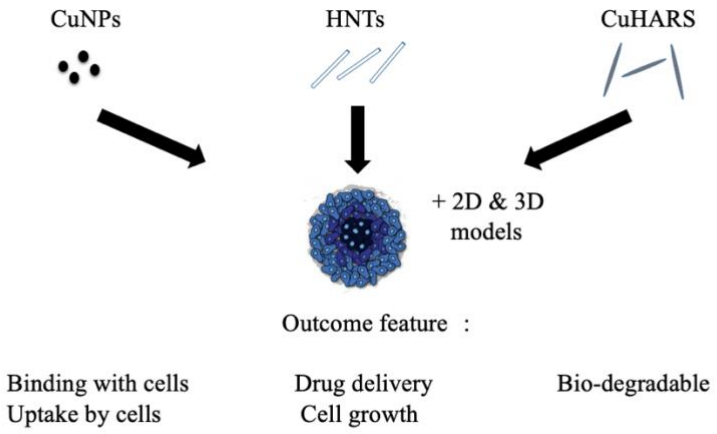

Figure 4.1: Schematic diagram of interaction of brain cells with non-degradable and degradable materials [9] and their outcome features.

We will also study the effect of anti-cancer drugs (cisplatin, paclitaxel and disulfiram) as the positive control in 2D and 3D cell models over short and long-term periods.

Interaction of the 3D spheroids with the three materials (CuNPs, CuHARS and HNTs) over time is diagrammed in **Figure 4.2**. As demonstrated in **Chapter 3**, of three materials, CuNPs break down the most rapidly and cause most toxicity to the cell initially, but the cells recover over time (especially in case of glioma). HNTs do not break down and are taken up/bound by the cells over time. Meanwhile, CuHARS bind to the cells and break down over time, causing delayed toxicity to the cells.

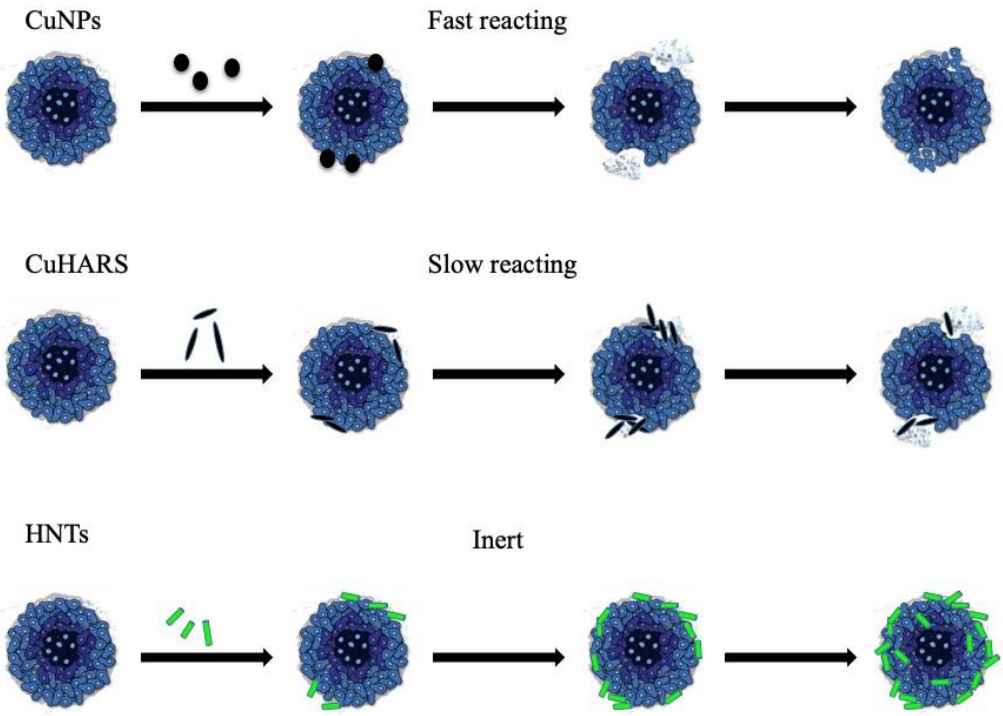

Figure 4.2: Schematic diagram of 3D spheroid of brain cells after interaction with non-degradable and degradable materials over time (adapted from [88]).

4.2 Materials and Methods

4.2.1 Cell Types

Rat brain glioma cells (CRL-2303) are obtained from American Type Culture Collection (ATCC) and cultured in DMEM containing 10% FBS, 1% non-essential amino acid solution, and 0.5% penicillin/streptomycin (**Appendix A, Section A.1)**.

Rat brain astrocytes are harvested from the cortex of newborn rats and cultured in astrocyte medium (Ham's F-12K) containing 10% Horse serum and other components (**Appendix A, Section A.2)**.

4.2.2 Method

To test the effects of biomaterials in both 2D and 3D models, cells were grown as specified in **Chapter 3**. Materials were added at day 3 in 2D model and day 7 in 3D model at different concentrations.

After 3 days, MTT assay and DAPI staining were performed to study cell viability in 2D model (n =9). For 3D model, microscopic images were recorded using Leica DMI600B microscopy every two days and the area of the spheroid was measured using Image Pro Plus 7.0 and Matlab 2015b software. Cell viability was measured using a resazurin assay with a fluorescent plate reader, at 3,5,7 and 9 DIV, post-treatment (n=4).

Cancer drugs (cisplatin, paclitaxel, and disulfiram) were added to both models at different concentrations to study their effects over short and long-term periods. Disulfiram (DSF), an FDA approved drug for alcoholism treatment, has recently been studied as a promising drug to treat cancers, including glioblastoma. Moreover, data have shown that the effects of DSF is maximized in the presence of copper. Therefore, using a

combination of DSF and CuHARS could be a novel approach to treat glioblastoma [15], [17].

4.2.2.1 *Cisplatin*

Cisplatin, a mutagenic and carcinogenic agent [89] that belongs to a class of platinum-containing anticancer drugs [90] is used to treat sarcomas, carcinomas, lymphomas, testicular cancer, ovarian cancer, cervical cancer, breast cancer, brain tumors and neuroblastoma. Cisplatin works by interfering with DNA replication, which means it can effectively kill the fastest proliferating cells, i.e. the cancerous cells. It has been reported to give enhanced effect for treating glioblastoma by combining with temozolomide [91] or conjugated gold nanoparticle [92].

4.2.2.2 *Paclitaxel*

Paclitaxel is a plant alkaloid that was first isolated from the bark of the Pacific yew tree Taxus brevifolia in 1971. It is synthesized in the bark of the tree by endophytic fungi. Paclitaxel is a cytoskeletal drug type that binds to tubulin and prevents the disassembly of microtubules, subsequently inhibits cell division. It can also induce apoptosis by binding to and blocking the function of the apoptosis inhibitor protein Bcl-2 (B-cell Leukemia 2). Paclitaxel is often used in the treatment of lung, ovarian, breast cancer, and pancreatic cancer. A combination of paclitaxel and temozolomide has been reported to enhance efficacy in treating malignant glioma [93].

4.2.3 MTT Cell Viability Assay

MTT (3-(4,5-dimethylthiazol-2-yl)-2,5-diphenyl tetrazolium bromide) obtained from Thermo Fisher Scientific (Waltham, MA) was dissolved in 1x DMEM at a concentration of 1.25 mg/mL. The MTT solution of 400 μL was added to each well and

incubated for one hour. After one hour, each well was washed and 200 μL of 91% isopropanol was added and mixed thoroughly (**Appendix F)**. The mix solution was then added to a 96 well-plate for spectroscopy. Thermo Scientific Multiskan Spectrum plate reader analyzed the wells at a wavelength of 570 nm. Figure 3-4 shows MTT reacting to formazan crystals through mitochondrial reductase.

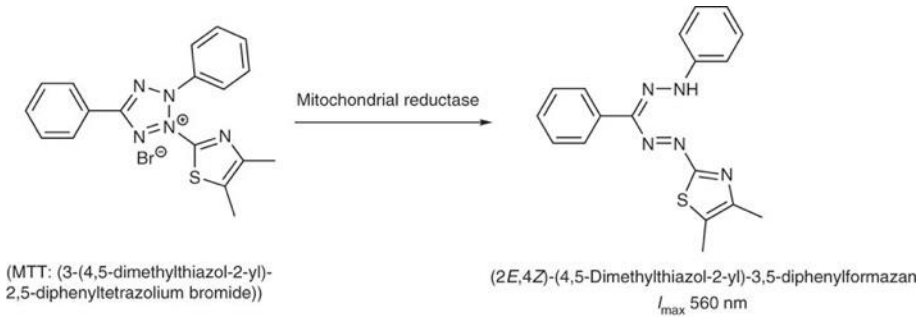

Figure 4.3: MTT to formazan crystals in the mitochondria [94].

4.2.4 Resazurin Assay

Resazurin (7-Hydroxy-3H-phenoxazin-3-one-10-oxide sodium salt) is a dye commonly used in cell viability assay [95], [96]. Resazurin by itself is weakly fluorescent but is effectively reduced in mitochondria when introduced to cell culture, resulting in a strong fluorescent derivative resorufin (**Figure 4.4**). Resazurin purchased from Sigma (#R7017) was diluted in PBS 1x at 0.2mg/ml concentration (**Appendix I)**. Each spheroid was moved from original plate to a 96 well-plate with 150 μl media and add 50 μl of resazurin solution. The plate was incubated for at least four hours and then analyzed with a fluorescence reader Gen5 Biotek Fluorescence Plate Reader at 550 nm, 585 nm wavelengths of excitation and emission, respectively.

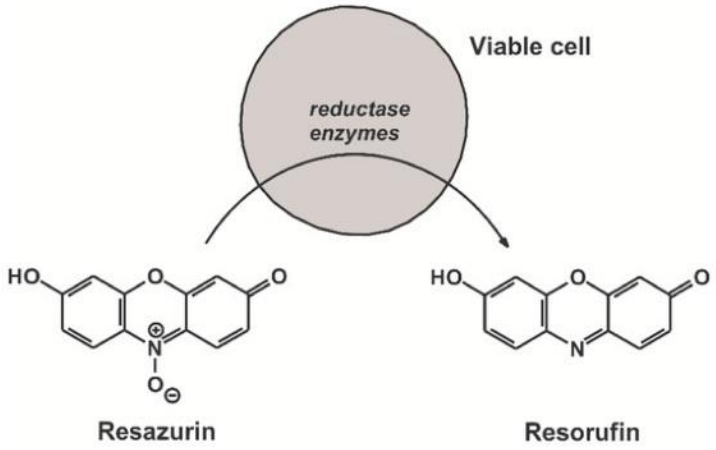

Figure 4.4: Viable cells reduce resazurin to its derivative, highly fluorescent metabolic resorufin [95].

4.2.5 Image Analysis

Image Analysis was carried out using software Image Pro-Plus version 7.0 developed by Media Cybernetics (Rockville, MD) to measure total area of each material. For images stained with DAPI, the total number of nuclei (objects) and total area of nuclei were calculated.

4.2.6 Statistics

Data analysis on total area of images cover by each material and cell viability of both cell types treated with each material was performed in R software and the significance of the test results was analyzed using one-way ANOVA test for normally distributed data and Kruskal-Wallis test for non-normally distributed data. The null hypotheses were that total area of materials did not change over time and cell viability showed no difference between treatment groups. A p-value less than 0.05 was considered statistically significant.

4.3 Results

4.3.1 Cell Viability in 2D Model

4.3.1.1 *Interaction with CuNPs*

CuNPs were captured using bright field microscopy and analyzed using Image Pro Plus 7.0 software to measure total area. **Figure 4.5** shows clearance of CuNPs in primary astrocyte (top panel) and glioma (bottom panel) culture in less than 24h for all concentrations. As confirmed in **Figure 3.7**, **3.8** (primary astrocyte) and **Figure 3.10**, **3.11** (glioma cells), CuNPs of all concentrations broke down in less than 24h with low concentration breaking down as fast as within 3h.

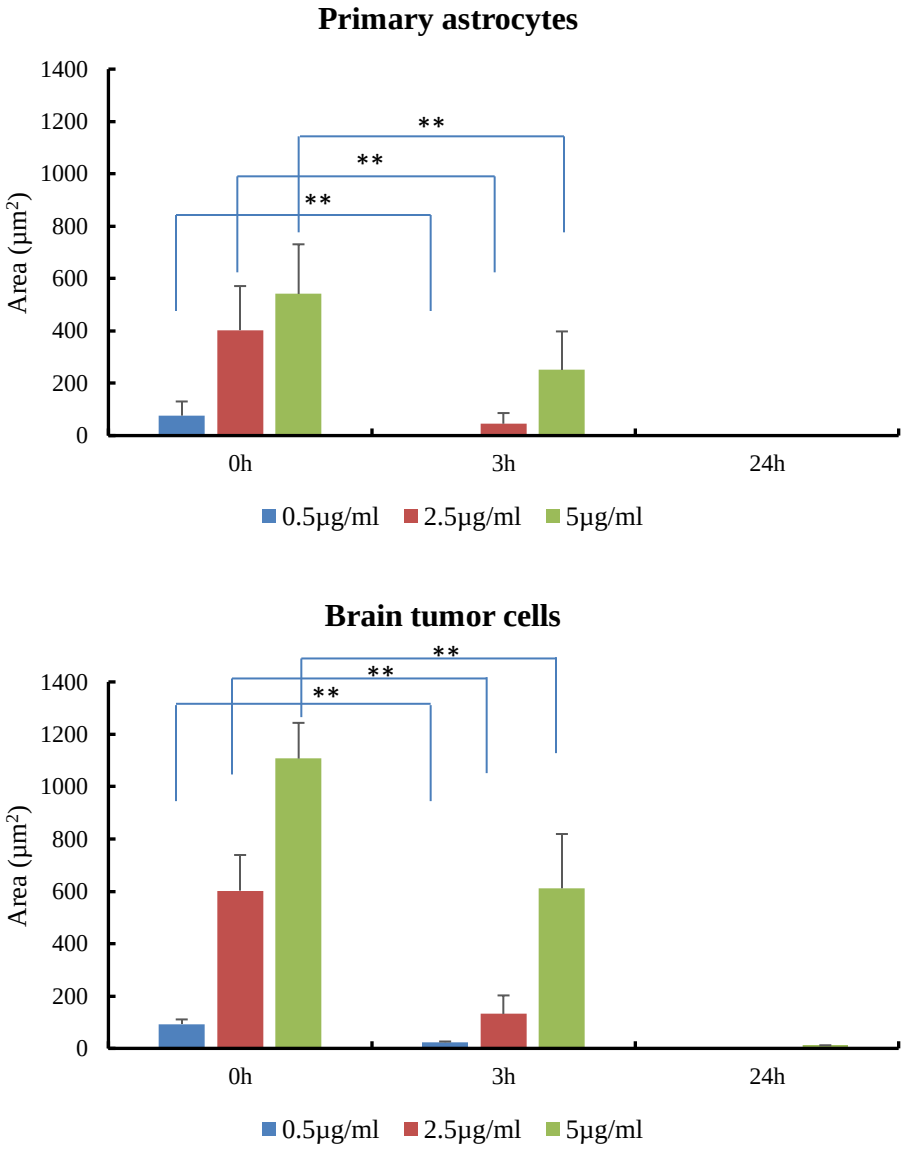

Figure 4.5: Total area of CuNPs (0.5µg/ml, 2.5µg/ml and 5µg/ml) added to astrocytes and brain tumor cells 2D models over time. n =9 per concentration, error bars represent standard deviation. Note the complete breakdown of CuNPs of all concentrations in less than 24h. Clearance was concentration-dependent with significant difference denoted by ** for $p \leq 0.01$. For astrocyte culture, $\chi^2 = 76.166$, df = 8, p-value = 2.88e-13. For glioma culture, $\chi^2 = 77.68$, df = 8, p-value = 1.431e-13.

4.3.1.2 *Interaction with CuHARS*

CuHARS were captured using bright field microscopy and analyzed using Image Pro Plus 7.0 software to measure total area, as shown in **Figure 4.6** and illustrated in

Figure 3.1, **3.2** (primary astrocyte) and **Figure 3.5**, **3.6** (glioma cells), CuHARS were not broken down as fast as CuNPs with more than 60% of CuHARS at all concentrations still present at 96h time point compared to the 0h time point.

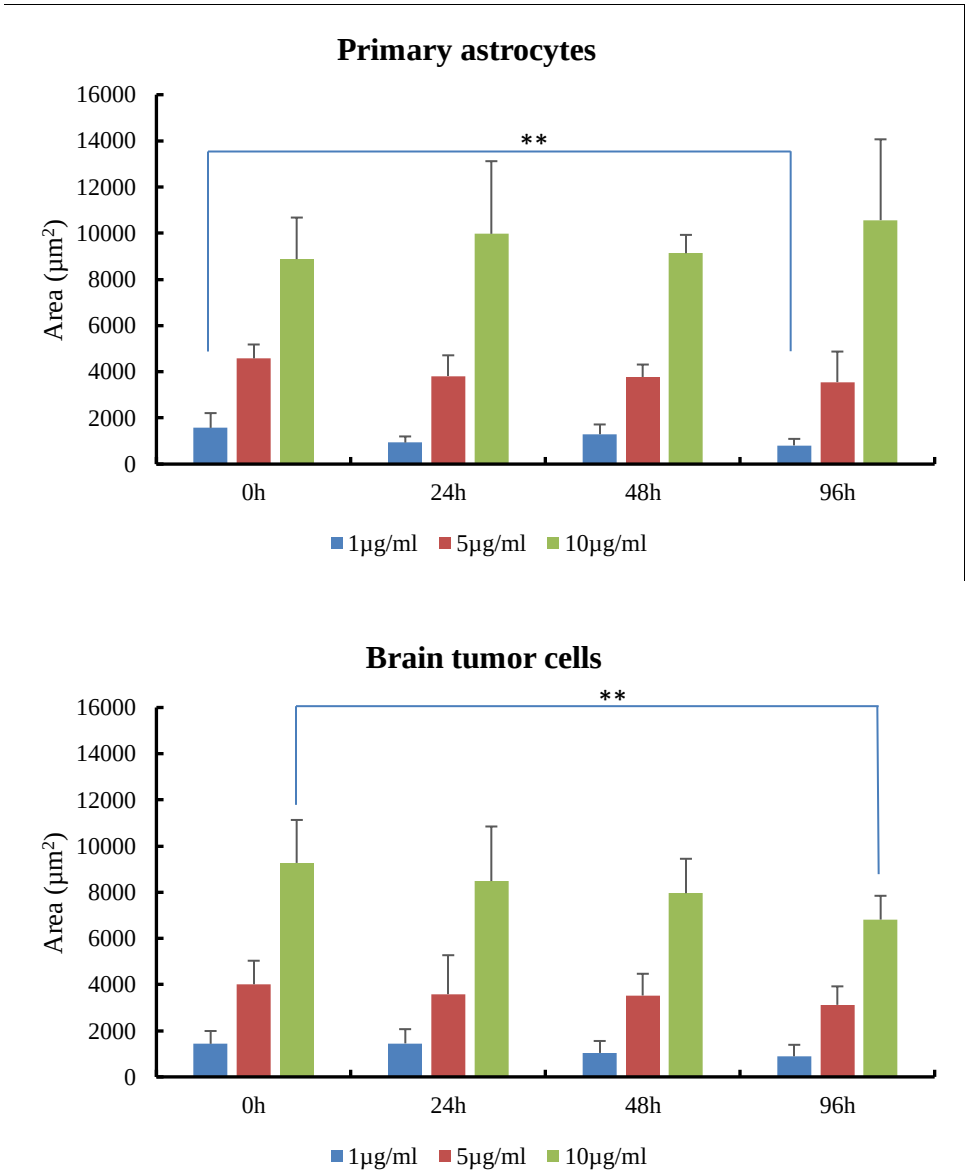

Figure 4.6: Total area of CuHARS (1µg/ml, 5µg/ml and 10µg/ml) added to astrocytes and brain tumor cells 2D models over time. n =9 per concentration, error bars represent standard deviation. Note the slow breakdown of CuHARS of all concentrations over time compared to CuNPs. Clearance was concentration-dependent with significant difference denoted by ** for $p \leq 0.01$. For astrocyte culture, $\chi^2 = 96.903$ with df = 11 and p-value = 7.313e-16. For glioma culture, $\chi^2 = 94.92$, df = 11, p-value = 1.8e-15.

4.3.1.3 *Interaction with HNTs*

Fluorescent HNTs were imaged under fluorescent microscopy, and Image Pro Plus 7.0 software was used to measure total area. **Figure 4.7** shows total area of HNTs in primary astrocyte (top panel) and glioma (bottom panel) culture went down over time for all concentrations because the materials clumped and were taken up/bound by the cells, as illustrated in **Figures 3.13** and **3.14** (primary astrocyte) and **Figures 3.16** and **3.17** (glioma cells).

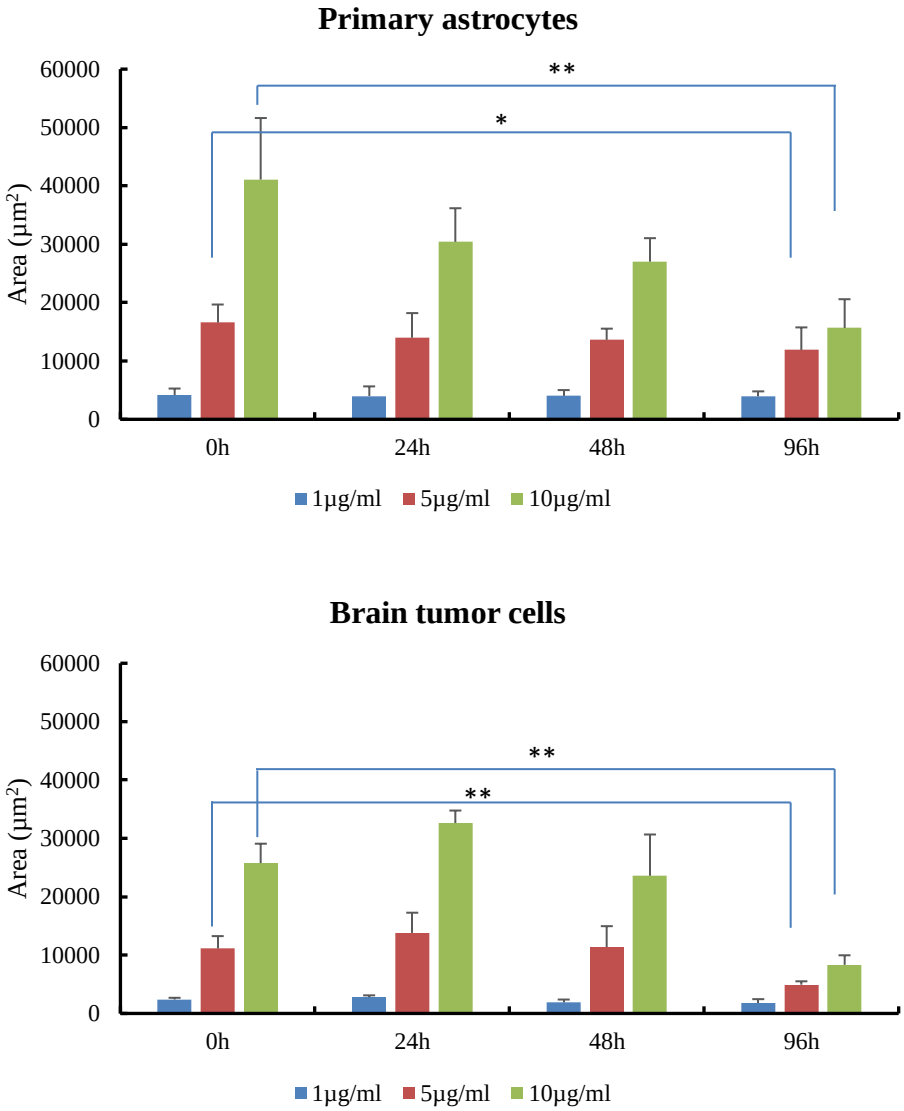

Figure 4.7: Total area of fluorescent HNTs (1µg/ml, 5µg/ml and 10µg/ml) added to astrocytes and brain tumor cells 2D models over time, n =9 per concentration, error bars represent standard deviation. Results were concentration-dependent with significant difference denoted by * for p≤ 0.05, ** for p≤ 0.01. For astrocyte culture, χ^2 = 95.248, df = 11, p-value = 1.551e-15. For glioma culture, χ^2 = 101.01, df = 11, p-value < 2.2e-16.

The total area of three materials (CuHARS, CuNPs and fluorescent HNTs) over time in primary astrocyte and glioma culture are displayed side-by-side in **Figures 4.8** and **4.9**. As previously mentioned, CuHARS showed little break down over 4DIV (96h),

CuNPs completely broken down in 24h and fluorescent HNTs total area went down as HNTs were not broken down but instead taken up/bound by the cells.

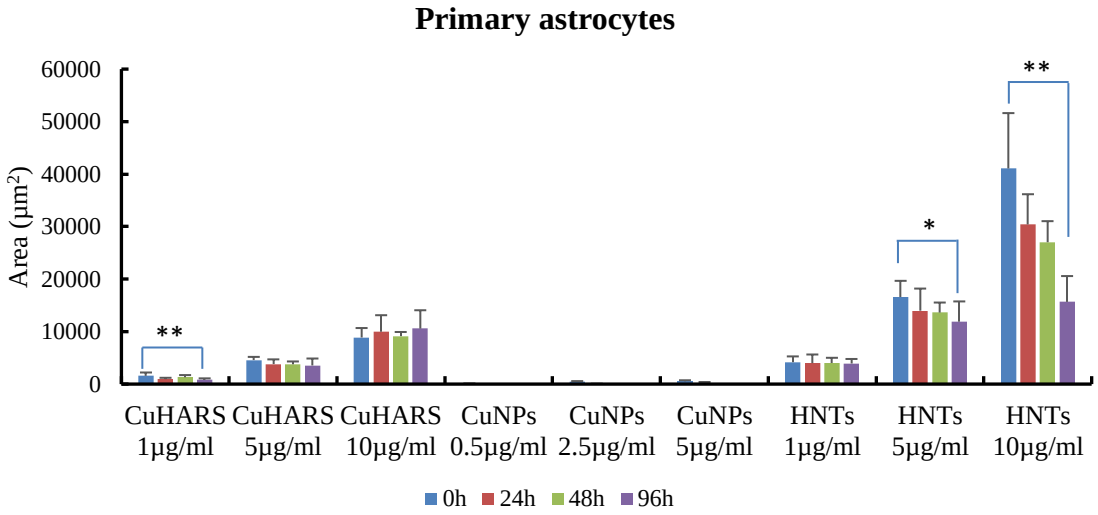

Figure 4.8: Total area of materials (CuHARS, CuNPs and HNTs) added to astrocytes 2D models over time, n =9 per material for each concentration, error bars represent standard deviation. Results were concentration-dependent with significant difference denoted by * for $p \leq 0.05$, ** for $p \leq 0.01$. $\chi^2 = 287.63$, df = 32, p-value < 2.2e-16.

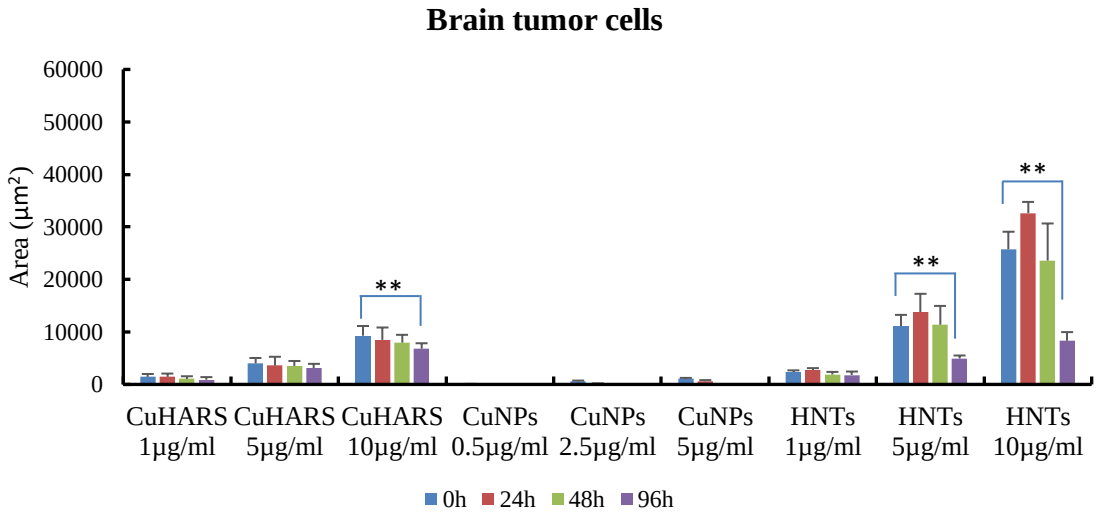

Figure 4.9: Total area of materials (CuHARS, CuNPs and HNTs) added to glioma culture 2D models over time, n =9 per material for each concentration, error bars represent standard deviation. Results were concentration-dependent with significant difference denoted by ** for $p \leq 0.01$. $\chi^2 = 287.51$, df = 32, p-value < 2.2e-16.

4.3.1.4 *Cell Viability*

Viability assay results using MTT to measure cell metabolism after interaction with materials are shown in **Figure 4.10**. Of all three materials, CuNPs were the most toxic to the cells, as reflected by the lowest bars, while CuHARS of similar mass concentration of copper were less toxic (higher bars). The low concentration of CuHARS (1 µg/ml) showed 95% or more cell viability, making it a suitable candidate to use as a carrier in delivery system for drug treatment or cell growth.

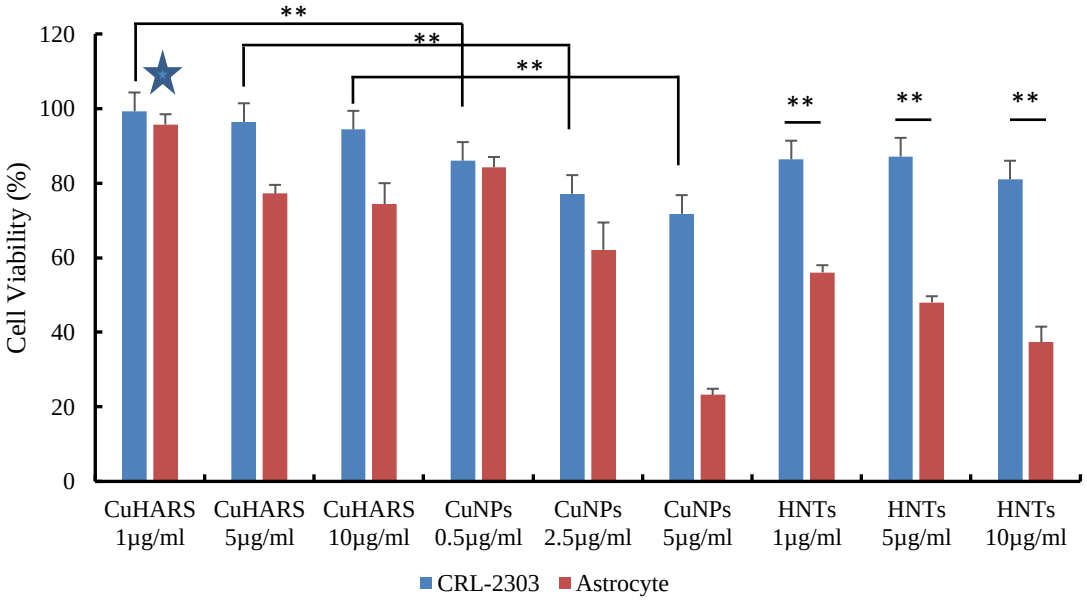

Figure 4.10: Viability assay of CRL-2303 and primary astrocytes in 2D at 4 days after addition of CuNPs, CuHARS and HNTs (concentration µg/ml). n =9 per material for each concentration, error bars represent standard deviation. The star indicated no toxicity in the concentration of CuHARS used. Data was normalized to control. Significant difference denoted by ** for $p \leq 0.01$. $\chi^2 = 137.97$, df = 17, p-value < 2.2e-16. Viability of cells treated with CuHARS was significantly higher than the ones treated with CuNP of the same amount of copper. Viability of brain tumor cells treated with HNTs was significantly higher than the astrocytes treated with HNTs of the same concentration.

Cell nuclei area of both cell types after staining with DAPI was measured and normalized as illustrated in **Figure 4.11**. Nuclei area of both cell types treated with

CuHARS showed little decrease compared to the control while primary astrocytes treated with high concentration of CuNPs demonstrated significant decrease in nuclei area compared to the control.

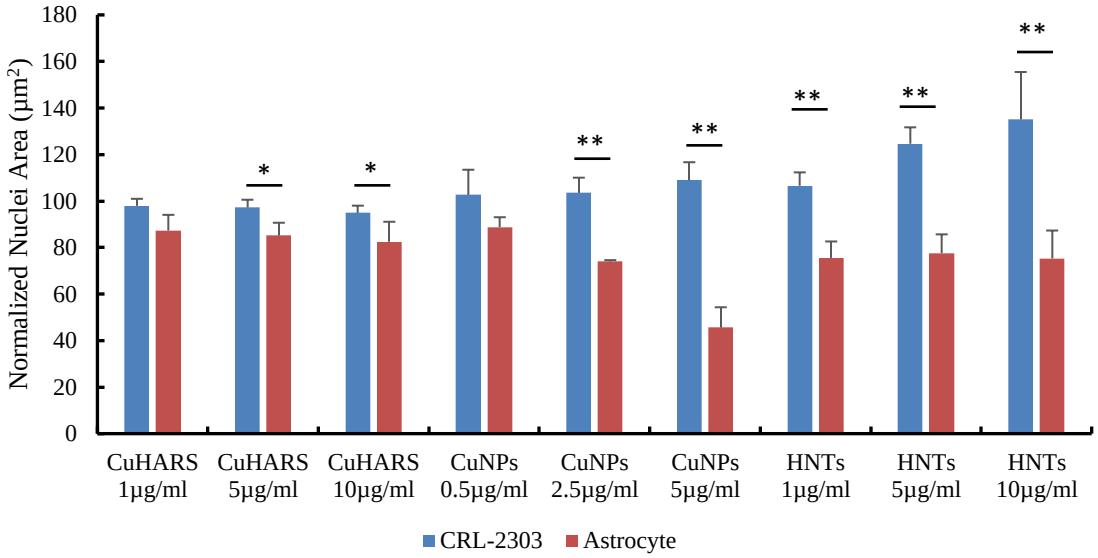

Figure 4.11: Nuclei area of primary astrocytes and gliomas 4DIV after treated with different materials and stained with DAPI, n =4 per material for each concentration, error bars represent standard deviation. Data was normalized to control. Significant difference denoted by * for $p \leq 0.05$, ** for $p \leq 0.01$. $F_{17,54} = 36.14$, p-value < 2e-16. Nuclei area of glioma cells were significantly higher than those of primary astrocytes in same treatment except for low concentration of CuHARS (1 µg/ml) and CuNPs (0.5 µg/ml).

4.3.2 Cell Viability in 3D Model

An example of high magnification captures of 3D cell spheroid 10 DIV post treatment with CuHARS and CuNPs is shown in **Figure 4.12**. In both cases, the edges of the spheroids appeared to be rough with cell debris in media nearby (especially in case of the spheroid treated with CuNPs as CuNPs was more toxic than CuHARS).

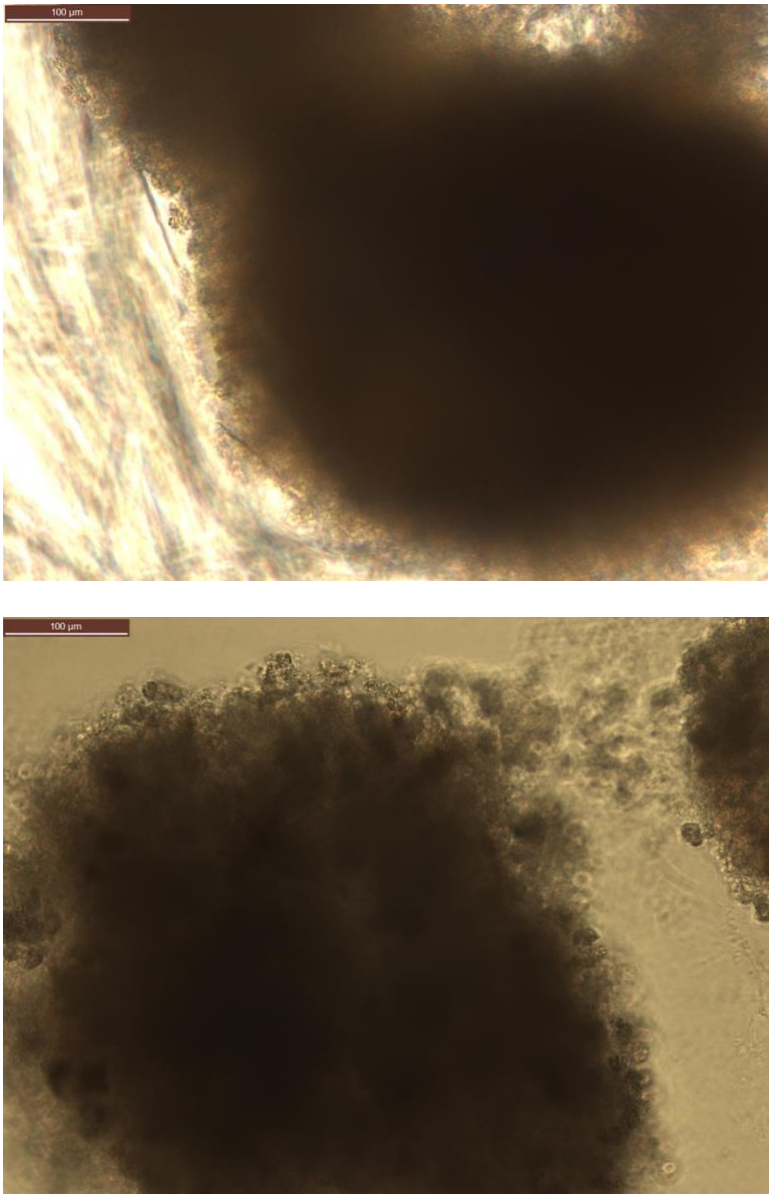

Figure 4.12: Astrocyte spheroid 10 DIV post treatment with CuHARS (25 µg/ml – top panel) and CuNPs (12.5 µg/ml – bottom panel). Pictures were taken using phase microscopy at 200x magnification. Scale bar = 100 µm.

4.3.2.1 *Interaction with CuNPs*

CuNPs were imaged under bright field microscopy, and Image Pro Plus 7.0 software was used to measure total area. **Figure 4.13** shows clearance of CuNPs in primary astrocyte (top panel) and glioma (bottom panel) 3D culture in less than 24h for

all concentrations. As confirmed in **Figures 3.26** and **3.27** (primary astrocyte) and **Figures 3.28** and **3.29** (glioma cells), CuNPs of all concentrations broke down in less than 24h, with the lowest concentration braking down completely as fast as within 5h.

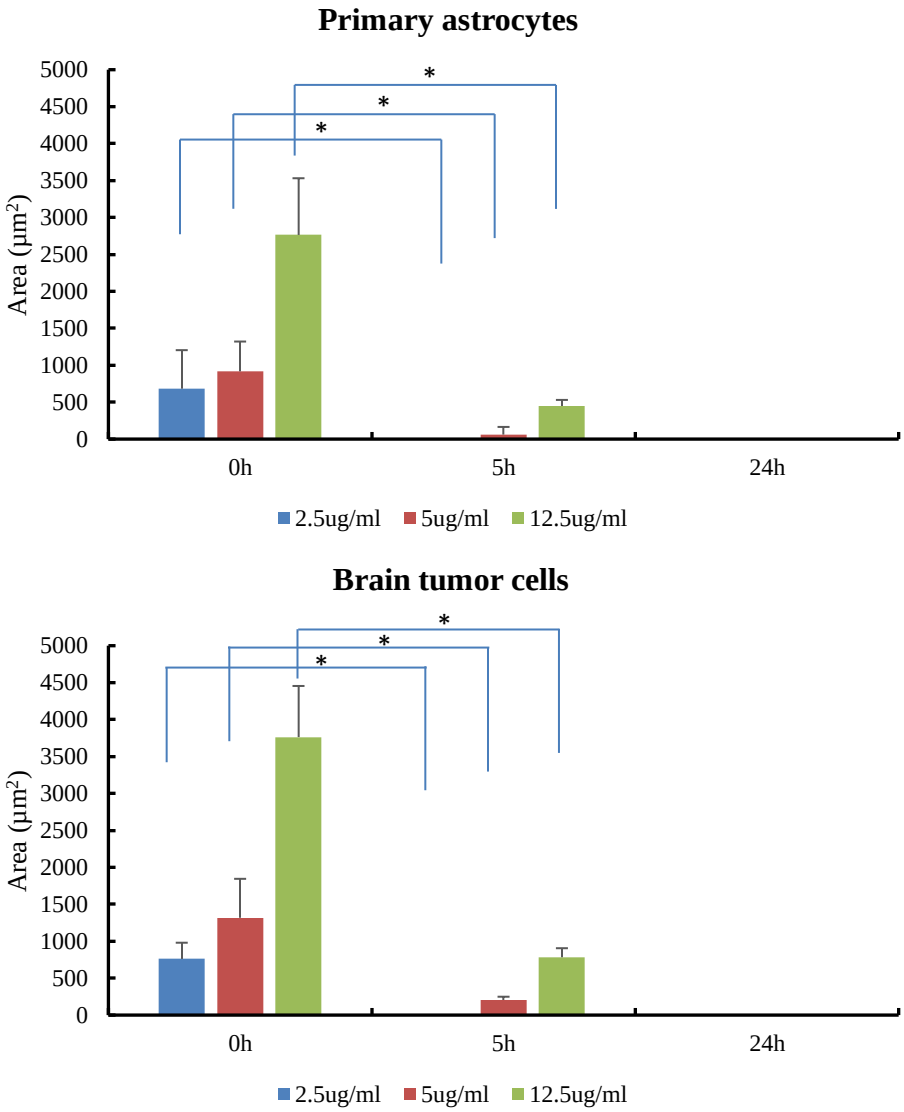

Figure 4.13: Total area of CuNPs (2.5µg/ml, 5µg/ml and 12.5µg/ml) added to astrocytes and brain tumor cells 3D spheroids. n =4 per concentration, error bars represent standard deviation. Note the complete breakdown of CuNPs of all concentrations in less than 24h. Clearance was concentration-dependent with significant difference denoted by * for $p \leq 0.05$. For astrocyte culture, $\chi^2 = 33.014$, df = 8, p-value = 6.124e-05. For glioma culture, $\chi^2 = 33.731$, df = 8, p-value = 4.544e-05.

4.3.2.2 *Interaction with CuHARS*

CuHARS were imaged under bright field microscopy, and Image Pro Plus 7.0 software was used to measure total area. As shown in **Figure 4.14** and illustrated in **Figures 3.22** and **3.23** (primary astrocyte) and **Figures 3.24** and **3.25** (glioma cells), CuHARS were not broken down as fast as CuNPs with more than 60% of CuHARS at all concentrations still present at 96h time point compared to 0h time point.

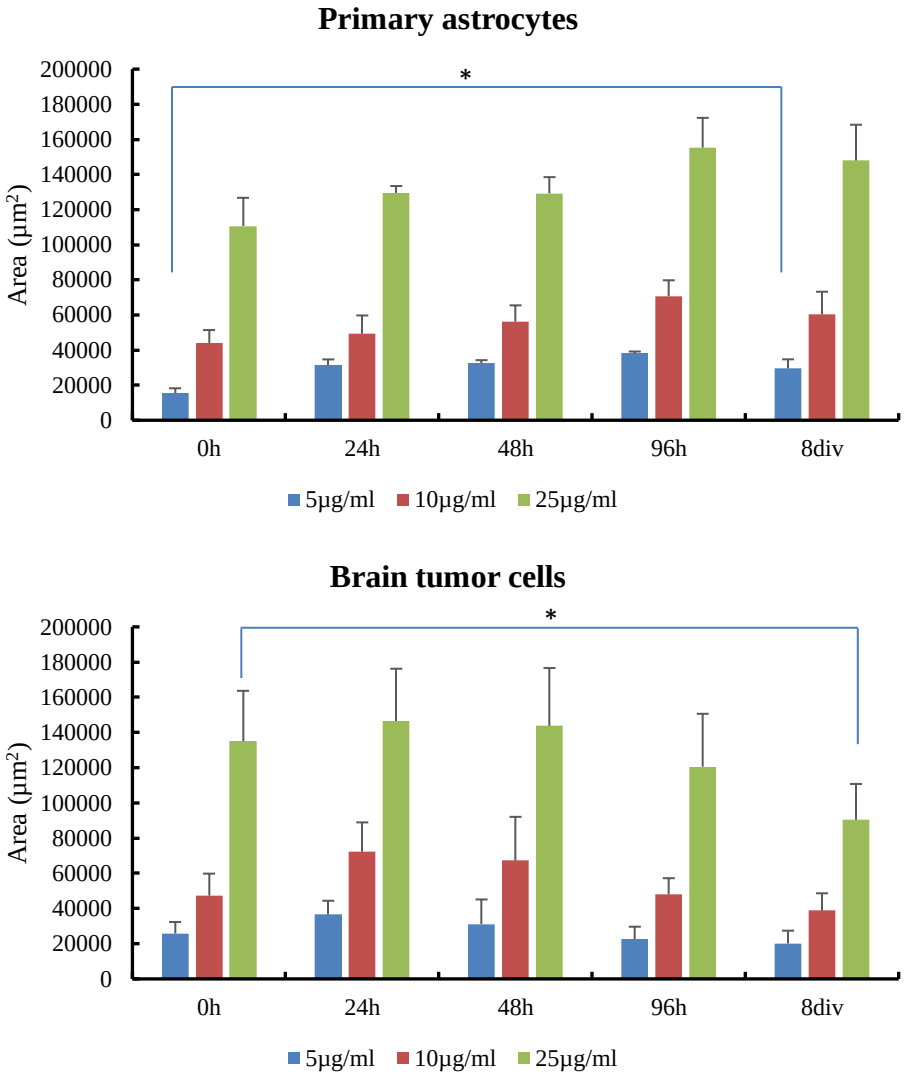

Figure 4.14: Total area of CuHARS (5µg/ml, 10µg/ml and 25µg/ml) added to astrocytes and brain tumor cells 3D models, n =4 per concentration, error bars represent standard deviation. Clearance was concentration-dependent with significant difference denoted by * for $p \leq 0.05$. For astrocyte culture, $\chi^2 = 56.466$, df = 14, p-value = 4.84e-07. For glioma culture, $\chi^2 = 57.803$, df = 14, p-value = 2.838e-07.

4.3.2.3 *Interaction with HNTs*

Fluorescent HNTs were imaged under fluorescent microscopy, and Image Pro Plus 7.0 software was used to measure total area. **Figure 4.15** shows total area of HNTs in primary astrocyte (top panel) and glioma (bottom panel) culture increased over time for all concentrations because the materials clumped and bound to the cells, as was

previously illustrated in **Figure 3.30**, **3.31** (primary astrocyte) and **Figure 3.32**, **3.33** (glioma cells).

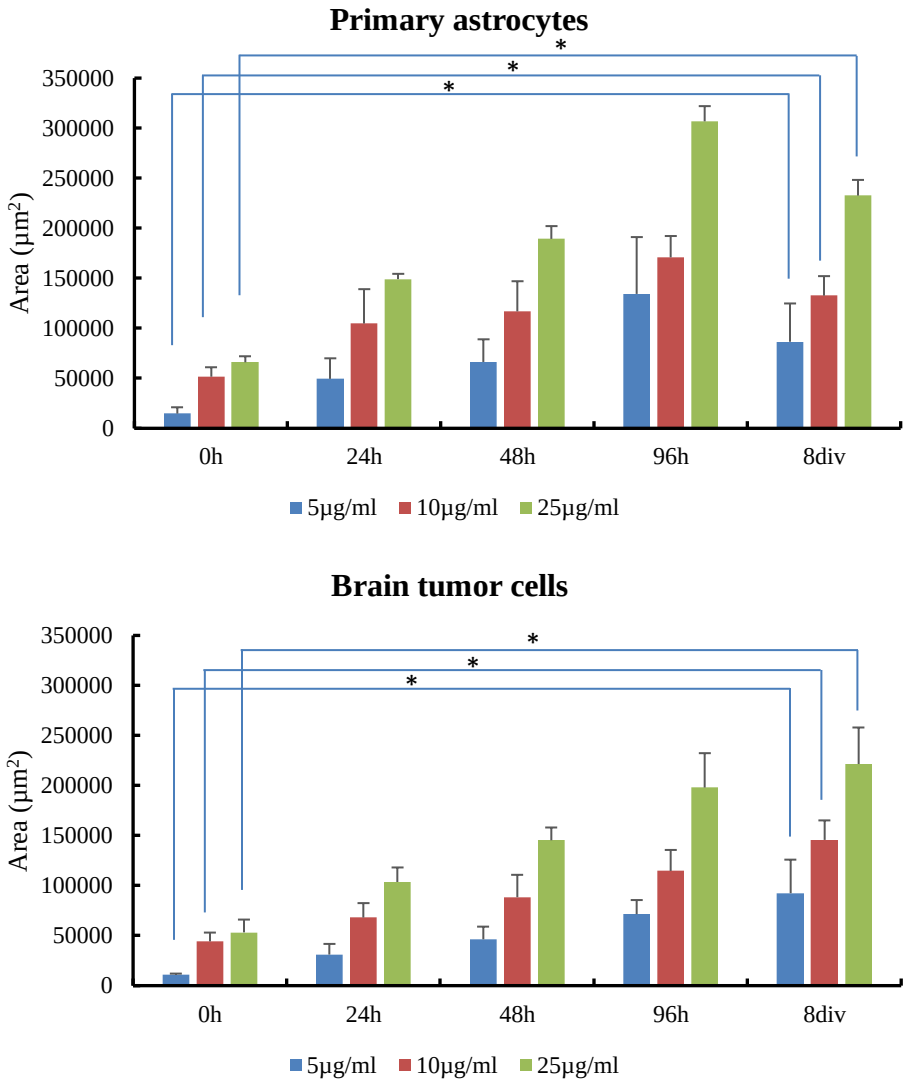

Figure 4.15: Total area of fluorescent HNTs (5µg/ml, 10µg/ml and 25µg/ml) added to astrocytes and brain tumor cells 3D models, n =4 per concentration, error bars represent standard deviation. Results were concentration-dependent with significant difference denoted by * for p≤ 0.05. For astrocyte culture, χ^2 = 51.944, df = 14, p-value = 2.874e-06. For glioma culture, χ^2 = 54.823, df = 14, p-value = 9.286e-07.

Results of the Resaruzin assay to measure glioma cell spheroid metabolism after interaction with materials are shown in **Figure 4.16**. Of all three materials, CuNPs were

the quickest to cause stress on the cell spheroid reflected by the lowest bars but glioma spheroids show sign of recurrence as the viability went up at later time point (indicated by the dashed arrow went up) while CuHARS of the similar concentration of copper illustrated a delay effect (indicated by the dashed arrow went down) as glioma spheroids at later time point were more stressed than the ones at earlier time point (the viability decreased over time). That delay effect occurs because CuHARS breaks down over time under physiological conditions, releasing the copper and causing stress to the cell spheroid, another demonstration makes it a suitable candidate to use as a carrier in delivery system for drug treatment. HNTs, meanwhile showed little to no toxicity on the spheroids at all concentrations.

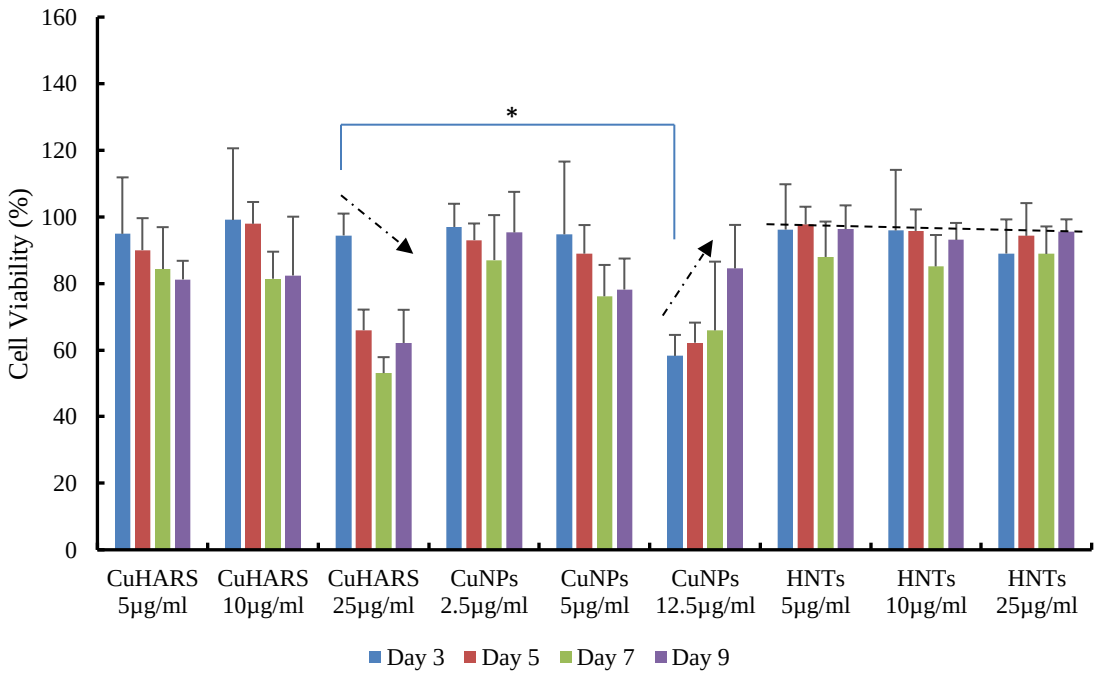

Figure 4.16: Viability assay of CRL-2303 spheroid added with CuNPs, Cu-HARS and HNTs over 3,5,7 and 9 days, n =4 per material for each concentration, error bars represent standard deviation. Data was normalized to control. Significant difference denoted by * for $p \leq 0.05$ with $\chi^2 = 77.405$, df = 35, p-value = 4.848e-05.

Resaruzin assays were also carried out to measure primary astrocyte cell spheroid metabolism after interaction with materials are shown in **Figure 4.17**. High concentration of CuNPs (25µg/ml) were significantly more toxic to the astrocyte spheroid compared to the CuHARS with same concentration of copper.

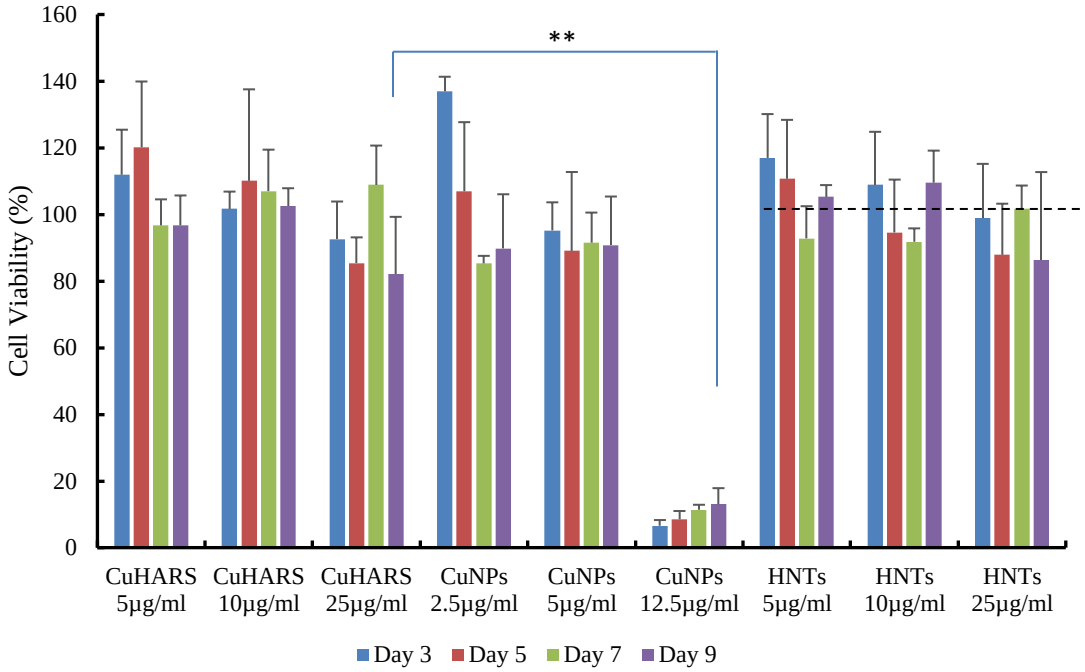

Figure 4.17: Viability assay of primary astrocyte spheroid added with CuNPs, Cu-HARS and HNTs over 3,5,7 and 9 days, n =3 per material for each concentration, error bars represent standard deviation. Data was normalized to control. Significant difference denoted by ** for $p \leq 0.01$ with $\chi^2 = 66.914$, df = 35, p-value = 0.0009246.

4.3.3 Cell Viability in Brain Tumor Cells Treated with Cancer Drug

4.3.3.1 *CRL-2303 Spheroids Treated with Cancer Drugs Cisplatin and Paclitaxel*

Results from the Resaruzin assay to measure glioma cell spheroid metabolism after interaction with cancer drugs cisplatin and paclitaxel are shown in **Figure 4.18**. Both drugs show little improvement in killing the cancer spheroid as no significant

reduction in cell viability from day 3 to day 9 *in vitro* occurred due to the aggressiveness of glioma.

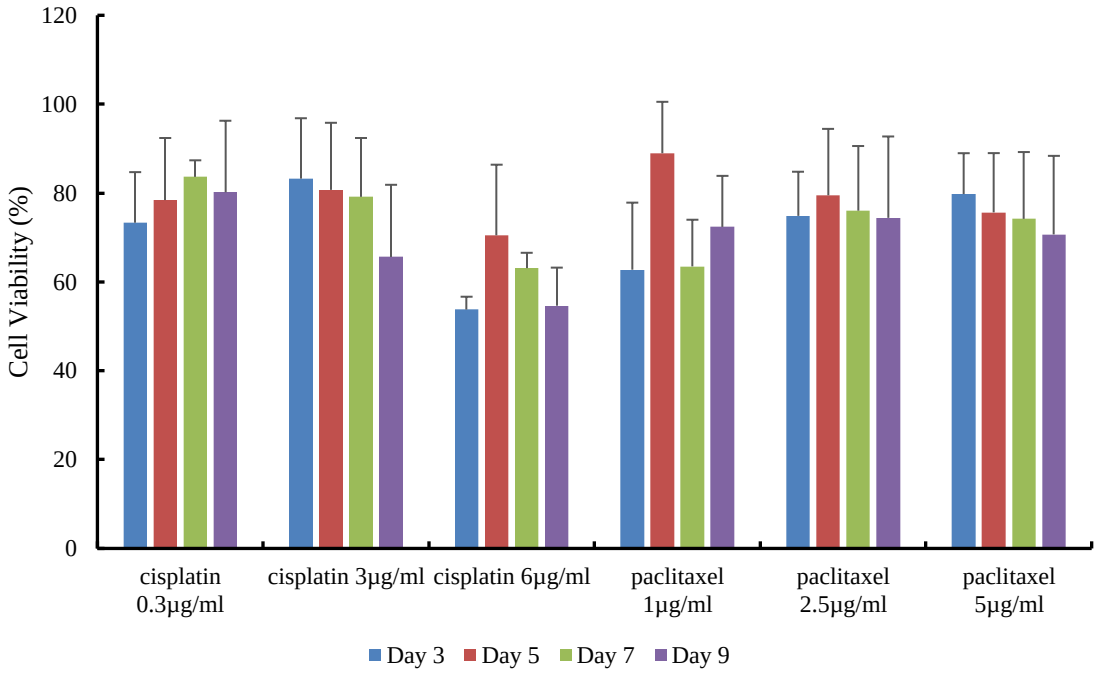

Figure 4.18: Viability assay of CRL-2303 spheroid added with cisplatin, and paclitaxel over 3,5,7 and 9 days (concentration µg/ml), n =4 per drug for each concentration, error bars represent standard deviation. Data was normalized to control. $\chi^2 = 31.57$, df = 23, p-value = 0.1094. There was no significant difference in cell viability between treatment groups.

4.3.3.2 *CRL-2303 Treated with Disulfiram.*

Viability of glioma cells treated with DSF in both 2D and 3D models was investigated and illustrated in **Figures 4.19** and **4.20**. In the 2D cell culture model (**Figure 4.19**), DSF was effective in killing glioma cell as a DSF concentration of 300nM shows 40% reduce in cell metabolism and increases to 65% at 500nM concentration of DSF. However, the effect of DSF was significantly decreased in 3D model, as shown in **Figure 4.20** as a DSF concentration of 50µM displays only 20% decrease in cell metabolism 6 DIV post treatment.

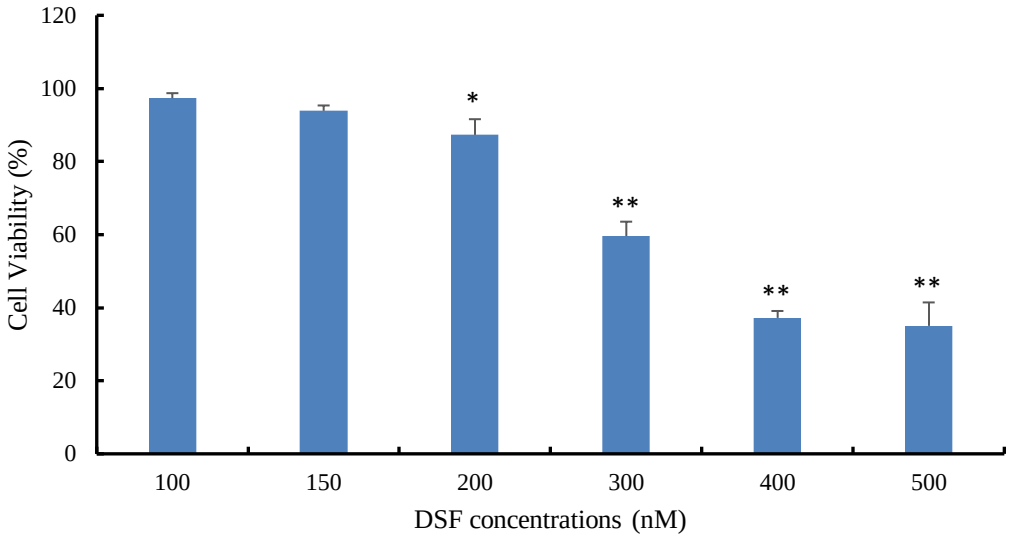

Figure 4.19: MTT assay of 2D model of CRL-2303 (10k cells/well) treated with different concentration of DSF after 24h, n =3 per concentration, error bars represent standard deviation. Data was normalized to control. Significant difference from control denoted by * for $p \leq 0.05$, ** for $p \leq 0.01$. $\chi^2 = 19.013$, df = 5, p-value = 0.004142. There was a significant decrease in cell viability of glioma cells treated with 200, 300, 400 and 500 nM concentrations of DSF compared to control.

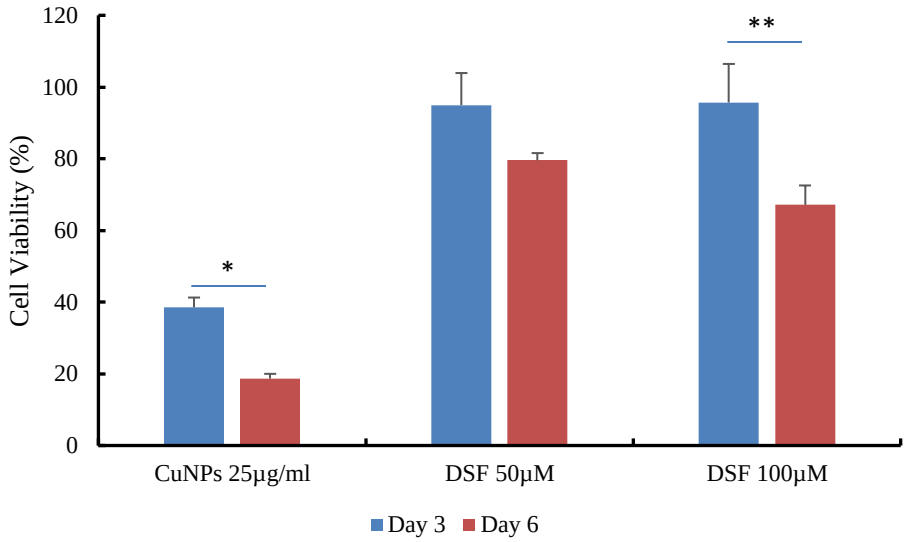

Figure 4.20: Viability assay of CRL-2303 spheroid treated with CuNPs and different concentrations of DSF after 3 and 6 days. n =3 per material for each concentration, error bars represent standard deviation. Much higher concentrations of DSF (50, 100 µM) compared to 2D model were used due to the larger number of cells (200k cells vs. 30k cells in 2D model). Data was normalized to control. Significant difference denoted by * for $p \leq 0.05$, ** for $p \leq 0.01$. $\chi^2 = 19.117$, df = 5, p-value = 0.003971. There was a significant decrease in cell viability of spheroids treated with CuNPs on both time points and spheroids treated with DSF of both concentrations on day 6 compared to control.

Viability of glioma cells treated with the combination of DSF and CuHARS in 2D model was investigated and shown in **Figures 4.21** and **4.22**. As displayed in **Figure 4.21**, the combination of DSF and CuHARS (panel B) was more effective than DSF alone in killing glioma cells, as indicated by more round cells (**Figure 4.21** –panel B & C) and MTT result (**Figure 4.22**). The combination of DSF and CuHARS caused significantly more toxicity to brain tumor cells than DSF alone (40 & 80% compared to 16% decrease in cell metabolism).

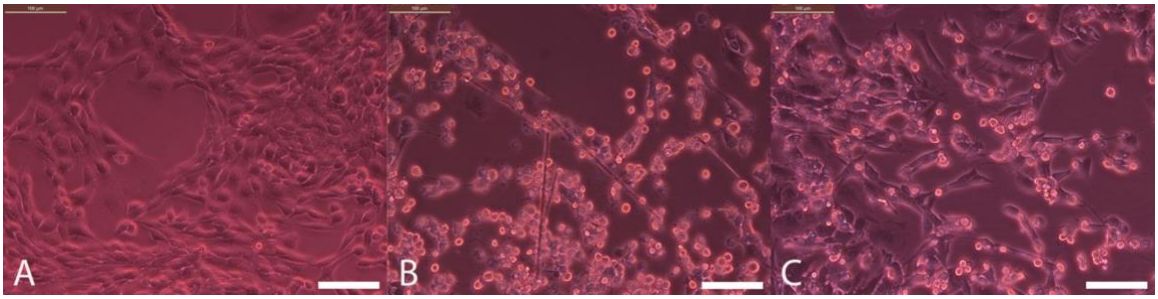

Figure 4.21: Interaction of CRL-2303 with the combination of CuHARS and DSF. Cells were plated at 10k cells/well. CuHARS were added 1 day while DSF was added 4 days after cells attached. Pictures were taken 24h post DSF addition: control (panel A), 5µg/ml CuHARS and 250nM DSF (panel B) and 250nM DSF (panel C) at 200x magnification. Scale bar = 100 µm.

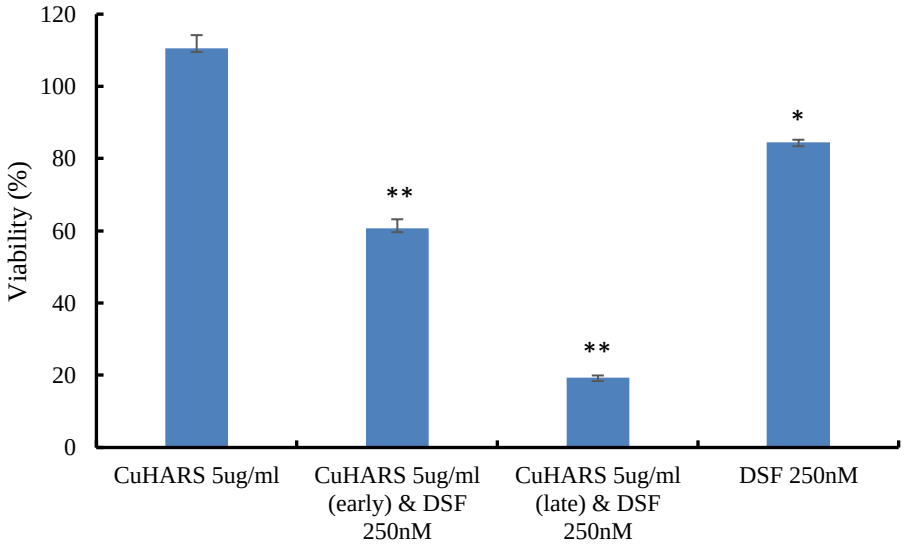

Figure 4.22: Viability assay of 2D model of CRL-2303 24h post treatment of DSF combined with CuHARS. Cells were plated at 10k cells/well. CuHARS were added 1 and 3 days while DSF was added 4 days after cells attached. Data were normalized to control plus standard deviation, n = 3 per material for each concentration. Significant difference from control denoted by * for $p \leq 0.05$, ** for $p \leq 0.01$. $\chi^2 = 13.5$, df = 4, p-value = 0.009074. There was a significant decrease in cell viability of gliomas treated with combinations of CuHARS and DSF compared to control and the ones treated with CuHARS and DSF alone.

Disulfiram (DSF) has been widely used in alcoholism treatment in the last six decades. DSF inhibits the aldehyde dehydrogenase (ALDH) enzyme family (which is

involved in the metabolism of alcohol), and has shown great potential in targeting cancer cell [17], [97].

Although the anticancer mechanisms of DSF are still not fully understood, studies have indicated that DSF chelates bivalent metals such as copper (Cu) and zinc (Zn) to form DSF metal complexes that inhibit proteasome activity and block the degradation of IκB and NFκB nuclear translocation [97]. In other words, the presence of copper increases the effect of DSF.

As the data show in this study, a combination of novel copper-contained biomaterial CuHARS with DSF showed significant increase in cancer cell death compared to DSF alone. This study can be used as a foundation for a therapeutic approach for effective cancer treatment by incorporating DSF into CuHARS for targeted drug delivery.

Figure 4.23 shows the interaction of DSF and CuHARS in sterile water. As mentioned above, DSF could form metal complex with copper, such as that in CuHARS. The combination of both DSF and CuHARS led to new structures (blue arrows) that did not appear when both materials were put separately in sterile water.

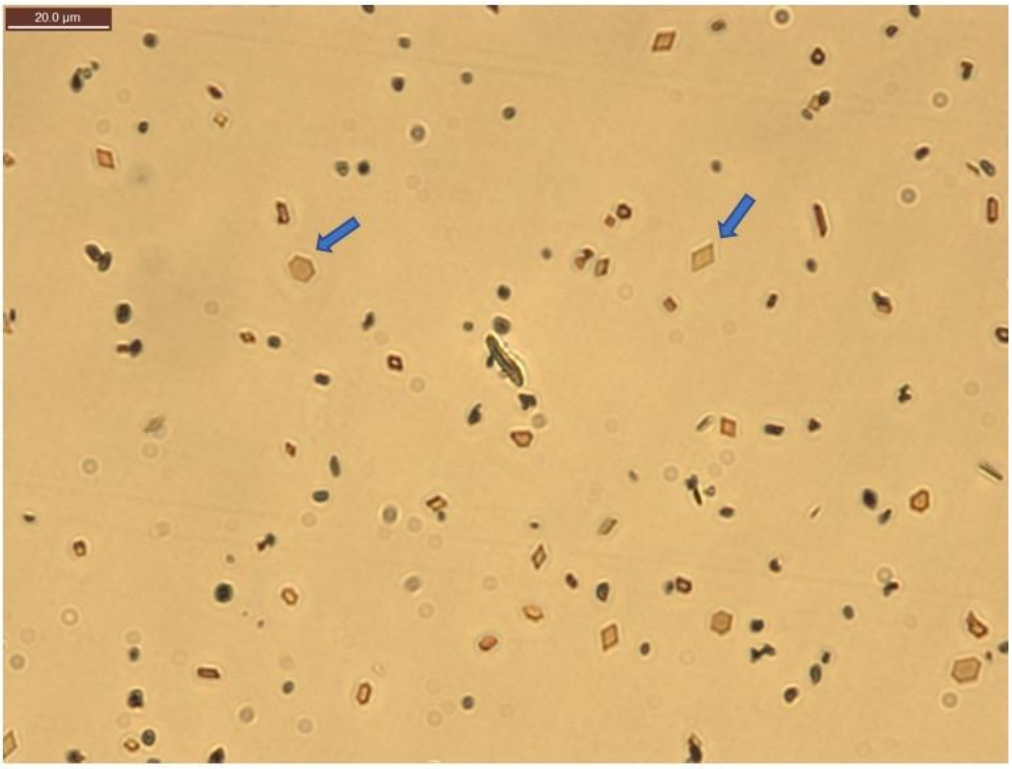

Figure 4.23: Combination of DSF and sonicated CuHARS in water. Pictures were taken using bright field microscope at 630x magnification. Scale bar = 20 µm.

The same viability study with combination of DSF and CuHARS was also carried out in 3D model (**Figure 4.24).** All combinations of DSF and CuHARS showed much improvement in suppressing glioma viability as cell metabolism reduced to 25%-43%, compared to 95% with DSF alone.

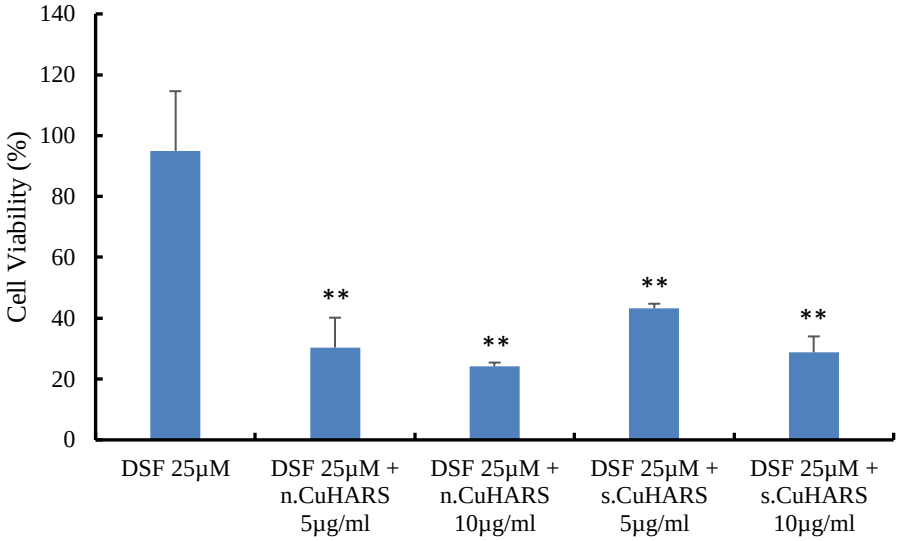

Figure 4.24: Viability assay of CRL-2303 spheroid treated with combination of DSF and non-sonicated and sonicated CuHARS 7 DIV post treatment, n =3 per material for each concentration, error bars represent standard deviation. Data was normalized to control. Significant difference from control denoted by ** for $p \leq 0.01$. $\chi^2 = 14.52$, df = 5, p-value = 0.01262. There was a significant decrease in cell viability of glioma spheroids treated with combinations of CuHARS and DSF compared to control and the ones treated with DSF alone.

4.4 Discussion

Of all three materials, CuNPs degraded fastest in both 2D and 3D models. CuNPs broke down completely in 3-5h at low concentrations and in less than 24h at all concentrations (**Figures 4.5** and **4.13**). CuNPs also caused most toxicity to the cells in 2D model (lowest cell viability – **Figure 4.10**) and initially in 3D model at high concentrations (**Figures 4.16** and **4.17**) but the cell recovered over time, especially in the case of gliomas (cell viability went up over time). On the other hand, CuHARS showed low stress on the cells in 2D model and initially in 3D model, but as the material broke down over time, cell viability decreased, indicating a delay effect on both cell types. Moreover, the combination of CuHARS and DSF to form DSF metal complex showed significantly increase in growth inhibition of gliomas in both 2D and 3D models (**Figures**

4.22 and **4.24**) suggesting a promising approach in treating gliomas that needed further investigation.

CHAPTER 5

MODIFICATION OF THE CUHARS

5.1 Overview

As previously discussed, CuHARS has the potential to be used as a delivery system for drug treatment or cell growth promotion as well as in combination with other chemicals/drugs for cancer treatment (DSF). One of the challenges with the current synthesized CuHARS is the large variability in size of the material. Some CuHARS can have the length of up to 200 μm or more, making them too long for the cells to uptake and also taking longer time to break down. The goal of this chapter is to introduce a simple method to modify the CuHARS to get a more uniform size and shape for better carrier and interaction with cells.

5.2 Materials and Methods

5.2.1 Materials

CuHARS after synthesis as described [9]–[11], [14] at concentration of 2mg/ml. Microcentrifuge tubes 0.65 ml (VWR, 87003-290) for sonicating CuHARS.

5.2.2 Cell Types

Rat brain astrocytes are harvested from the cortex of newborn rats and cultured in astrocyte medium (Ham's F-12K) containing 10% horse serum and other components (**Appendix A, Section A.2)**. The cells were plated in a cell culture 48 wells plate at the

density of 20,000 cells/mL and grown in an incubator with 5% CO_2 and at 37°C for 5 DIV before adding the materials.

5.2.3 Sonication

CuHARS was added to 0.65 ml plastic vial at the concentration of 1 mg/ml and total volume is 400 µL. The vial was then sonicated in Branson 1510 Ultrasonic Cleaner for 20 minutes. During the sonication process, CuHARS were checked to ensure that they did not settle down to the bottom of the vial.

5.2.4 Image Analysis

Image Pro-Plus software version 7.0 developed by Media Cybernetics (Rockville, MD) was used to measure length and area of the CuHARS.

5.2.5 Statistics

Data analysis was performed in R software and the significance of the test results was analyzed using Kruskal-Wallis test to evaluate the hypothesis that the length and area of the CuHARS before and after sonication were significantly different. The null hypothesis was that the length and area of the CuHARS did not change after sonication. A p-value less than 0.05 was considered statistically significant.

5.3 Results

5.3.1 Comparison of CuHARS before and after Sonication

CuHARS before and after sonication is shown in **Figure 5.1**. On the left panel, the non-sonicated CuHARS displayed varieties in length with some reaching lengths up to 80µm while the sonicated CuHARS on the right panel demonstrated a much more uniform length.

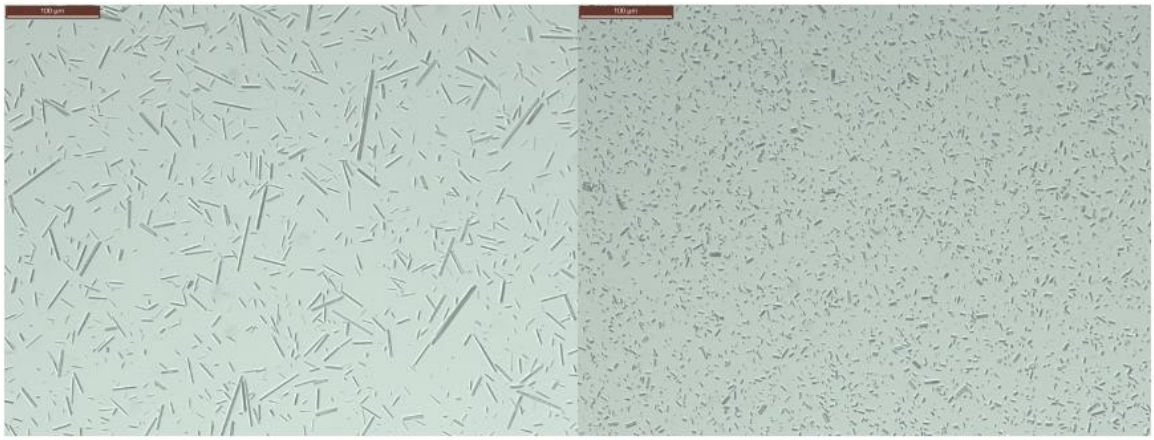

Figure 5.1: CuHARS before (left panel) and after (right panel) sonication. CuHARS were diluted to a final concentration of 10 µg/ml in sterile water. Pictures were taken using bright field microscope at 200x magnification. Scale bar = 100 µm.

High magnification picture of **Figure 5.1** right panel is shown in **Figure 5.2**. The sonicated CuHARS appeared to retain properties in sterile water with no big clumps as the material carries a negative charge [14].

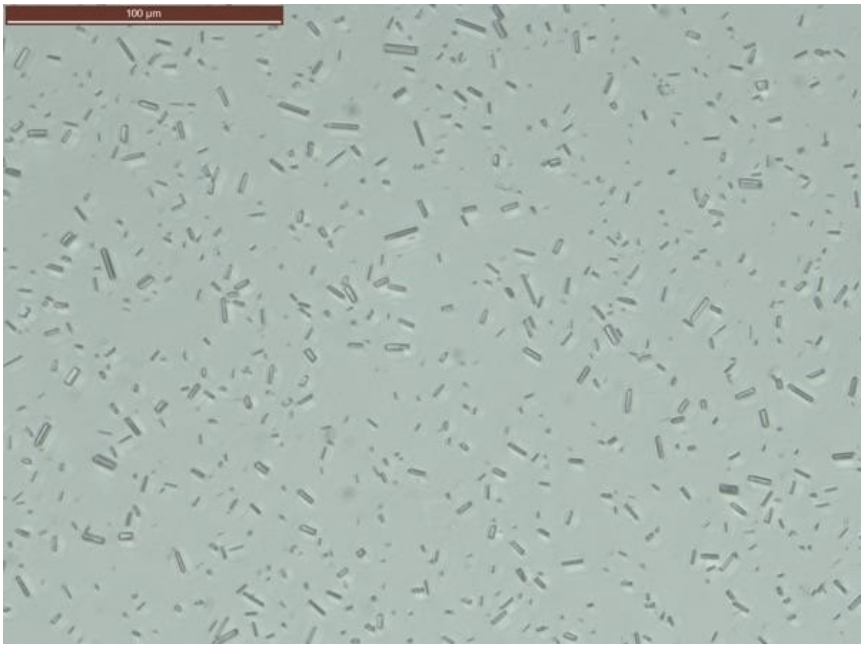

Figure 5.2: CuHARS after sonication. CuHARS were diluted to a final concentration of 10 µg/ml in sterile water. Pictures were taken using bright field microscope at 400x magnification. Scale bar = 100 µm.

Figure 5.3 compares the population and total area of the CuHARS before and after sonication. Even though the breakdown of longer CuHARS to shorter ones caused the number of sonicated CuHARS to increase 3-fold compared to the non-sonicated CuHARS, the total area of sonicated CuHARS shows no significant increase/decrease compared to non-sonicated CuHARS indicating no material was lost during the sonication process.

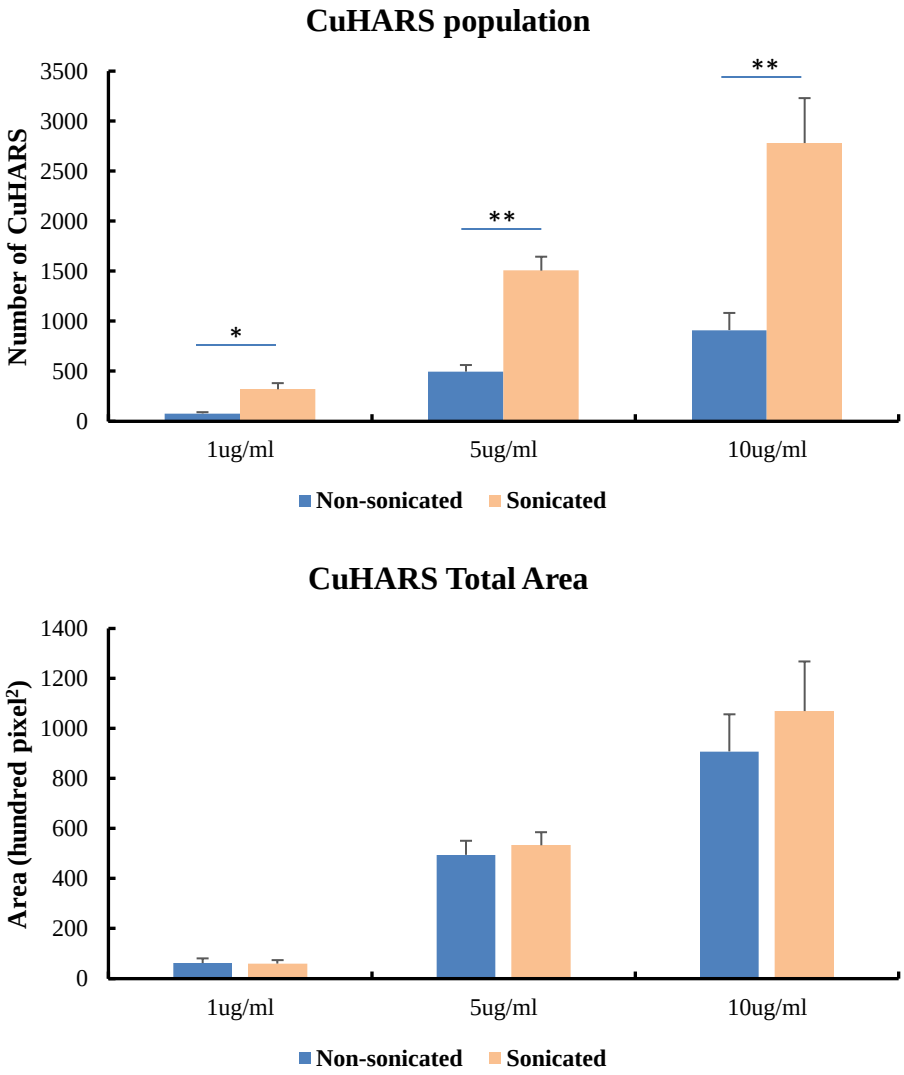

Figure 5.3: Comparison in number (top graph) and total area (bottom graph) of CuHARS before and after sonication. Results were concentration-dependent with significant difference denoted by * for $p \leq 0.05$, ** for $p \leq 0.01$. For number of CuHARS before and after sonication, $\chi^2 = 28.232$, df = 5, p-value = 3.279e-05. For total area of CuHARS before and after sonication, $\chi^2 = 26.13$, df = 5, p-value = 8.419e-05.

The CuHARS area before and after sonication is presented in **Figure 5.4**. The majority of sonicated CuHARS have an area within the range of 2-8 μm^2 (66.9%), and only 4.3% of CuHARS have area equal or larger than 24 μm^2 (4.3%). Most (61.6%) of the non-sonicated CuHARS had an area between 2-14 μm^2, but many had area equal or greater than 24 μm^2 (22.1%).

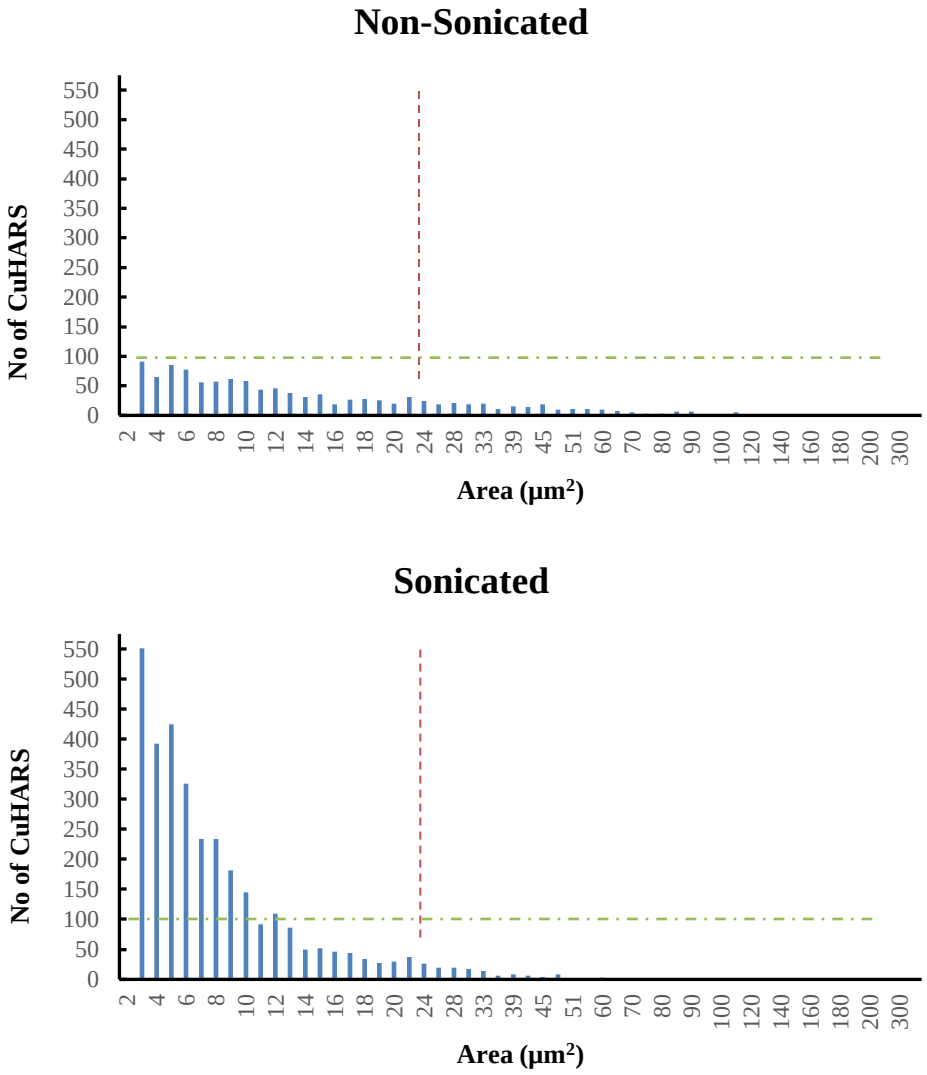

Figure 5.4: Histogram comparison in size (µm^2) of CuHARS before (top graph) and after (bottom graph) sonication.

The CuHARS length distributions are shown in **Figure 5.5**. Most (93.2%) of sonicated CuHARS have a length within the range of 2-8 µm, and almost none have length equal or larger than 10 µm (4.3%). The length of most non-sonicated CuHARS, (62.2%) varies from 2-11 µm, but 21% have length equal to or greater than 17 µm.

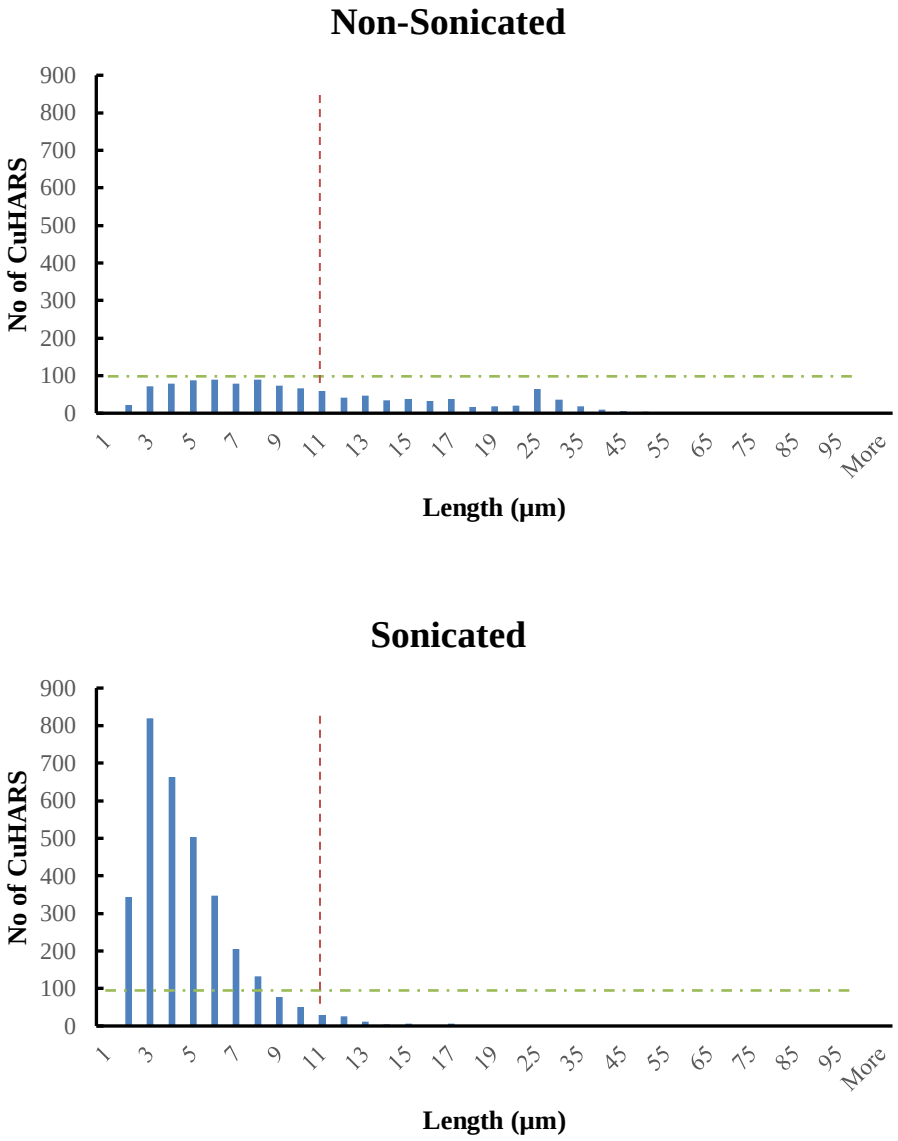

Figure 5.5: Histogram comparison in length (µm) of CuHARS before (top graph) and after (bottom graph) sonication.

5.3.2 Comparison of CuHARS before and after Sonication in Cell Culture

Clearance of non-sonicated and sonicated CuHARS in primary astrocyte culture over time is displayed in **Figures 5.6** and **5.7**. While most of the sonicated CuHARS broke down after 6 DIV and completely disappeared in 16 DIV (**Figure 5.7** panel D2, F2), many non-sonicated CuHARS were still present in the culture after 16 DIV (**Figure**

5.6 panel F2). Moreover, the reduced, uniform size of the sonicated CuHARS, which helped the cells bind/uptake the material easier, makes them better carriers for drug delivery compared to the non-sonicated CuHARS.

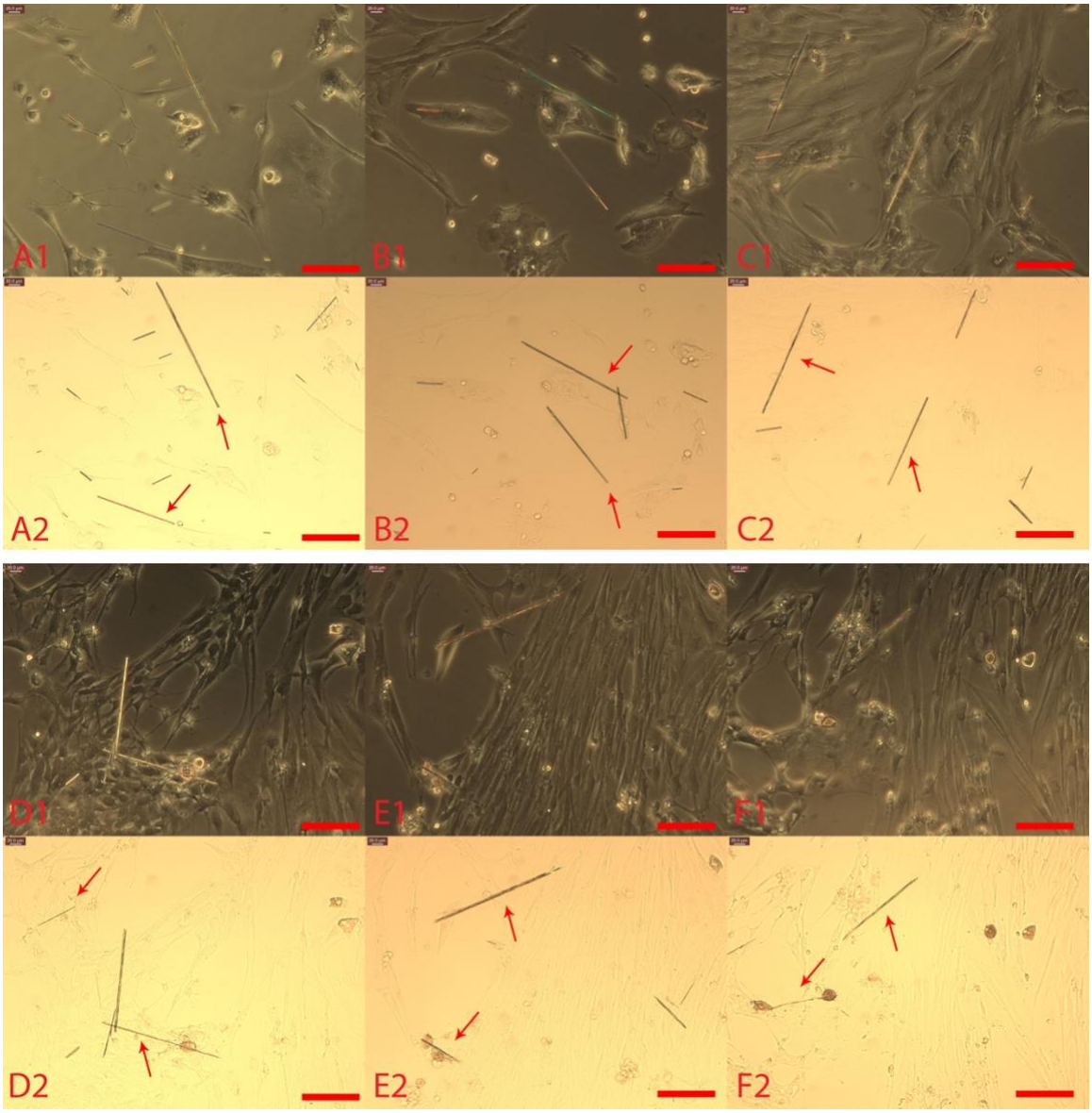

Figure 5.6: Interaction of non-sonicated CuHARS (1 µg/ml concentration) with primary astrocytes. Cells were plated at 20k cells/well and CuHARS were added 5 days after cells attached. Panels 1 and 2 were taken of the same areas with pictures A1, B1, C1, D1, E1, F1 were taken using phase microscopy, pictures A2, B2, C2, D2, E2, F2 were taken using bright field microscopy. Pictures were taken at 0h (panel A), 24 (panel B), 48h (panel C), 6div (panel D), 12 div (panel E) and 16 div (panel F) post addition at 200x magnification. Red arrows indicate CuHARS. Scale bar = 100µm.

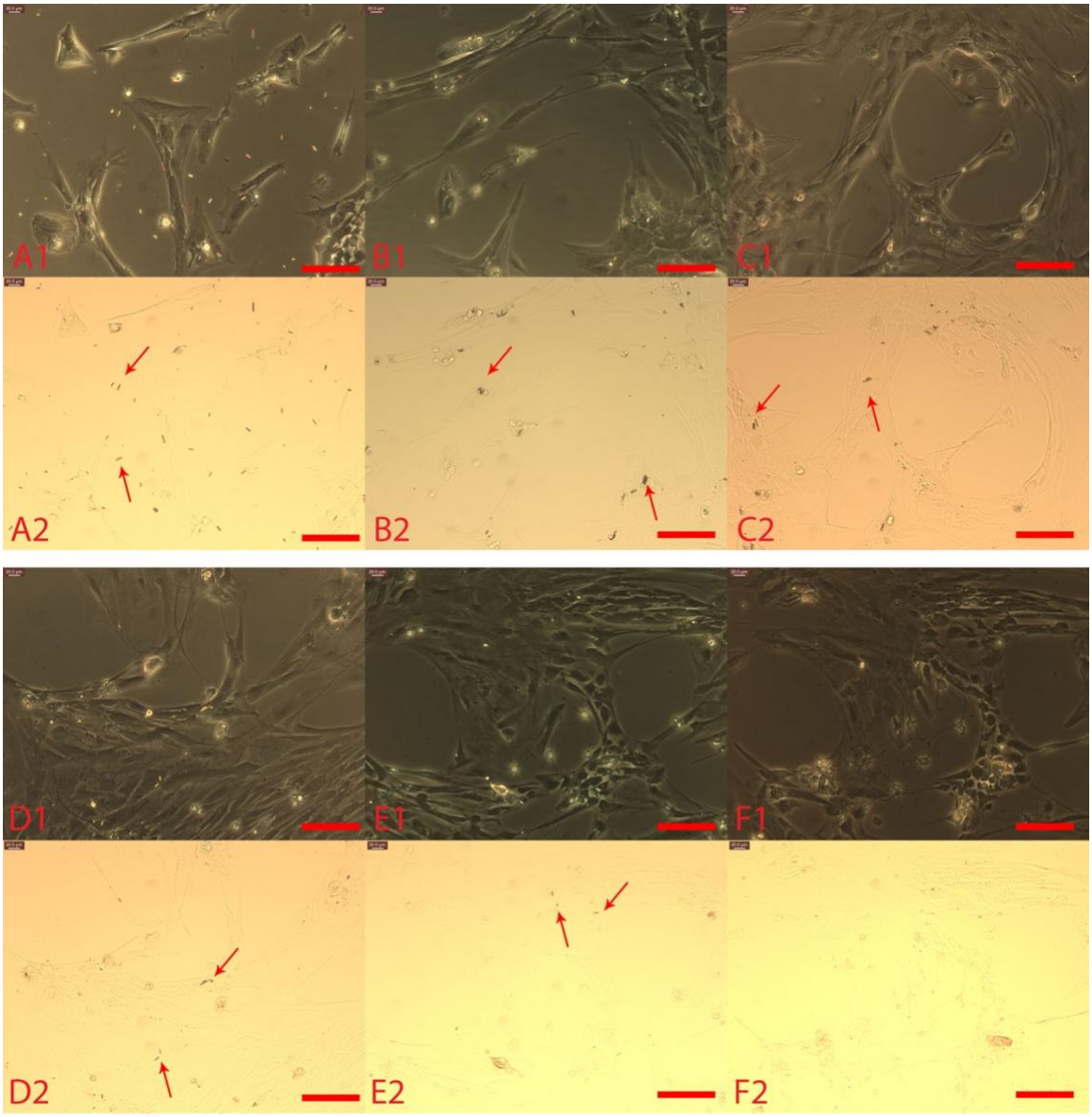

Figure 5.7: Interaction of sonicated CuHARS (1 µg/ml concentration) with primary astrocytes. Cells were plated at 20k cells/well and CuHARS were added 5 days after cells attached. Panels 1 and 2 were taken of the same areas with pictures A1, B1, C1, D1, E1, F1 were taken using phase microscopy, pictures A2, B2, C2, D2, E2, F2 were taken using bright field microscopy. Pictures were taken at 0h (panel A), 24 (panel B), 48h (panel C), 6div (panel D), 12 div (panel E) and 16 div (panel F) post addition at 200x magnification. Red arrows indicate CuHARS. Scale bar = 100µm.

Analysis of both non-sonicated and sonicated CuHARS clearance over time is shown in **Figure 5.8**, which confirms the complete breakdown of sonicated CuHARS

after 16 DIV for all concentrations, compared to the presence of the non-sonicated CuHARS after 16 DIV even at low concentration (1µg/ml).

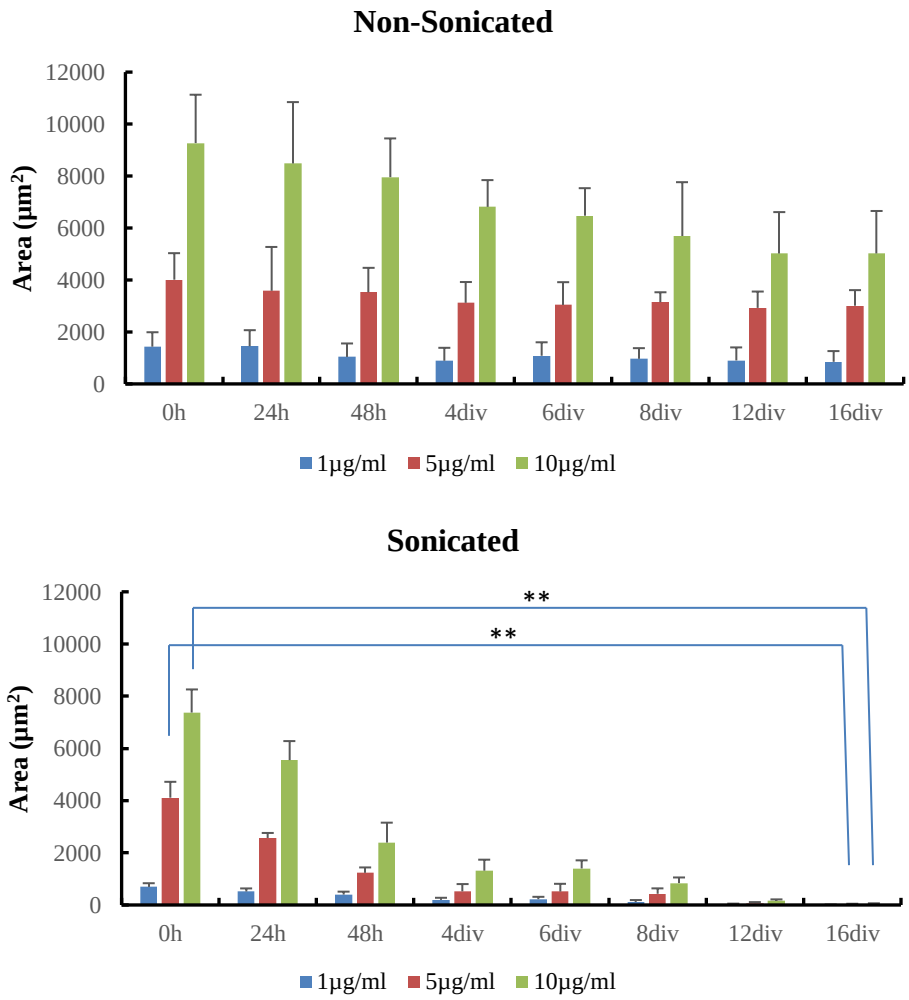

Figure 5.8: Total area of CuHARS (1µg/ml, 5µg/ml and 10µg/ml) in primary astrocytes culture over time. n =3 for each concentration, error bars represent standard deviation. Results were concentration-dependent with significant difference denoted by ** for p≤ 0.01. For the CuHARS before sonication, χ^2 = 84.622, df = 23, p-value = 5.579e-09. For the CuHARS after sonication, χ^2 = 99.914, df = 23, p-value = 1.457e-11. All concentrations of non-sonicated CuHARS showed no significant decrease in terms of total area at 16div time point compared to 0h time point while medium and high concentrations of sonicated CuHARS showed significant decrease in terms of total area at 16div time point compared to 0h time point.

5.4 Discussion

CuHARS after sonication displayed a much more uniform size and length compared to the ones before modification, with the majority of CuHARS having lengths of less than 7 µm in contrast to the non-sonicated CuHARS which had numerous examples with length of 35 µm or longer. Moreover, characteristics of the material appeared to be unchanged after modification. The smaller size of sonicated CuHARS helped to increase the chances for the material being taken up by or bound to the cells, and it accelerated the degradation of the materials (**Figure 5.7** and **Figure 5.8**) which in turn made the sonicated CuHARS a promising candidate to be used as a delivery system.

CHAPTER 6

CO-CULTURE MODELS OF PRIMARY ASTROCYTES AND GLIOMAS TO STUDY CANCER MICROENVIRONMENT

6.1 Overview

Since the brain and almost all other organs consist of not one but many different cell types, co-culture models (both 2D and 3D) are important tools to investigate cell-cell interaction in addition to cell response to drugs and other materials [98]. The goal of this chapter is to demonstrate cell interaction in a traditional 2D model and to use our novel matrix free technique of making 3D spheroid in building models of co-culture of both normal brain cells and glioblastoma. This will allow us to better understand cell behavior in different environments before performing to *in vivo* studies.

6.2 Materials and Methods

6.2.1 Cell Types

Rat brain glioma cells CRL-2303 (C6/lacZ7) were obtained from American Type Culture Collection (ATCC) and cultured in DMEM containing 10% FBS and other components (**Appendix A, Section A.1)**.

Rat brain astrocytes are harvested from the cortex of newborn rats and cultured in astrocyte medium (Ham's F-12K) containing 10% horse serum and other components (**Appendix A, Section A.2)**.

6.2.2 Methods

For the 2D co-culture experimental model, glioma cells (CRL-2303) and normal brain astrocytes were placed at the ratio 1:3 in their respective growth media into the same well in a 48-well cell culture plate (Griener) and allowed to grow in an incubator with 5% CO_2 and 37°C for 3 days.

For the 3D co-culture experimental model, glioblastoma and primary astrocytes were placed at different ratios in their respective growth media into the same well in a 48-well suspension plate to form a spheroid using the Matrix-free system (Nanogaia #SSD-01, Ruston, LA - http://www.nanogaia.com/) and allowed to grow for 5 DIV before staining.

6.2.3 Cell Fixation

After 3 days *in vitro*, the growth medium from the cells was aspirated and washed twice with 500 µL 1X PBS. Cells were fixed in the fixation solution from β-gal kit (**Appendix H, Section H.1 and H.2**) such that it covers the entire well, and the plate was kept at room temperature for 10 minutes. The cells were rinsed twice with 500 uL 1X PBS again.

6.2.4 GFAP Staining

To confirm normal *in vitro* characteristics, cells were stained using indirect immunofluorescence for glial fibrillary acidic protein (GFAP), a cytoskeletal protein found specifically in glial cells. Cells were stained using Anti-Glial Fibrillary Acidic Protein (Anti-GFAP), antibody produced in rabbit as 1° Ab from Sigma-Aldrich (Sigma Product #G9269), and Alexa Fluo® 488 goat anti-rabbit IgG (H+L) as 2° Ab from Invitrogen Molecular Probes (Invitrogen Product #A-11035) (**Appendix G**).

6.2.5 β-galactosidase Staining

As the GFAP stained both astrocytes and glioma cells, CRL-2303 cells were counterstained with β-gal staining to distinguish between the cell types in a co-culture experimental model (**Appendix H, Section H.3**). A β-galactosidase Reporter Gene Staining Kit was obtained from Sigma-Aldrich (Sigma Product #GALS).

6.2.6 Image Analysis

Image Pro-Plus software version 7.0 developed by Media Cybernetics (Rockville, MD) was used to determine the total area covered by normal brain astrocytes and glioma cells from the GFAP and β-gal staining in each image.

6.3 Results

6.3.1 2D Co-Culture of Glioma and Primary Astrocytes

Co-culture of glioma and astrocytes stained with GFAP is shown in **Figure 6.1**. Both glioma and primary astrocytes stained positive for GFAP because glioma cells were derived from the astrocytes [41], [42], [99]–[101].

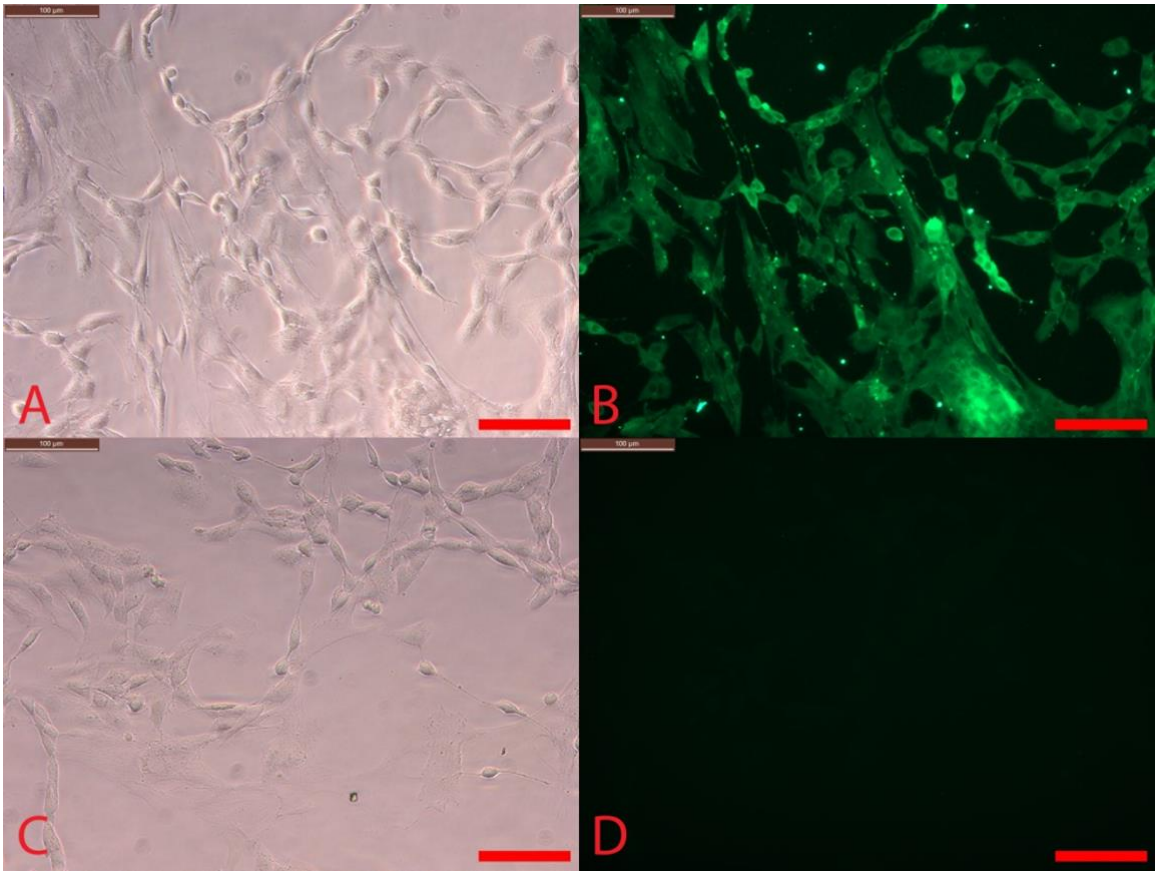

Figure 6.1: GFAP staining for co-culture of 4,000 glioma and 12,000 primary astrocytes cells per ml. Panel A and C represent phase image of the cells before and GFAP staining while panel B (with 1° Ab) and D (without 1° Ab) represent fluorescence images of respective area after GFAP staining. Scale bar = 100 µm.

Since GFAP stains both glioma and astrocyte cells, β-galactosidase staining was used in addition to GFAP to visualize the glioma cells in co-culture environment. **Figure 6.2** shows co-culture of normal brain astrocytes and glioma cells stained with both GFAP and β-galactosidase. Both normal brain astrocytes and glioma cells (**Figure 6.2** panel A2) stained positive for GFAP staining in positive controls (1° Ab + 2° Ab) while negative controls (no 1° Ab) (**Figure 6.2** panel B2) did not show staining. β-galactosidase stained the glioma cells but not the normal brain astrocytes an indigo blue color in a co-culture model. **Figure 6.2,** panels A3 and B3, show positive β-galactosidase staining of gliomas.

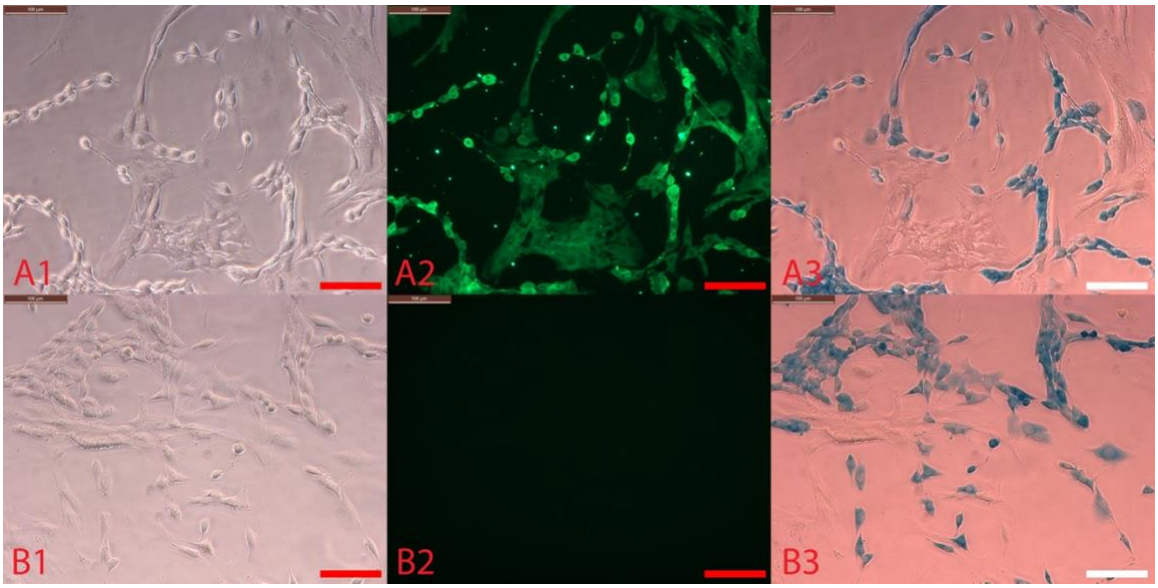

Figure 6.2: GFAP and β-galactosidase staining for co-culture of 4,000 cells/ml gliomas (CRL-2303) and 12,000 cells/ml normal brain astrocytes. Panel A1, B1 (after GFAP staining) and A3, B3 (after β-galactosidase staining) were taken using phase microscopy whereas panel A2 and B2 were taken with fluorescent microscopy (after GFAP staining). Scale bar = 100 µm.

6.3.2 3D Co-Culture of Glioma and Primary Astrocytes Spheroid

Glioma spheroid stained with β-galactosidase is shown in **Figure 6.3**. All the cells were stained with indigo blue color while a co-culture spheroid of glioma and astrocytes (**Figure 6.4**) displays areas of unstained cells, indicating the primary astrocytes. Both cell types did not spread out evenly, instead the glioma demonstrated tumorous behavior by growing into patches.

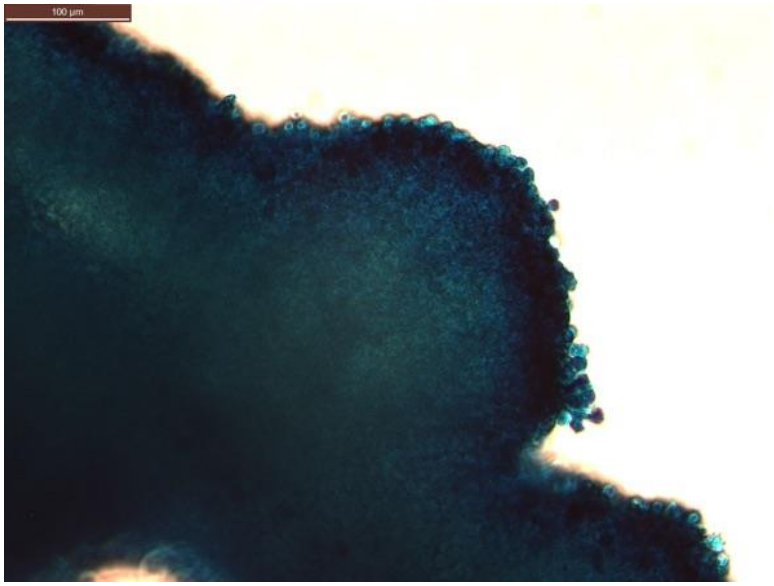

Figure 6.3: Three-dimensional spheroid of glioblastoma stained with β-galactosidase. Scale bar = 100 µm.

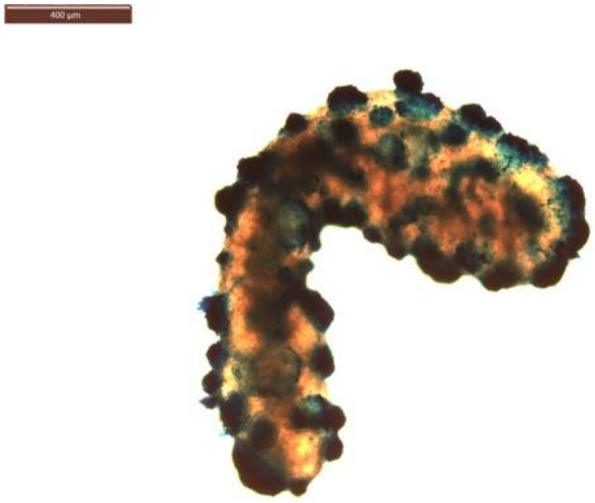

Figure 6.4: Co-culture spheroid of glioblastoma and primary astrocyte at the ratio of 1 to 3 stained with β-galactosidase after 4DIV. Scale bar = 400 µm.

As mentioned above, GFAP stains both glioma and primary astrocytes. However, β-galactosidase as a colorimetric assay quenches the fluorescence of the GFAP. Therefore, a co-culture spheroid of glioblastoma and primary astrocyte stained first with β-galactosidase and secondly with GFAP can still present the two cell types under

fluorescent microscopy, as shown in **Figure 6.5,** with the astrocytes turned green due to GFAP while the glioma remained dark blue due to β-galactosidase staining.

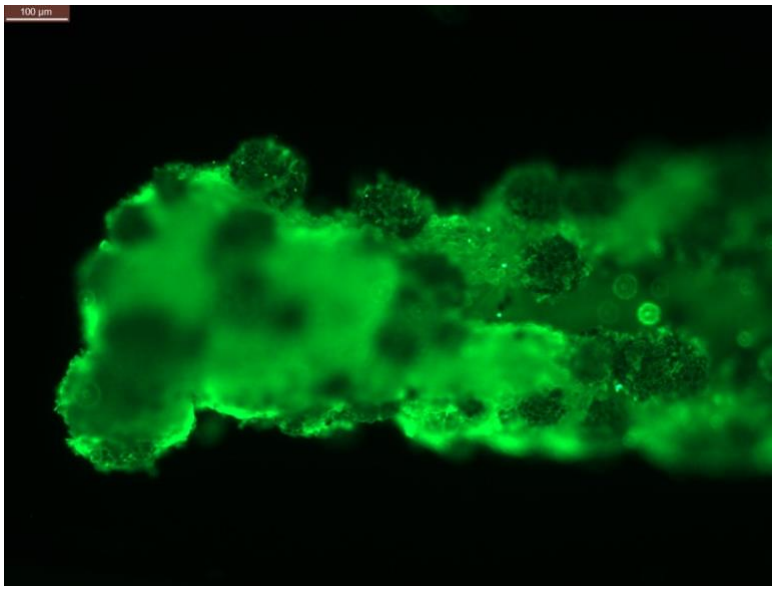

Figure 6.5: Co-culture spheroid of glioblastoma and primary astrocyte at the ratio of 1 to 1 4DIV stained with GFAP. Scale bar = 100 µm.

Co-culture spheroid models with different ratios of brain tumor vs. astrocytes cells were investigated as shown in **Figure 6.6**. Spheroids were stained with β-galactosidase and analyzed using Image Pro Plus 7.0 software to study tumor invasion in co-culture.

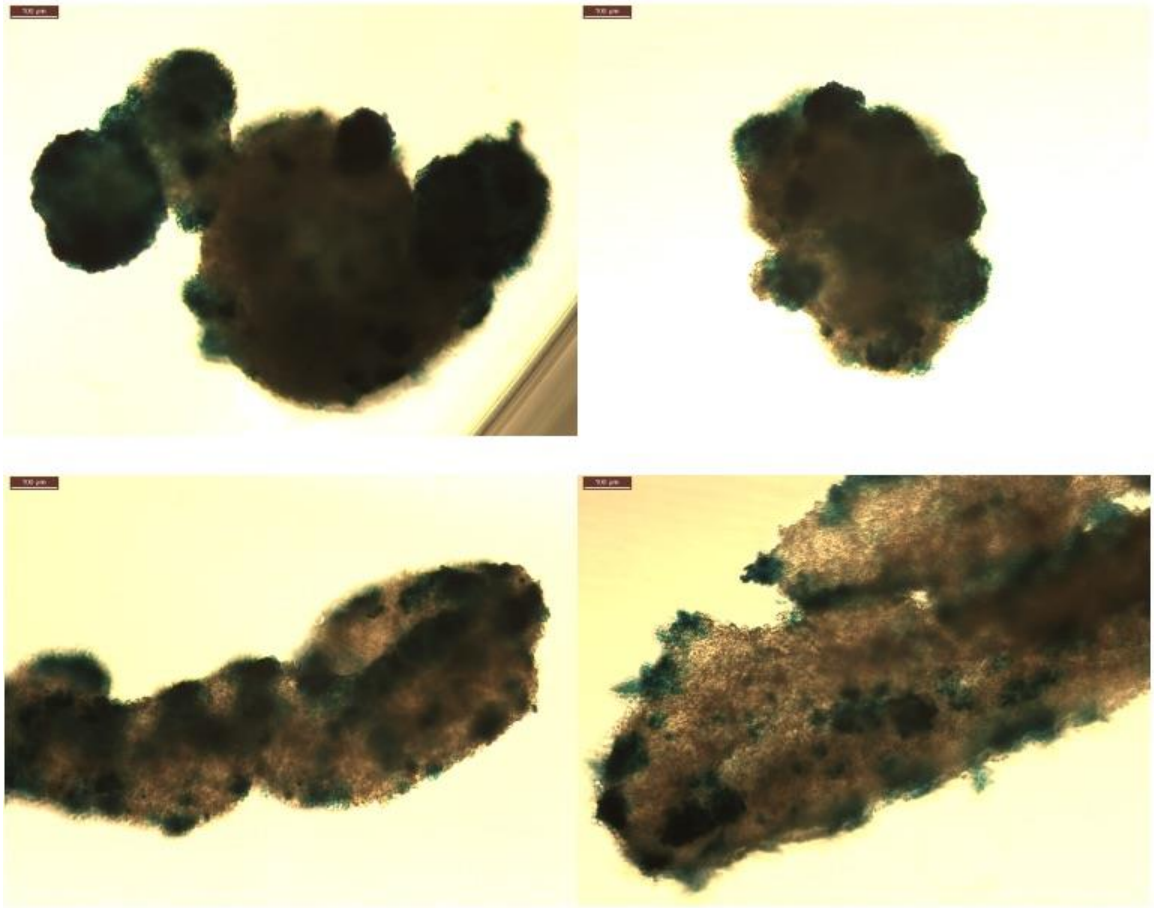

Figure 6.6: Co-culture spheroid with different ratio of brain tumor vs. astrocytes cells (1 to 1, 1 to 2, 1 to 3 and 1 to 4, respectively) stained with β-galactosidase. Pictures were taken 5 DIV after placing the cells into culture conditions. Scale bar = 100 µm.

Total area coverage by β-gal staining of co-culture spheroid models, which is an indication of glioma cells is shown in **Figure 6.7**.

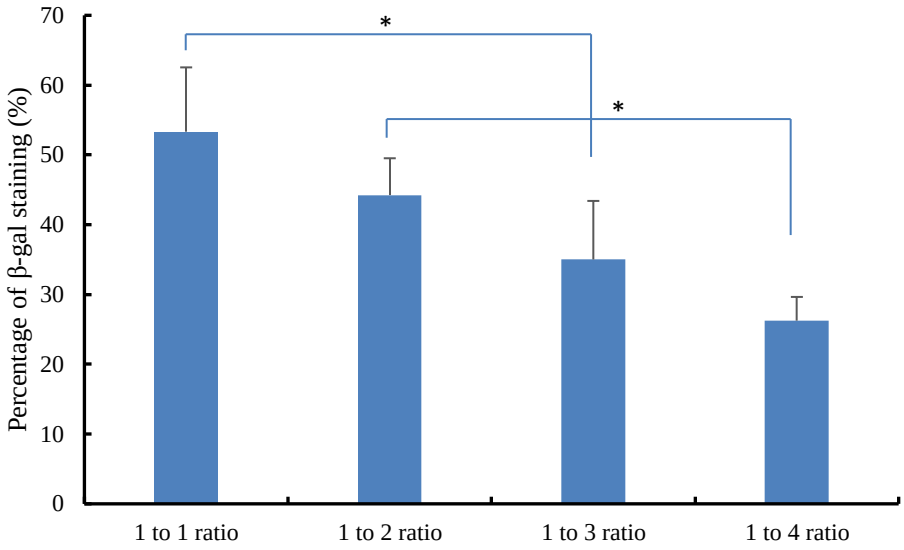

Figure 6.7: Percentage of brain tumor cells in co-culture spheroid with different ratios of normal brain cells astrocytes and brain tumor cells, 1 to 1, 1 to 2, 1 to 3 and 1 to 4, respectively. n =4 for each ratio, error bars represent standard deviation. Significant difference denoted by * for $p \leq 0.05$. $F_{3,12} = 11.21$, p-value = 0.000855.

6.4 Discussion

We successfully demonstrated integration of two different cell types into a co-culture environment at both 2D and 3D models with different ratios of gliomas and primary astrocytes. Due to their aggressive growth rate, glioma cells could invade and take over the culture in a short amount of time in 2D model. Therefore, a 3D co-culture spheroid may be a better model for long term investigation of role of cell–cell physical contact, autocrine and paracrine effects on cell functions as well as cell differentiation [102], [103]. Co-culture spheroids with different ratios of glioma and primary astrocytes could be used to study different stages of tumorigenesis [104] as well as interaction with materials (e.g. combination of CuHARS and DSF). Moreover, the same method could be used to pair up various cell types (endothelial together with gliomas to study the influence of brain tumor on blood brain barrier [105], [106]) or integration of three or more cell types [107].

CHAPTER 7

CONCLUSIONS

Both two- and three-dimensional cell culture models are used for *in vitro* research, with traditional 2D cell culture used more frequently in cell assay and drug discovery. However, 3D cell spheroid has emerged in recent years to close the gap between *in vitro* and *in vivo* cell models. Each model has its own advantages and disadvantages. Traditional 2D cell culture is a convenient, inexpensive, and quick way to study drug testing but may not provide accurate responses due to cell morphology and cell-cell interaction which are different from *in vivo*. Also, duration of 2D cell models varies and depends on cell types but in most cases does not expand longer than 7 days with majority only last 3 to 5 days. On the other hand, 3D cell models grow cells into aggregates/spheroids with different layers of cells (proliferating layer, quiescent layer and necrotic core) which better resemble 3D environment of the cells in tissue. Moreover, 3D cell models can last up to a month *in vitro* making them more suitable for long-term studies. However, 3D models require longer preparation time, larger numbers of cells, and more drugs/chemicals. Analyzing 3D spheroid data also proves to be challenging.

In this dissertation, we validated the similarity and difference between 2D and 3D cell models in terms of cell morphology as well as their interactions with various materials. The results demonstrated that while there were similarities in the ways cells interact and respond to materials and drugs, 2D models were more suitable in situations

where fast screening for materials/drugs response was desired or for preliminary experiments, whereas 3D models better fit situations where long-term cell-cell and cell-materials interactions were the focus, especially in cases of cancerous cells which had distinctive feature of aggressive proliferation. Furthermore, we demonstrated the ability to grow different cell types (normal astrocytes and glioma) in a co-culture environment to more accurately mimic the brain tumor microenvironment.

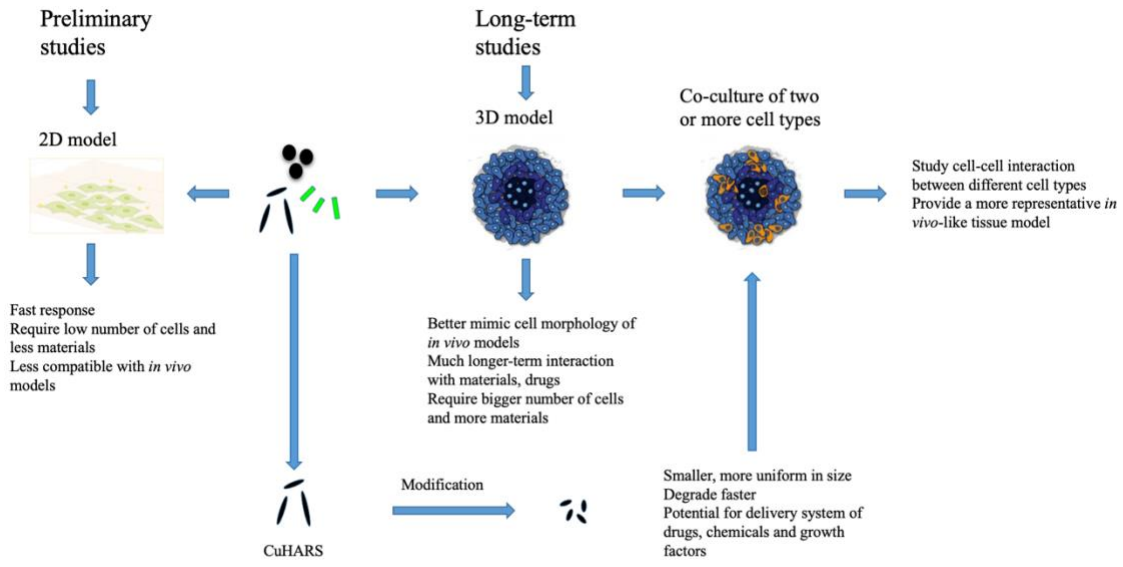

Figure 7.1: Schematic diagram comparing two-and three-dimensional cell models (adapted from [88]).

The novel material CuHARS developed by our group which is made from copper and the amino acid cystine has promising potential to be used as a carrier in a delivery system because it has many unique characteristics, including biodegradable behaviors in body physiological conditions, less toxicity to the cells compared to copper at the same concentration, and enhanced suppression of glioma when used in combination with DSF exploiting the very low aggregation property of the CuHARS. Moreover, we established

a method to modify the CuHARS to get a more uniform size and shape of material for better carrier properties and interaction with cells. Future studies include coating the CuHARS with various cancer drugs and growth factors (we have had some preliminary results in the lab with fluorescent bead labeled CuHARS) and testing these materials in co-culture systems.

APPENDIX A

CELL CULTURE MEDIA

A.1 CRL-2303 Media

A.1.1 Materials Required for 250 mL Media

- Sterile filtration unit
- 221.25 mL Dulbecco's Modified Eagle's Medium (DMEM)
- 25 mL Fetal Bovine Serum (FBS) (10 %)
- 2.5 mL Amino acid solution (1 %)
- 1.25 mL Penicillin/Streptomycin solution (P/S) (0.5 %)

A.1.2 Preparation of CRL-2303 Growth Media

The procedure is carried out in a laminar flow hood (sterile environment).

1. Add 110.25 mL DMEM to sterile filtration unit.
2. Add Fetal Bovine Serum, Amino acid solution, and P/S to sterile filtration unit.
3. Add 111 mL DMEM to sterile filtration unit.
4. Place the lid over sterile filtration unit and connect it to vacuum nozzle.
5. Carefully turn on the vacuum and allow the liquid to pass through the filter. Make sure to hold sterile filtration unit during this step so the unit does not turn over. Turn off the vacuum before bubbles form.
6. Twist top of filtration unit off carefully. Screw sterile cap onto container of media.

7. Label media as CRL-2303 media with date and your initials, and store in refrigerator.

A.2 Astrocyte Media

A.2.1 Materials Required for 250 mL Media

- Sterile filtration unit
- 223.75 mL Ham's F-12K media with L-Glutamine
- 12.5 mL Fetal Bovine Serum (FBS) (5.0 %)
- 12.5 mL Horse Serum (5.0 %)
- 1.25 mL Penicillin/Streptomycin solution (P/S) (0.5 %)

A.2.2 Preparation of Astrocyte Growth Media

The procedure is carried out in a laminar flow hood (sterile environment).

1. Add 100 mL Ham's F-12K media to sterile filtration unit.
2. Add Fetal Bovine Serum, Horse Serum, and P/S to sterile filtration unit.
3. Add 123.75 mL Ham's F-12K media to sterile filtration unit.
4. Place the lid over sterile filtration unit and connect it to vacuum nozzle.
5. Carefully turn on the vacuum and allow the liquid to pass through the filter. Make sure to hold sterile filtration unit during this step so the unit does not turn over. Turn off the vacuum before bubbles form.
6. Twist top of filtration unit off carefully. Screw sterile cap onto container of media.
7. Label media as Astrocyte media with date and your initials, and store in refrigerator.

A.3 Locke's Solution

A.3.1 Materials Required for 250 mL Media

- 2250 mg of Sodium Chloride (NaCl) (154 mM)
- 104.4 mg of Potassium Chloride (Kcl) (5.6 mM)
- 75.6 mg of Sodium Bicarbonate (NaHCO3) (3.6 mM)
- 84.5 mg of Calcium Chloride (Cacl2.2H2O) (2.3 mM)
- 252.3 mg of Glucose (5.6 mM)
- 1.25 ml of 1M stock 4-(2-hydroxyethyle)-2-piperazineethanesulfonic acid (HEPES) (pH 7.4) (5 mM)
- 248.75 mL purified water

A.3.2 Preparation of Locke's Solution

1. Dissolve the components in 100 ml of purified water and add to the vacuum filtration unit.
2. Add 100 ml of purified water to vacuum filtration unit.
3. Add water with dissolved components.
4. Add 1.25 ml of 1 M stock HEPES.
5. Add remaining amount of purified water.
6. Place cap on unit. Carefully turn on the vacuum.
7. Allow all the liquid to pass through the filter. Turn off the vacuum before bubbles form.
8. Twist the top of vacuum unit off carefully. Screw the sterile cap onto the container of the solution.
9. Label as Locke's solution with date and your initials, and store in refrigerator.

APPENDIX B

SPLITTING AND FREEZING CELLS

B.1 Splitting Cells or Re-Plating Cells

1. Remove media from cells into a waste beaker.
2. Wash flask once with 3 ml of 1X PBS (1 mL 10X PBS + 9 mL sterile water gives 10 mL 1X PBS). Pipet PBS gently into a flask. Lay flask down once. Lift flask and remove PBS.
3. Add 1.5 mL (for CRL-2303 and Microglia) or 3 mL (for Astrocytes) thawed trypsin/EDTA to flask. Cap the flask and put it in the incubator for 3 minutes (for CRL-2303 and Microglia) or 8 minutes (for Astrocytes). Take the flask out of the incubator and check under microscope to ensure cells are detached.
4. Add 3 mL fresh media to the flask and transfer them to a 15 mL centrifuge tube.
5. Centrifuge cells in a tube using a counterbalance in pre-cooled centrifuge (8°C) at 160 r.c.f. (relative centrifugal force) for 8 minutes.
6. After spinning, remove the supernatant liquid into waste beaker.
7. Suspend pellet in desired amount of media, then vortex until cells are evenly distributed throughout media.
8. Before plating, count the number of cells using a hemocytometer.
9. Plate cells onto the flask, adding the appropriate amounts of media.

10. Label flask with cell name, date, and passage number (passage number increases after splitting cells).

B.2 Freezing Cells

1. Remove media from cells into a waste beaker.
2. Wash flask once with 3 mL of 1X PBS (1 mL 10X PBS + 9 mL sterile water gives 10 mL 1X PBS). Pipet PBS gently into a flask. Lay flask down once. Lift flask and remove PBS.
3. Add 1.5 mL (for CRL-2303 and Microglia) or 3 mL (for Astrocytes) thawed trypsin/EDTA to flask. Cap the flask and put it in the incubator for 3 minutes (for CRL-2303 and Microglia) or 8 minutes (for Astrocytes). Take the flask out of the incubator and check under microscope to ensure cells are detached.
4. Add 3 mL fresh media to the flask and transfer them to a 15 mL centrifuge tube.
5. Centrifuge cells in a tube using a counterbalance in pre-cooled centrifuge (8°C) at 160 r.c.f. (relative centrifugal force) for 8 minutes.
6. After spinning, remove the supernatant liquid into waste beaker.
7. Suspend pellet in desired amount of media, then vortex until cells are evenly distributed throughout media.
8. Add 5% DMSO dropwise to cells. Mix by inverting centrifuge tube.
9. Transfer cell mixture to pre-cooled cryovial.
10. Label cryovial with cell name, date, and passage number (passage number is same as on the flask).
11. Put cryovials in a container and place in -80°C freezer overnight.
12. Transfer cells into liquid nitrogen. Record the cane number.

APPENDIX C

THAWING AND FEEDING CELLS

C.1 Thawing Cells

1. Remove vial of cells from liquid nitrogen and immediately place in water bath preheated to 37°C.
2. Thaw the vial containing cells quickly (approximately three minutes).
3. Remove the vial, wipe the vial with kim wipe and isopropanol under the laminar flow hood.
4. Mix cell suspension by pipetting up and down the vial. Do not vortex cells.
5. Gently transfer the cell suspension from the vial into a flask with 5 mL pre-warmed cell growth media.
6. Label flask with cell type, date, and passage number (passage number increases when thawing cells).
7. Incubate the cells for 24 hr at 37°C in 5% CO_2 incubator.
8. Do not use the cells immediately after thawing as it contains Dimethyl Sulfoxide (DMSO) and some dead cells. Passage them at least once before seeding the cells.

C.2 Feeding Cells

1. Remove 3 mL media from 24 cm^2 flask into a waste beaker.
2. Add 3 mL pre-warmed cell culture media to cells.
3. Label flask with date of feeding and place the flask back into the incubator.

APPENDIX D

FIXING CELLS

Protocol for fixation is explained in following steps:

1. Remove complete media from cell culture.
2. Wash the cells with pre-warmed Locke's solution.
3. Add the fixing solution (DiffQuik from Siemens) to cover whole surface of well or dish and leave it for 10 minutes.
4. Remove the fixing solution and add Phosphate Buffer Saline (PBS) to cover whole surface.
5. For storage, label the plate or dish, seal with parafilm and keep it at 2-8°C (in refrigerator).

APPENDIX E

DAPI STAINING PROTOCOL

1. A 14.27 millimolar concentration of DAPI in DI water was diluted 1 to 1000 in 1x PBS.
2. Once DAPI has been added place dish in 37ºC incubator for 10 minutes (depending on the health of the cells you may need a longer time to load do to the fact that healthy cells take longer to load DAPI than damaged or dead cells).

APPENDIX F

MTT ASSAY PROTOCOL

400 uL of MTT solution is added into each well of a 24 well plate. Considering this, 9.6 mL of MTT would be needed to treat an entire plate. Usually 11 mL of solution is prepared to have a buffer volume.

Procedure for a 24 well plate:

1. Weigh 13.75 mg of MTT powder and add it to 11 mL of prewarmed DMEM without phenol red (or sterile Locke's solution).
2. Media is aspirated from the wells carefully. Do not wash.
3. Add 400 uL of MTT solution carefully to each well from the side.
4. Place the 24 well plate in the incubator for 60 minutes to allow the cells to react with MTT solution.
5. The viable cells react, and purple crystals are formed in the wells.
6. After incubation, aspirate the MTT solution carefully without lifting the crystals and add 300 uL of 91% isopropanol to each well.
7. Allow the crystals to be dissolved into the isopropanol, gently shake the well plate. Don't delay after adding the isopropanol as it will evaporate.
8. Transfer 300 uL of isopropanol with dissolved crystals into 96 well plate.
9. Measure the plate using a spectrophotometer at a wavelength of 570 nm.

APPENDIX G

GFAP ANTIBODY (AB) STAINING

1. Fixation of Cells:
    - Remove complete media from cell culture.
    - Wash twice the cells with pre-warmed Locke's solution.
    - Add ice-cold methanol to cover whole surface of well or dish and keep it for 5 minutes.
    - Remove methanol and add 1X PBS to cover whole surface.
    - For storage seal the plate or dish with paraffin and keep it at 2-8 ºC (in refrigerator).
2. Permeabilization of cells: Remove PBS from pre-fixed cells and 0.2 % Triton X 100 (in 1X PBS) to cover whole surface and keep it at room temperature for 15 minutes.
3. Blocking: Remove Triton X 100 and add 2% Goat Serum (in 1X PBS) to cover whole surface. Seal the plate or dish with paraffin and keep it at 2-8 ºC (in refrigerator) for 4-5 hrs or overnight.
4. Primary Ab: Remove goat serum and add 1° Ab (Anti-GFAP produced in rabbit in 1:500 1X PBS) to cover the whole surface. Seal the plate or dish with paraffin and keep it at 2-8 ºC (in refrigerator) for 24 hrs or overnight.
5. Washing: Remove 1° Ab and wash twice with 1X PBS.

6. Secondary Ab: Add 2° Ab (1:500 Goat Anti- Rabbit Ig Ab in 2% Goat Serum which is in 1X PBS) to cover the whole surface. Seal the plate or dish with paraffin and cover with aluminum foil and keep it at room temperature for 45-60 minutes.
7. Washing: Remove 2° Ab and wash twice with 0.2 % Triton X 100 (in 1X PBS). Lastly add 1X PBS to cover whole surface.
8. Florescence Microscopy: Observe staining using fluorescent microscope.
9. Storage: Seal the plate or dish with paraffin and cover with aluminum foil and keep it at 2-8 ºC (in refrigerator) for storage for weeks.

APPENDIX H

B-GALACTOSIDASE STAINING

H.1 Reagents Required for Staining

- 10X PBS

  70.2 mM Na_2HPO_4, 14.7 mM KH_2PO_4, 1.37 M NaCl, and 26.8 mM KCl

- 10X Fixation Buffer

  20% formaldehyde and 2% glutaraldehyde in 10X PBS

- Reagent A - 200 mM $MgCl_2$
- Reagent B - 400 mM potassium ferricyanide
- Reagent C - 400 mM potassium ferrocyanide
- X-Gal - (5-Bromo-4-chloro-3-indolyl-B-D-galactopyranoside)
- Dimethylformamide (DMF)

H.2 Preparation Instructions

- Dilute 10X PBS 10-fold with sterile water to prepare 1X PBS.
- Dilute 10X Fixation Buffer 10-fold with sterile water to prepare 1X Fixation Solution.
- Prepare a 20 mg/mL solution of X-Gal in DMF in a polypropylene tube or a glass vial. The solution can be stored in the dark at -20°C for 1 month.

H.3 Procedure for 48-well Cell Culture Plate

1. Aspirate the growth medium from the cells.

2. Wash cells twice with 300 uL of 1X PBS. Remove the wash solution entirely with aspiration.
3. Add 300 uL of 1X Fixation Solution and incubate 10 minutes at room temperature.
4. During the fixation process, prepare the Staining Solution in a polypropylene tube.

   Staining Solution

Component	Amount
Reagent A	10 uL
Reagent B	10 uL
Reagent C	10 uL
X-Gal solution (20 mg/mL)	50 uL
1X PBS	920 uL
Total volume	1 mL (enough for 3 wells)

5. Rinse the cells twice with 300 uL of 1X PBS.
6. Add 300 uL of Staining Solution to the plate. Ensure even coverage of the plate.
7. Incubate at 37°C for 0.5-2 hr or longer, until the cells stain blue. In the event a longer staining period is needed, seal the plate with parafilm to prevent it from drying out. The exact incubation time must be optimized.
8. Observe the cells under the microscope. Count the cells and calculate the percent of cells.
9. For long-term storage of stained plate, remove the Staining Solution, overlay cells with 300 uL 1X PBS and store at 4°C.

APPENDIX I

RESAZURIN ASSAY PROTOCOL

Spheroid was moved from original plate to a 96 well-plate in 150 µl media. Each well with spheroid will be added 50 µl of resazurin solution. For an experiment with 10 spheroids, follow these steps.

I.1 Prepare Resazurin Solution

1. Prepare the resazurin solution:
    - Weigh 0.4mg of resazurin sodium salt and put in a clean 15ml tube.
    - Add 2ml of sterile PBS 1x to get a concentration of 0.2mg/ml resazurin solution.
2. Procedure for adding resazurin to the cells:
    - Add 50 µl of resazurin solution to each well and mix using pipette.
    - Incubate for at least 4 hours but less than 8 hours in an incubator with 5% CO_2 and at 37°C.
3. Procedure for viability reading:
4. Cover the plate with tin foil and bring it to a fluorescence reader (Gen5 Biotek Fluorescence Plate Reader).

I.2 Measure Viability Using BioTek FLx800 Plate Reader

1. Turn on the plate reader. Power button located on back bottom right side of the device.
2. Check computer connection/communication with device.
3. Turn on laptop.
4. Double click on application icon Gen5 1.08 located on the desktop
5. "Create a New Item"→ "Protocol"
    a. Double click on "Procedure" on left menu.
        i. "Plate type"→ "96 Well Plate"
        ii. Under the "Add Step" menu on left choose: "Read"
            1. "Detection Method"→ "Fluorescence"
            2. "Filter Sets" → "Excite" → "485/20"
                → " Emission" → "528/20" (These numbers depend on the type of fluorescent molecules you are using. Shown for Green.)
                → "Optics Position" → "Top" or "Bottom"
                → "Sensitivity" → 35 or 40 (Higher # = Higher sens)
                → Click on "Full Plate" located on upper right of panel

Uncheck "Use all Wells" → Highlight wells you want to read → Click "Ok" on this screen

→ Click "Ok" on entire panel

Go to File → Save As → Local Drive → Choose appropriate file. Be sure to name the file in a useful manner).

APPENDIX J

IMAGE-PRO PLUS VERSION 7.0

1. Insert the dongle (special security plug) that comes with Image-Pro Plus to unlock the program.

2. Open Image-Pro Plus 7.0. A dialog box 'Macro Browser' appears. Click Done.

3. Go to File → Open → Select the image.

4. Go to Measure → Count/Size → Choose 'Manual' → Click 'Select Colors' → A dialog box appears. Click 'Color Cube Based' → Select Class '1' → Under Options, Select Sensitivity '4' → Pick 'color picker tool'. Then click on the indigo blue color staining (Start selecting the color from lightest to darkest) → Under Preview, select 'Current Class' → Change to 'Class Color on Black' from 'Class Color on Transparent' → Select 'Apply Mask' → Click 'OK'.

5. Now choose 'Automatic Bright Objects'→ Click 'Count'. The white area gets selected.

6. Go to 'Measure' → Click 'Select Measurements' → Choose 'Area' → Click 'Measure'.

7. Go to 'View' → Click 'Measurement Data' → Choose 'Sort Down'.

8. Go to 'File' → Click 'Export Data'. This will copy the data into an excel spreadsheet.

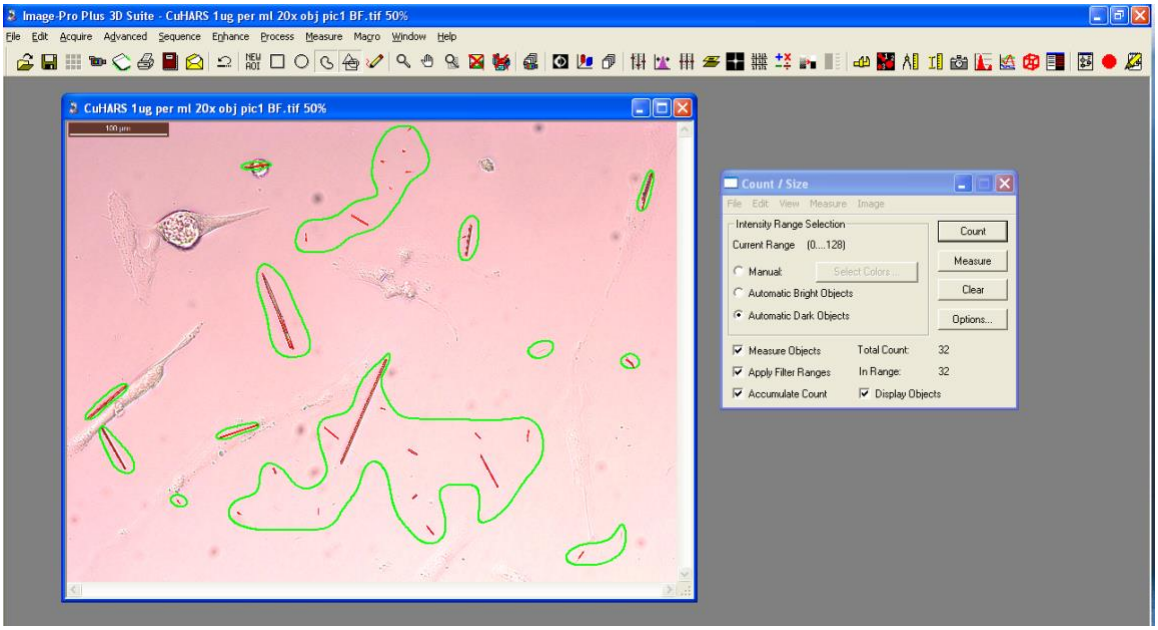

Figure J.1: An example of image analysis to calculate area and length of the CuHARS in 2D cell culture.

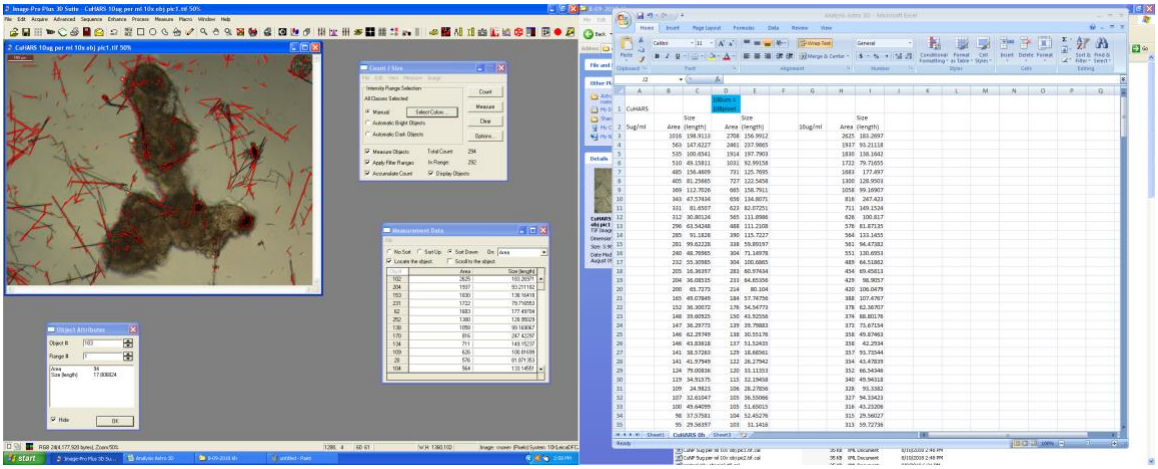

Figure J.2: An example of image analysis to calculate area and length of the CuHARS in 3D cell culture.

BIBLIOGRAPHY

[1] E. C. Holland, "Glioblastoma multiforme: the terminator," *Proceedings of the National Academy of Sciences of the United States of America*, vol. 97, no. 12, pp. 6242–6244, Jun. 2000.

[2] D. R. Johnson and B. P. O'Neill, "Glioblastoma survival in the United States before and during the temozolomide era," *Journal of Neuro-Oncology*, vol. 107, no. 2, pp. 359–364, Apr. 2012.

[3] H. P. Ellis, M. Greenslade, B. Powell, I. Spiteri, A. Sottoriva, and K. M. Kurian, "Current Challenges in Glioblastoma: Intratumour Heterogeneity, Residual Disease, and Models to Predict Disease Recurrence," *Frontiers in Oncology*, vol. 5, Nov. 2015.

[4] J. D. Lathia, S. C. Mack, E. E. Mulkearns-Hubert, C. L. L. Valentim, and J. N. Rich, "Cancer stem cells in glioblastoma," *Genes & Development*, vol. 29, no. 12, pp. 1203–1217, Jun. 2015.

[5] J. Zhou, K.-B. Atsina, B. T. Himes, G. W. Strohbehn, and W. M. Saltzman, "Novel delivery strategies for glioblastoma," *Cancer Journal*, vol. 18, no. 1, pp. 89–99, Feb. 2012.

[6] R. Edmondson, J. J. Broglie, A. F. Adcock, and L. Yang, "Three-dimensional cell culture systems and their applications in drug discovery and cell-based biosensors," *ASSAY and Drug Development Technologies*, vol. 12, no. 4, pp. 207–218, May 2014.

[7] "5 Reasons Cancer Researchers Adopt 3D Cell Culture: A Review of Recent Literature," *Sigma-Aldrich*. [Online]. Available: https://www.sigmaaldrich.com/technical-documents/articles/biology/5-reasons-cancer-researchers-adopt-3d-cell-culture-white-paper.html. [Accessed: 25-Aug-2018].

[8] S. Nath and G. R. Devi, "Three-dimensional culture systems in cancer research: Focus on tumor spheroid model," *Pharmacology & Therapeutics*, vol. 163, pp. 94–108, 2016.

[9] S. Deodhar, J. Huckaby, M. Delahoussaye, and M. A. DeCoster, "High-Aspect Ratio Bio-Metallic Nanocomposites for Cellular Interactions," *IOP Conference Series: Materials Science and Engineering*, vol. 64, no. 1, p. 012014, 2014.

[10] K. C. Kelly, J. R. Wasserman, S. Deodhar, J. Huckaby, and M. A. DeCoster, "Generation of Scalable, Metallic High-Aspect Ratio Nanocomposites in a Biological Liquid Medium," *Journal of Visualized Experiments: JoVE*, no. 101, pp. e52901–e52901, Jul. 2015.

[11] M. A. DeCoster, "Novel Scalable Nano-and Micro-High-Aspect Ratio Structure (HARS) Biocomposites Generated under Physiological Conditions," in *2016 32nd Southern Biomedical Engineering Conference (SBEC)*, 2016, pp. 165–166.

[12] G. D. Prestwich and Y. Luo, "Novel biomaterials for drug delivery," *Expert Opinion on Therapeutic Patents*, vol. 11, no. 9, pp. 1395–1410, Sep. 2001.

[13] P. H. Hoet, I. Brüske-Hohlfeld, and O. V. Salata, "Nanoparticles – known and unknown health risks," *Journal of Nanobiotechnology*, vol. 2, no. 1, p. 12, Dec. 2004.

[14] A. Karan, M. Darder, U. Kansakar, Z. Norcross, and M. A. DeCoster, "Integration of a Copper-Containing Biohybrid (CuHARS) with Cellulose for Subsequent Degradation and Biomedical Control," *International Journal of Environmental Research and Public Health*, vol. 15, no. 5, May 2018.

[15] J. Triscott *et al.*, "Disulfiram, a drug widely used to control alcoholism, suppresses the self-renewal of glioblastoma and over-rides resistance to temozolomide," *Oncotarget*, vol. 3, no. 10, pp. 1112–1123, Oct. 2012.

[16] M. Wehbe *et al.*, "Development and optimization of an injectable formulation of copper diethyldithiocarbamate, an active anticancer agent," *International Journal of Nanomedicine*, vol. 12, pp. 4129–4146, May 2017.

[17] X. Lun *et al.*, "Disulfiram when Combined with Copper Enhances the Therapeutic Effects of Temozolomide for the Treatment of Glioblastoma," *Clinical Cancer Research*, vol. 22, no. 15, pp. 3860–3875, Aug. 2016.

[18] M. V. Sofroniew and H. V. Vinters, "Astrocytes: biology and pathology," *Acta Neuropathologica*, vol. 119, no. 1, pp. 7–35, Jan. 2010.

[19] "Guyton and Hall Textbook of Medical Physiology - 12th Edition." [Online]. Available: https://www.elsevier.com/books/guyton-and-hall-textbook-of-medical-physiology/hall/978-0-8089-2400-5. [Accessed: 09-Nov-2018].

[20] H. K. Kimelberg and M. Nedergaard, "Functions of astrocytes and their potential as therapeutic targets," *Neurotherapeutics*, vol. 7, no. 4, pp. 338–353, Oct. 2010.

[21] E. Shigetomi, D. N. Bowser, M. V. Sofroniew, and B. S. Khakh, "Two forms of astrocyte calcium excitability have distinct effects on NMDA receptor-mediated slow inward currents in pyramidal neurons," *Journal of Neuroscience*, vol. 28, no. 26, pp. 6659–6663, Jun. 2008.

[22] M. Brini, T. Calì, D. Ottolini, and E. Carafoli, “Neuronal calcium signaling: function and dysfunction,” *Cellular and Molecular Life Sciences*, vol. 71, no. 15, pp. 2787–2814, Aug. 2014.

[23] M. M. Halassa, T. Fellin, and P. G. Haydon, “The tripartite synapse: roles for gliotransmission in health and disease,” *Trends in Molecular Medicine*, vol. 13, no. 2, pp. 54–63, Feb. 2007.

[24] M. Nedergaard, B. Ransom, and S. A. Goldman, “New roles for astrocytes: redefining the functional architecture of the brain,” *Trends in Neurosciences*, vol. 26, no. 10, pp. 523–530, Oct. 2003.

[25] G. Perea, M. Navarrete, and A. Araque, “Tripartite synapses: astrocytes process and control synaptic information,” *Trends in Neurosciences*, vol. 32, no. 8, pp. 421–431, Aug. 2009.

[26] G. Ricci, L. Volpi, L. Pasquali, L. Petrozzi, and G. Siciliano, “Astrocyte–neuron interactions in neurological disorders,” *Journal of Biological Physics*, vol. 35, no. 4, pp. 317–336, Oct. 2009.

[27] F. Kirchhoff, R. Dringen, and C. Giaume, “Pathways of neuron-astrocyte interactions and their possible role in neuroprotection,” *European Archives of Psychiatry and Clinical Neuroscience*, vol. 251, no. 4, pp. 159–169, Aug. 2001.

[28] N. J. Abbott, “Astrocyte-endothelial interactions and blood-brain barrier permeability,” *Journal of Anatomy*, vol. 200, no. 6, pp. 629–638, Jun. 2002.

[29] R. Daneman and A. Prat, “The Blood–Brain Barrier,” *Cold Spring Harbor Perspectives in Biology*, vol. 7, no. 1, Jan. 2015.

[30] G. J. del Zoppo and J. M. Hallenbeck, “Advances in the vascular pathophysiology of ischemic stroke,” *Thrombosis Research*, vol. 98, no. 3, pp. 73–81, May 2000.

[31] K. Nakahama, M. Nagano, A. Fujioka, K. Shinoda, and H. Sasaki, “Effect of TPA on aquaporin 4 mRNA expression in cultured rat astrocytes,” *Glia*, vol. 25, no. 3, pp. 240–246, Feb. 1999.

[32] E. Hansson and L. Rönnbäck, “Glial neuronal signaling in the central nervous system,” *FASEB Journal*, vol. 17, no. 3, pp. 341–348, Mar. 2003.

[33] “Key Statistics for Brain and Spinal Cord Tumors.” [Online]. Available: https://www.cancer.org/cancer/brain-spinal-cord-tumors-adults/about/key-statistics.html. [Accessed: 23-Feb-2019].

[34] L. Nayak, E. Q. Lee, and P. Y. Wen, “Epidemiology of brain metastases,” *Current Oncology Reports*, vol. 14, no. 1, pp. 48–54, Feb. 2012.

[35] D. B. Costa *et al.*, "Clinical Experience with Crizotinib in Patients with Advanced ALK-Rearranged Non-Small-Cell Lung Cancer and Brain Metastases," *Journal of Clinical Oncology*, vol. 33, no. 17, pp. 1881–1888, Jun. 2015.

[36] R. L. Siegel, K. D. Miller, and A. Jemal, "Cancer statistics, 2016," *CA: A Cancer Journal for Clinicians*, vol. 66, no. 1, pp. 7–30, Jan. 2016.

[37] R. Leece, J. Xu, Q. T. Ostrom, Y. Chen, C. Kruchko, and J. S. Barnholtz-Sloan, "Global incidence of malignant brain and other central nervous system tumors by histology, 2003–2007," *Neuro-Oncology*, vol. 19, no. 11, pp. 1553–1564, Oct. 2017.

[38] P. A. McKinney, "Brain tumours: incidence, survival, and aetiology," *Journal of Neurology, Neurosurgery & Psychiatry*, vol. 75, no. suppl 2, pp. ii12–ii17, Jun. 2004.

[39] F. B. Furnari *et al.*, "Malignant astrocytic glioma: genetics, biology, and paths to treatment," *Genes & Development*, vol. 21, no. 21, pp. 2683–2710, Nov. 2007.

[40] P. Wesseling, J. M. Kros, and J. W. M. Jeuken, "The pathological diagnosis of diffuse gliomas: towards a smart synthesis of microscopic and molecular information in a multidisciplinary context," *Diagnostic Histopathology*, vol. 17, no. 11, pp. 486–494, Nov. 2011.

[41] J. Huang, B. Gholami, N. Y. R. Agar, I. Norton, W. M. Haddad, and A. R. Tannenbaum, "Classification of Astrocytomas and Oligodendrogliomas from Mass Spectrometry Data Using Sparse Kernel Machines," *Conference Proceedings IEEE Engineering in Medicine and Biology Society*, vol. 2011, pp. 7965–7968, 2011.

[42] H. Zong, L. F. Parada, and S. J. Baker, "Cell of Origin for Malignant Gliomas and Its Implication in Therapeutic Development," *Cold Spring Harbor Perspectives in Biology*, vol. 7, no. 5, May 2015.

[43] S. Edge, D. R. Byrd, C. C. Compton, A. G. Fritz, F. Greene, and A. Trotti, Eds., *AJCC Cancer Staging Handbook: From the AJCC Cancer Staging Manual*, 7th ed. New York: Springer-Verlag, 2010.

[44] "Survival statistics for brain and spinal cord tumours - Canadian Cance," *www.cancer.ca*. [Online]. Available: http://www.cancer.ca/en/cancer-information/cancer-type/brain-spinal/prognosis-and-survival/survival-statistics/?region=on. [Accessed: 12-Nov-2018].

[45] "Survival Rates for Selected Adult Brain and Spinal Cord Tumors." [Online]. Available: https://www.cancer.org/cancer/brain-spinal-cord-tumors-adults/detection-diagnosis-staging/survival-rates.html. [Accessed: 12-Nov-2018].

[46] D. N. Louis *et al.*, "The 2007 WHO Classification of Tumours of the Central Nervous System," *Acta Neuropathologica*, vol. 114, no. 2, pp. 97–109, Aug. 2007.

[47] M. S. Walid, “Prognostic Factors for Long-Term Survival after Glioblastoma,” *The Permanente Journal*, vol. 12, no. 4, pp. 45–48, 2008.

[48] J. K. Park *et al.*, “Scale to Predict Survival After Surgery for Recurrent Glioblastoma Multiforme,” *Journal of Clinical Oncology*, vol. 28, no. 24, pp. 3838–3843, Aug. 2010.

[49] S. Mallick, R. Benson, A. Hakim, and G. K. Rath, “Management of glioblastoma after recurrence: A changing paradigm,” *Journal of the Egyptian National Cancer Institute*, vol. 28, no. 4, pp. 199–210, Dec. 2016.

[50] Ö. Yersal, “Clinical outcome of patients with glioblastoma multiforme: Single center experience,” *Journal of Oncological Sciences*, vol. 3, no. 3, pp. 123–126, Dec. 2017.

[51] F. W. Boele, A. G. Rooney, R. Grant, and M. Klein, “Psychiatric symptoms in glioma patients: from diagnosis to management,” *Neuropsychiatric Disease and Treatment*, vol. 11, pp. 1413–1420, Jun. 2015.

[52] R. Henriksson, T. Asklund, and H. S. Poulsen, “Impact of therapy on quality of life, neurocognitive function and their correlates in glioblastoma multiforme: a review,” *Journal of Neuro-Oncology*, vol. 104, no. 3, pp. 639–646, Sep. 2011.

[53] “Brain Tumor - Grades and Prognostic Factors,” *Cancer.Net*, 25-Jun-2012. [Online]. Available: https://www.cancer.net/cancer-types/brain-tumor/grades-and-prognostic-factors. [Accessed: 12-Nov-2018].

[54] “Glioblastoma (GBM),” *American Brain Tumor Association*. [Online]. Available: https://www.abta.org/tumor_types/glioblastoma-gbm/. [Accessed: 13-Nov-2018].

[55] H. Huang, Y. Ding, X. S. Sun, and T. A. Nguyen, “Peptide hydrogelation and cell encapsulation for 3D culture of MCF-7 breast cancer cells,” *PLoS ONE*, vol. 8, no. 3, p. e59482, 2013.

[56] “3D Cell Culture vs. Traditional 2D Cell Culture | Mimetas.” [Online]. Available: https://mimetas.com/article/3d-cell-culture-vs-traditional-2d-cell-culture. [Accessed: 04-Apr-2019].

[57] qgelbio, *QGel: Why 3D Cell Culture?*

[58] D. Huh, G. A. Hamilton, and D. E. Ingber, “From Three-Dimensional Cell Culture to Organs-on-Chips,” *Trends in Cell Biology*, vol. 21, no. 12, pp. 745–754, Dec. 2011.

[59] M. Ravi, V. Paramesh, S. R. Kaviya, E. Anuradha, and F. D. P. Solomon, “3D cell culture systems: advantages and applications,” *Journal of Cellular Physiology*, vol. 230, no. 1, pp. 16–26, Jan. 2015.

[60] D. J. Maltman and S. A. Przyborski, “Developments in three-dimensional cell culture technology aimed at improving the accuracy of in vitro analyses,” *Biochemical Society Transactions*, vol. 38, no. 4, pp. 1072–1075, Aug. 2010.

[61] “3d Cell Culture: Tools and Techniques,” *Sigma-Aldrich*. [Online]. Available: https://www.sigmaaldrich.com/technical-documents/articles/biology/3d-cell-culture-technology.html. [Accessed: 14-Nov-2018].

[62] S. Bose, M. Roy, and A. Bandyopadhyay, “Recent advances in bone tissue engineering scaffolds,” *Trends in Biotechnology*, vol. 30, no. 10, pp. 546–554, Oct. 2012.

[63] A. Sourla, C. Doillon, and M. Koutsilieris, “Three-dimensional type I collagen gel system containing MG-63 osteoblasts-like cells as a model for studying local bone reaction caused by metastatic cancer cells.,” *Anticancer Research*, vol. 16, no. 5A, pp. 2773–2780, 1996.

[64] “3D cell culture methods and applications - a short review,” *Elveflow*.

[65] S. Breslin and L. O’Driscoll, “Three-dimensional cell culture: the missing link in drug discovery,” *Drug Discovery Today*, vol. 18, no. 5–6, pp. 240–249, Mar. 2013.

[66] C. E. White and R. M. Olabisi, “Scaffolds for retinal pigment epithelial cell transplantation in age-related macular degeneration,” *Journal of Tissue Engineering*, vol. 8, Jul. 2017.

[67] K. E. Kador and J. L. Goldberg, “Scaffolds and stem cells: delivery of cell transplants for retinal degenerations,” *Expert Review of Ophthalmology*, vol. 7, no. 5, pp. 459–470, Oct. 2012.

[68] A. Birgersdotter, R. Sandberg, and I. Ernberg, “Gene expression perturbation in vitro--a growing case for three-dimensional (3D) culture systems,” *Seminars in Cancer Biology*, vol. 15, no. 5, pp. 405–412, Oct. 2005.

[69] R. H. Dosh, A. Essa, N. Jordan-Mahy, C. Sammon, and C. L. Le Maitre, “Use of hydrogel scaffolds to develop an in vitro 3D culture model of human intestinal epithelium,” *Acta Biomaterialia*, vol. 62, pp. 128–143, 15 2017.

[70] J. M. Kelm, N. E. Timmins, C. J. Brown, M. Fussenegger, and L. K. Nielsen, “Method for generation of homogeneous multicellular tumor spheroids applicable to a wide variety of cell types,” *Biotechnology and Bioengineering*, vol. 83, no. 2, pp. 173–180, Jul. 2003.

[71] Y. Li and E. Kumacheva, “Hydrogel microenvironments for cancer spheroid growth and drug screening,” *Science Advances*, vol. 4, no. 4, p. eaas8998, Apr. 2018.

[72] K. Kobayashi *et al.*, "Increased expression of drug-metabolizing enzymes in human hepatocarcinoma FLC-4 cells cultured on micro-space cell culture plates," *Drug Metabolism and Pharmacokinetics*, vol. 27, no. 5, pp. 478–485, 2012.

[73] "3D Cell Culture Guide | Creative Bioarray." [Online]. Available: https://www.creative-bioarray.com/support/3d-cell-culture-guide.htm. [Accessed: 15-Nov-2018].

[74] M. Vinci *et al.*, "Advances in establishment and analysis of three-dimensional tumor spheroid-based functional assays for target validation and drug evaluation," *BMC Biology*, vol. 10, no. 1, p. 29, Mar. 2012.

[75] D. P. Ivanov *et al.*, "Multiplexing spheroid volume, resazurin and acid phosphatase viability assays for high-throughput screening of tumour spheroids and stem cell neurospheres," *PLoS ONE*, vol. 9, no. 8, p. e103817, 2014.

[76] X. (James) Li, A. V. Valadez, P. Zuo, and Z. Nie, "Microfluidic 3D cell culture: potential application for tissue-based bioassays," *Bioanalysis*, vol. 4, no. 12, pp. 1509–1525, Jun. 2012.

[77] D. Pappas, "Microfluidics and cancer analysis: cell separation, cell/tissue culture, cell mechanics, and integrated analysis systems," *Analyst*, vol. 141, no. 2, pp. 525–535, Jan. 2016.

[78] Y.-C. Toh *et al.*, "A novel 3D mammalian cell perfusion-culture system in microfluidic channels," *Lab on a Chip*, vol. 7, no. 3, pp. 302–309, Mar. 2007.

[79] C. Wan, S. Chung, and R. D. Kamm, "Differentiation of embryonic stem cells into cardiomyocytes in a compliant microfluidic system," *Annals of Biomedical Engineering*, vol. 39, no. 6, pp. 1840–1847, Jun. 2011.

[80] T. Liu, B. Lin, and J. Qin, "Carcinoma-associated fibroblasts promoted tumor spheroid invasion on a microfluidic 3D co-culture device," *Lab on a Chip*, vol. 10, no. 13, pp. 1671–1677, Jul. 2010.

[81] G. G. Nestorova, K. Hasenstein, N. Nguyen, M. A. DeCoster, and N. D. Crews, "Lab-on-a-chip mRNA purification and reverse transcription via a solid-phase gene extraction technique," *Lab on a Chip*, vol. 17, no. 6, pp. 1128–1136, 14 2017.

[82] J. Ramyadevi, K. Jeyasubramanian, A. Marikani, G. Rajakumar, and A. A. Rahuman, "Synthesis and antimicrobial activity of copper nanoparticles," *Materials Letters*, vol. 71, pp. 114–116, Mar. 2012.

[83] Y. Yang, Y. Chen, F. Leng, L. Huang, Z. Wang, and W. Tian, "Recent Advances on Surface Modification of Halloysite Nanotubes for Multifunctional Applications," *Applied Sciences*, vol. 7, no. 12, p. 1215, Dec. 2017.

[84] M. Massaro *et al.*, "Chemical modification of halloysite nanotubes for controlled loading and release," *Journal of Materials Chemistry B*, vol. 6, no. 21, pp. 3415–3433, May 2018.

[85] "Halloysite Clay Nanotubes for Loading and Sustained Release of Functional Compounds - Lvov - 2016 - *Advanced Materials* - Wiley Online Library." [Online]. Available: https://onlinelibrary.wiley.com/doi/abs/10.1002/adma.201502341. [Accessed: 05-Apr-2019].

[86] G. Mehta, A. Y. Hsiao, M. Ingram, G. D. Luker, and S. Takayama, "Opportunities and Challenges for use of Tumor Spheroids as Models to Test Drug Delivery and Efficacy," *Journal of Controlled Release*, vol. 164, no. 2, pp. 192–204, Dec. 2012.

[87] M. Zanoni *et al.*, "3D tumor spheroid models for *in vitro* therapeutic screening: a systematic approach to enhance the biological relevance of data obtained," *Scientific Reports*, vol. 6, p. 19103, Jan. 2016.

[88] E. C. Costa, A. F. Moreira, D. de Melo-Diogo, V. M. Gaspar, M. P. Carvalho, and I. J. Correia, "3D tumor spheroids: an overview on the tools and techniques used for their analysis," *Biotechnology Advances*, vol. 34, no. 8, pp. 1427–1441, Dec. 2016.

[89] M. H. Greene, "Is Cisplatin a Human Carcinogen?" *Journal of the National Cancer Institute*, vol. 84, no. 5, pp. 306–312, Mar. 1992.

[90] T. C. Johnstone, G. Y. Park, and S. J. Lippard, "Understanding and Improving Platinum Anticancer Drugs – Phenanthriplatin," *Anticancer Research*, vol. 34, no. 1, pp. 471–476, Jan. 2014.

[91] Y. Wang, X. Kong, Y. Guo, R. Wang, and W. Ma, "Continuous dose-intense temozolomide and cisplatin in recurrent glioblastoma patients," *Medicine (Baltimore)*, vol. 96, no. 10, p. e6261, Mar. 2017.

[92] D. Coluccia *et al.*, "Enhancing glioblastoma treatment using cisplatin-gold-nanoparticle conjugates and targeted delivery with magnetic resonance-guided focused ultrasound," *Nanomedicine*, vol. 14, no. 4, pp. 1137–1148, Feb. 2018.

[93] Y. Xu *et al.*, "The synergic antitumor effects of paclitaxel and temozolomide co-loaded in mPEG-PLGA nanoparticles on glioblastoma cells," *Oncotarget*, vol. 7, no. 15, pp. 20890–20901, Mar. 2016.

[94] T. L. Riss *et al.*, "Cell Viability Assays," in *Assay Guidance Manual*, G. S. Sittampalam, N. P. Coussens, K. Brimacombe, A. Grossman, M. Arkin, D. Auld, C. Austin, J. Baell, B. Bejcek, J. M. M. Caaveiro, T. D. Y. Chung, J. L. Dahlin, V. Devanaryan, T. L. Foley, M. Glicksman, M. D. Hall, J. V. Haas, J. Inglese, P. W. Iversen, S. D. Kahl, S. C. Kales, M. Lal-Nag, Z. Li, J. McGee, O. McManus, T. Riss, O. J. Trask, J. R. Weidner, M. J. Wildey, M. Xia, and X. Xu, Eds. Bethesda (MD): Eli Lilly & Company and the National Center for Advancing Translational Sciences, 2004.

[95] R. Csepregi *et al.*, "Complex Formation of Resorufin and Resazurin with B-Cyclodextrins: Can Cyclodextrins Interfere with a Resazurin Cell Viability Assay?," *Molecules*, vol. 23, no. 2, p. 382, Feb. 2018.

[96] J. L. Chen, T. W. J. Steele, and D. C. Stuckey, "Metabolic reduction of resazurin; location within the cell for cytotoxicity assays," *Biotechnology and Bioengineering*, vol. 115, no. 2, pp. 351–358, 2018.

[97] M. Papaioannou, I. Mylonas, R. E. Kast, and A. Brüning, "Disulfiram/copper causes redox-related proteotoxicity and concomitant heat shock response in ovarian cancer cells that is augmented by auranofin-mediated thioredoxin inhibition," *Oncoscience*, vol. 1, no. 1, pp. 21–29, 2014.

[98] D. R. Bogdanowicz and H. H. Lu, "Studying cell-cell communication in co-culture," *Biotechnology Journal*, vol. 8, no. 4, pp. 395–396, Apr. 2013.

[99] N. Gagliano *et al.*, "Glioma-astrocyte interaction modifies the astrocyte phenotype in a co-culture experimental model," *Oncology Reports*, vol. 22, no. 6, pp. 1349–1356, Dec. 2009.

[100] Y. Jiang and L. Uhrbom, "On the origin of glioma," *Upsala Journal of Medical Sciences*, vol. 117, no. 2, pp. 113–121, May 2012.

[101] H. Zong, R. G. Verhaak, and P. Canoll, "The cellular origin for malignant glioma and prospects for clinical advancements," *Expert Review of Molecular Diagnostics*, vol. 12, no. 4, pp. 383–394, May 2012.

[102] L. Goers, P. Freemont, and K. M. Polizzi, "Co-culture systems and technologies: taking synthetic biology to the next level," *Journal of the Royal Society Interface*, vol. 11, no. 96, Jul. 2014.

[103] D. R. Bogdanowicz and H. H. Lu, "Multifunction Co-culture Model for Evaluating Cell–Cell Interactions," *Methods in Molecular Biology*, vol. 1202, pp. 29–36, 2014.

[104] S. Sawant *et al.*, "Establishment of 3D Co-Culture Models from Different Stages of Human Tongue Tumorigenesis: Utility in Understanding Neoplastic Progression," *PLoS One*, vol. 11, no. 8, Aug. 2016.

[105] R. D. Hurst and I. B. Fritz, "Properties of an immortalised vascular endothelial/glioma cell co-culture model of the blood-brain barrier," *Journal of Cellular Physiology*, vol. 167, no. 1, pp. 81–88, 1996.

[106] A. D. Lehmann, N. Daum, M. Bur, C.-M. Lehr, P. Gehr, and B. M. Rothen-Rutishauser, "An in vitro triple cell co-culture model with primary cells mimicking the human alveolar epithelial barrier," *European Journal of Pharmaceutics and Biopharmaceutics*, vol. 77, no. 3, pp. 398–406, Apr. 2011.

[107] G. Lazzari, V. Nicolas, M. Matsusaki, M. Akashi, P. Couvreur, and S. Mura, "Multicellular spheroid based on a triple co-culture: A novel 3D model to mimic pancreatic tumor complexity," *Acta Biomaterialia*, vol. 78, pp. 296–307, Sep. 2018.